Organometallic Complexes in Biological Applications: Synthesis, Mechanism, and *In Vitro* Behavior

by
Huong Thi Hoai Nguyen

A dissertation submitted to the Department of Chemistry,
College of Natural Sciences and Mathematics
in partial fulfillment of the requirements for the degree of

Doctor of Philosophy

in Chemistry

Chair of Committee: Dr. Loi H. Do

Committee Member: Dr. T. Randall Lee

Committee Member: Dr. Jeremy A. May

Committee Member: Dr. Melissa L. Zastrow

Committee Member: Dr. Michihisa Umetani

University of Houston
May 2021

ACKNOWLEDGMENTS

For starters, I would like to express my sincere appreciation and gratitude to my advisor Dr. Loi H. Do for invaluable guidance, encouragement, and supporting throughout my Ph.D. study. Do research in Dr. Do's group has impactfully contributed to my intellectual and personal development. I would like to thank all my committee members, Dr. Lee, Dr. May, Dr. Zastrow, and Dr. Umetani for taking the time to review my dissertation and providing insightful suggestions that can broaden my research perspective.

I would like to thank to Dr. Umetani and his student – Jacky Wu, who are wonderful collaborators for always being so cooperative and informative. My project was absolutely not possible to reach without their assistance. I am grateful to Dr. Thummel and Dr. Teets and for allowing me to use their instruments. I want to acknowledge Department of Chemistry staff for always being helpful and understanding.

My sincere thanks to all my group members, both past, and present, who made it an enjoyable and productive working environment. We have consistently worked as a team to help each other realize our goals as graduate students. Working in the lab and carrying out rational research would not have been possible without their constant consultation. Especially, I would like to mention Dr. Anh Ngo, Dr. Sohini Bose for introducing me to cell culture techniques, and Dr. Thi Tran for his valuable advice during my doctoral research.

I am extremely grateful to my undergraduate mentor, Dr. Thanh Truong, for inspiring and supporting me to pursue an advance degree in chemistry in the US.

Special thanks to my amazing friends Thi, Tung, Dat, Hieu, Hanh, Quan, Ky, Yennie, Thamon, Dawei, Sohini and Eryn for their invaluable friendship.

Finally, I am sincerely grateful to my parents and my two sisters for their unconditional love, help, and support during my doctoral study.

ABSTRACT

Transition metal complexes are attractive as bioactive compounds due to their structural complexity and ability to achieve high potency and selectivity. In recent years, the development of these complexes has gained much popularity due to their synthetically accessibility and tunable reactivity. However, creating complexes that are non-toxic and active inside biological environments is highly challenging.

Herein, we describe the synthesis of new organometallic complexes and their possible application as anti-cancer agents. In the first project, a bifunctional complex featuring a quinone and picolinamide iridium moieties was synthesized as new transfer hydrogenation catalysts. We proposed that this catalyst design would enable more efficient generation of hydrogen peroxide by taking advantages of intramolecular reactivity. In the presence of sodium formate, our catalytic produced more hydrogen peroxide compared to that by the corresponding tandem catalysts under physiological conditions. We characterized several key reaction intermediates by VT NMR spectroscopy and determined catalyst stability over time. The biocompatibility of the complex toward cancer cell lines was also evaluated.

The second project was performed in collaboration with Dr. Michihisa Umetani, in which we attempted to develop synthetic liver X receptor agonists (GW3965) that are nucleus impermeable and can selectively inhibit nuclear gene expression. Toward this goal, we covalently attached GW3965 to ruthenium/rhodium/iridium complexes using a variety of linkers. The fluorescent cyclometalated iridium complex bearing two GW3965 units showed extra-nuclear localization via live cell imaging. The distribution of Ru/Rh compounds is currently being investigated by Inductive coupled plasma-mass spectroscopy (ICP-MS). Further studies using qPCR, cell proliferation, and cytotoxicity assays would be conducted evaluate these complexes' behavior inside cells.

Our work had led to the first demonstration of using intramolecular transfer hydrogenation to enhance H_2O_2 generation at low catalyst concentrations. We also introduced a new approach for reducing the nuclear permeability of Liver X Receptor agonists. We believe the insights gained from the studies could be used to develop more biocompatible systems in the future.

Table of Contents

LIST OF ABBREVIATIONS

A	Absorbance
CuAAC	Copper azide-alkyne coupling
d	Doublet
DCM	Dichloromethane
DIC	Differential interference contrast
DMEM	Dulbecco's modified eagle medium
DMF	Dimethyl formamide
DMSO	Dimethylsulfoxide
FBS	Fetal bovine serum
GC-FID	Gas chromatography-flame ionization detector
GC-MS	Gas chromatography-mass spectroscopy
HRMS	High resolution mass spectroscopy
IC50	Half maximal inhibitory concentration
ICP-MS	Inductive coupled plasma-mass spectroscopy
IR	Infrared (spectroscopy)
J	Coupling constant
LXR	Liver X Receptor
m	Multiplate or milli
min	Minute
Mp	Melting point
MTS	3-(4,5-dimethylthiazol-2-yl)-5-(3-carboxymethoxyphenyl)-2-(4-sulfophenyl)-2H-tetrazolium
m/z	Mass to charge ratio
NADH	Reduced cofactor nicotinamide adenine dinucleotide

NAD(P)H	Phosphorylated analogue of NADH
NMR	Nuclear magnetic resonance (spectroscopy)
PCC	Pearson’s correlation coefficient
PEG	Polyethylene glycol
Ph	Phenyl
Py	Pyridine
q	quartet
RT	Room temperature
s	Singlet
SAR	Structure-activity relationship
t	Triplet
td	Triplet of doublet
TLC	Thin layer chromatography
THF	Tetrahydrofuran
TON	Turn over number
UV-Vis	Ultraviolet-visible (spectroscopy)
λ_{ex}	Excitation wavelength
λ_{em}	Emission wavelength
μ	Micro

LIST OF FIGURES

LIST OF SCHEMES

LIST OF TABLES

Chapter 1. Intracellular Organometallic Chemistry

Portions of this work have been previously published.

Reprinted with permission Dat P. Nguyen, Huong T. H. Nguyen, Loi H. Do., *ACS Catal.*, **2021**, *11*, 5148-5165. DOI: 10.1021/acscatal.1c00438

1.1 Introduction to Intracellular Reactions

Biological reactions play crucial roles in maintaining normal cell functions and growth. These reactions are typically facilitated by biological catalysts such as enzymes.[1] Inspired by nature, scientists have been trying to mimic these natural systems in order to create artificial replacements for defective or deficient enzymes.[2] Excitingly, synthetic compounds have been showed to induce non-native transformations inside cells, which may have useful applications in medicinal chemistry and chemical biology.[3-4] In 2003, the concept of bioorthogonal chemistry was first time introduced by Bertozzi and co-workers, which describes the chemical reactions that can occur inside of living systems without interfering with native biochemical processes[5-6] There is significant interest in developing biorthogonal reactions for novel applications such as *in situ* drug synthesis, organelles labelling and tracking for the study of biomolecules within living organisms.[7-9] For example, Astex Pharmaceuticals showed that they could control the degradation of proteins by in-cell assembly of proteolysis targeting chimeras. A Click reaction, which is chemoselective, stable, fast, and high yielding,[10] was used to assemble proteolysis targeting chimeras, which degraded two key oncology targets (BRD4 and ERK1/2).[11] While many bioorthogonal reactions form unnatural linkages between substrates, some can form natural linkages such as amides, esters, phosphodiesters.[12-14] For instant, Staudinger ligation and associated coupling reactions have been used to generate amide linkages, which is important in peptide

synthesis.[15] A publication by Raines and coworkers showed that the ligation of a *C*-terminal phosphinothioester with *N*-terminal α-azide formed the amide product in high isolated yield.[16] This study provided a versatile method for protein synthesis. Additionally, bioorthogonal chemistry has accelerated the development of imaging techniques that utilize radioisotopes or molecular tags.[17-18] Scientists have been able to perform controlled intracellular transformations via direct *in situ* drug synthesis or triggered drug release.[9, 19-20]

1.2 Small-Molecule Intracellular Metal Catalyst

In recent years, tremendous attention has been focus on the development of bioorthogonal reactions that could be catalyzed by artificial enzymes or synthetic metal catalysts.[21-22] Artificial metallo enzymes comprise a protein with inorganic active sites while synthetic metal catalysts do not contain any biological components.[23-26] Transition metal complexes are capable of catalyzing a variety of reactions in living cells, such as C-C bond cross coupling,[27-28] olefin metathesis,[29] alloc/allyl-cleavage,[30-33] amide coupling,[34] azide reduction,[35-36] ring formation,[37-38] azide-alkyne cycloaddition,[39-43] and transfer hydrogenation.[44-46] These catalysts can be homogeneous[21] or heterogeneous[33, 47] and the reactions could take place inside[48] or outside of the cells.[19, 42]

One of the first metal-catalyzed reactions performed with cells was reported in 1985. In this work, a water-soluble ruthenium complex was used to hydrogenate the C=C bond of lipids in cellular membranes.[49] Unfortunately, the highly cytotoxic catalyst caused severe protoplast damage. A breakthrough in this field of bioorthogonal catalysis was the discovery of copper-catalyzed azide-alkyne cycloaddition (CuAAC) in 2002 by Folkin and Sharpless.[50] Although the reaction between azides and alkynes can occur in the absence of a catalyst, it usually requires hash conditions and provides poor regioselectivity. In contrast, copper (I) complexes can accelerate this reaction in aqueous mixtures at room temperature to give

selectivity the 1,4-disubstituted triazole (Scheme 1.1a). Over the past few decades, CuAAC has become the most extensively studied reaction in the biological chemistry with applications ranging from the labelling of proteins, nucleic acids, and polysaccharides[51] to the modification of outer/inner surface of virus particles,[52-53] bacteria,[39] and living mammalian cells.[49] Significant effort has been invested in developing copper (I) catalysts that are compatible physiological conditions.[54] To overcome the toxicity of copper salts, researchers found that supporting copper with multidentate improved their biocompatibility. CuAAC reactions has been used in live cells and zebrafish in 2010.[55-56]

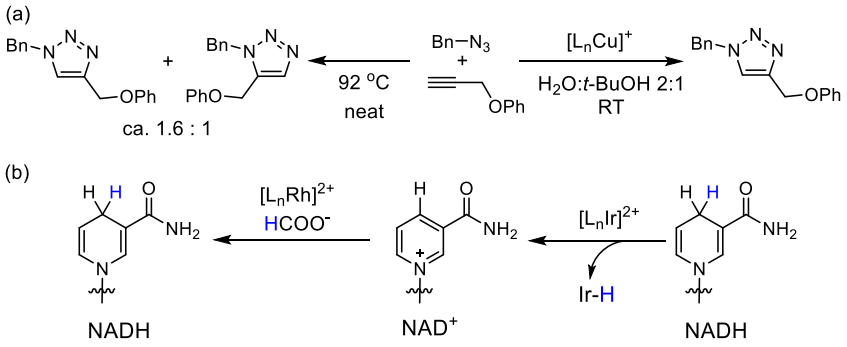

Figure 1.1 CuAAC and transfer hydrogenation reactions in aqueous solution.

Transfer hydrogenation is another attractive target for small-molecule intramolecular metal catalysis.[8] This reaction, which was first introduced over 100 years ago, involves transferring hydride from a donor to an acceptor. Endogenous nicotinamide adenine dinucleotide is a popular substrate for studying transfer hydrogenation because it can exist in either the oxidized (NAD^+) or reduced (NADH) form. [57-58] In 1988, Steckhan reduced NAD^+ to NADH by transferring hydride from formate to NAD^+ using catalyst Rh(Cp*)(2,2'-bipyridine)$(H_2O)^{2+}$ (Cp* = pentamethylcyclopentadienyl anion).[59] Sadler[60] and Fukuzumi[61] utilized NADH as a donor to generate iridium-hydride species in 2012, which was then used to reduce organic electrophiles or generate hydrogen gas (Scheme 1.1b). Enzymes that catalyze transfer hydrogenation play critical roles in metabolism which suggested that synthetic mimics of such enzymes could have important biological applications.[49, 57] Several

studies for *in vitro* transfer hydrogenation have been reported. In 2018, Sadler used chiral osmium (II) complex to asymmetrically reduce pyruvate into *D*-lactate in the interior of A2780 cells (Scheme 1.2a).[45] Our group demonstrated that the reduction of a fluorogenic BODIPY-CHO probe using Ir(Cp*)-picolinamide catalyst could be visualized in NIH-3T3 mouse embryo fibroblast cells using confocal fluorescence microscopy. (Scheme 1.2b).[44]

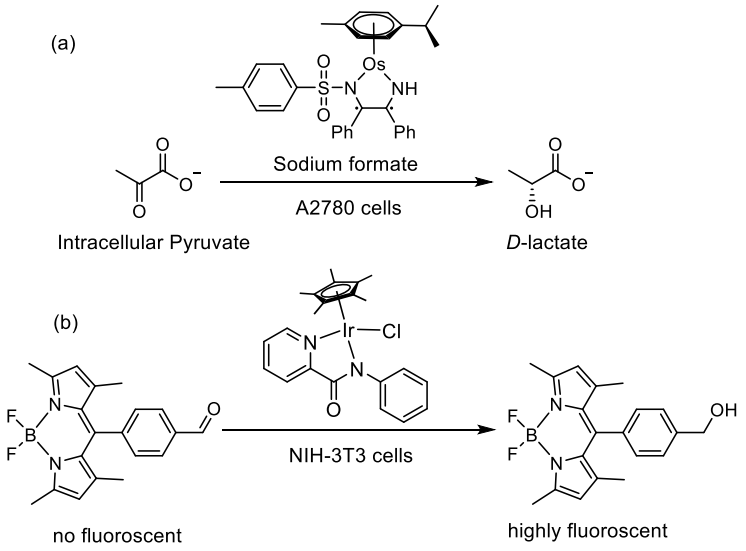

Scheme 1.1 Intracellular transfer hydrogenation studies.

1.3 Therapeutic Applications of Intracellular Metal Complexes

Scientists have explored using metal catalysts for intracellular medicinal chemistry applications. A reaction that has been studied extensively is protecting groups cleavage.[1] This reaction only involves a single substrate and has been performed with a variety of catalyst such as ruthenium, palladium and iron-based complexes. Meggers and coworkers demonstrated that a pyrene-ruthenium complex can catalyze the uncaging of an allylcarbamate-protected substrate to release rhodamine 110 in the presence of thiophenol.[30, 62] In 2011, using the same strategy, Bradley studied depropargylation by Pd^0 nanoparticles inside HeLa cells.[27, 63] Porphyrin-based iron catalysts were also shown to accelerate the reduction of aromatic azides to the corresponding amino group. [35] Researchers have taken

advantages of this deprotection chemistry to develop probes for detection Pd inside living systems.[64-66] The earliest report was from Ahn and coworkers who demonstrated the of an *O*-propargylated fluorescein for Pd-visualization in zebrafish.[67] A series of organic probes were later introduced by Du, Liu, and Fun with excellent selectivity toward Pd over other metal ions.[68-70] An innovation in the design of these probes was the transformation from off-on probes into ratiometric and colorimetric probes with the detection range extended to the near-infrared region.[71-72] A summary of Pd-detecting probes is showed in table 1.1.

Table 1.1 Pd-detecting probes and the fluorescent products.

Author (Year)	Probe Structure	Product
Ahn (2010)	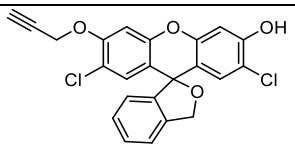	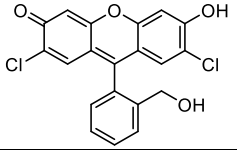
Du and Zhang (2011)	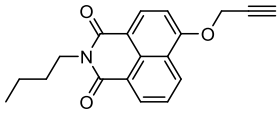	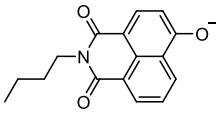
Liu (2014)	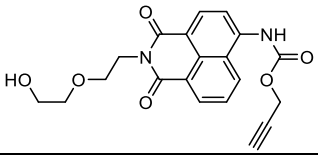	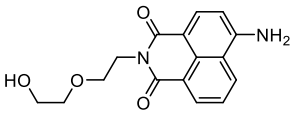
Fun (2013)	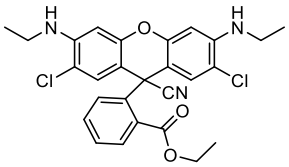	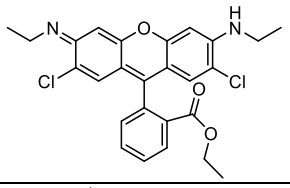
Lin (2013)	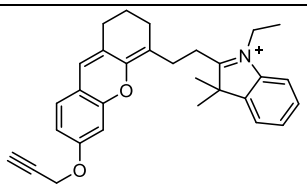 E_x/E_m: 645 nm / 675 nm (weak)	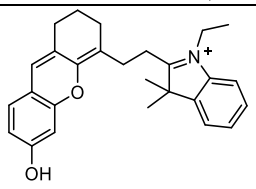 E_x/E_m: 690 nm / 716 nm (strong)
Guo and Zhu (2014)	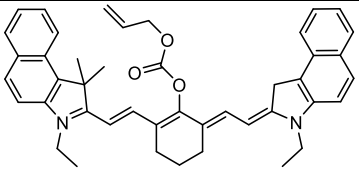 E_x/E_m: 740 nm / 825 nm	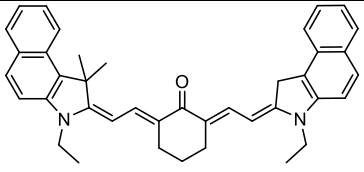 E_x/E_m: 540 nm / 660 nm

These uncaging reactions have also been used for therapeutic applications. For instance, [Ru(Cp*)(cod)Cl] and thiophenol were used by Vázquez and Mascareñas for the allylcarbamate deprotection of intracellular DNA-binding bisbenzamidine, DAPI, and ethidium units in live chicken embryo fibroblast (CEF)[73]. Drug release could be carried out using the same strategy, such deprotection of the anti-cancer drug doxorubicin in HeLa cells reported by Meggers.[74] These advances in drug uncaging have provided new strategies for designing prodrugs.[75-79]

Intracellular bond forming reactions using metal catalysts have also been reported in recent years.[1] These reactions require two substrates along with the catalyst, so they are highly sensitive to concentration. Ring-closing reactions were used to form several fluorogenic reagents in order to detect intracellular Au^{3+} ion.[80-83] Azide-alkyne cycloaddition is one of the most efficient reactions for intracellular coupling of two compounds.[51, 84] Its applications include protein functionalization,[85] and labelling of biological compounds.[86-89]

Other metallic complexes are also useful in catalyzing intermolecular bond forming reactions.[90] In 2011, Lin and coworkers reported an application of the copper-free Sonogashira coupling in *E. coli*.[28] A Pd(II) complex was used to catalyze the reaction between a homopropargyl-glycine (Hpg)-encoded ubiquitin protein with various aryl iodides to provide the corresponding fluorescent products. Another notable study was published by Chen and coworkers, in which they demonstrated the utilization of CuAAC chemistry in the development of a new protein-based pH indicator for intracellular measurements.[91] They used a copper (I) catalyst to connect a fluorophore, 4-*N*,*N*-dimethylamino-1,8-naphthalimide (4-DMN), to an acid-stress chaperon HdeA. Due to changes in protein HdeA conformation upon pH changes, the fluorescence intensity of the conjugated product changes according to the pH environment. This method was applied in *E. coli* in 2014 and gave accurate compartment-specific pH measurement in the range of pH 7 to pH 2.

The organometallic compounds themselves could also possess therapeutic properties.[92] In Sadler's work, a series of iridium, ruthenium, and osmium complexes was found to have anti-cancer activity, with some candidates exhibiting toxicity greater toward cancer cells than the FDA approved drug cisplatin (Fig. 1.1).[93-96] Our group in 2016 showed that the half-sandwich iridium picolinamide complex could lower the 50% growth inhibition concentration (IC_{50}) of the carboplatin drug by up to ~30-50% toward select cancer cell lines.[97] Although the mechanism remained unclear, some preliminary results suggested that those complexes can kill cancer cells by altering their redox balance.[95]

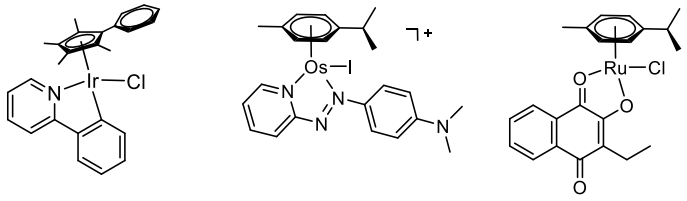

Figure 1.2 Chemical structures of some half-sandwich anticancer complexes.

1.4 Challenges in Designing Bioorganometallic Complexes

Although metal complexes can have useful biological applications, making them biocompatible can be challenging.[74] For example, they must be highly nontoxic, water-soluble, cell permeable, and active under physiological condition.[1, 6] The catalysts must have high catalytic activity so they can be functionally useful at low catalyst concentration. Additionally, a variety of biological components in cellular environment are acidic, basic, coordinating, or redox active, which means that the synthetic metal complexes must be compatible with a wide range of chemical species.

Although there is no standard procedure to evaluate a catalyst for their *in vivo* application, most studies consist of some basic steps as shown in Scheme 1.3. To begin with, a specific bioorthogonal reaction is chosen and a series of relevant catalysts are considered. When evaluating their properties, some important parameters to consider are their aqueous

solubility, dioxygen and biological additives tolerance, and effective concentration. The most promising complexes are then tested for their biocompatibility with one or more cell lines by measuring their IC_{50} values and cellular uptake. Next, the target reactions are be conducted inside living systems and several analytical methods should be used to determine the reaction efficiency. At this step, extra care is needed to ensure the accuracy of the measurements while controls experiments are usually required to determine whether the reactions take place intracellularly or extracellularly. Furthermore, the catalyst, starting agents, and products should not be toxic, unless the final goal is to kill cells such as in anti-cancer chemotherapy. Finally, structure-activity relationship studies are conducted to gain new insights into future catalyst designs.

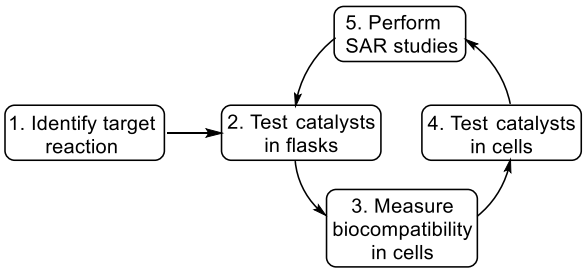

Scheme 1.2 Typical workflow for the design of biocompatible catalysts.

As mentioned above, due to the numerous biological components in living environments, it is challenging to design synthetic complexes that meet all of our design criteria. For example, various factors such as local pH, biological nucleophiles, or solution viscosity could significantly affect the catalyst behavior. Moreover, the low concentration of substrates and catalysts make quantifying them in cells is exceedingly difficult, especially when non-invasive measurements are needed. Some common analytical techniques available for studying intracellular catalysis include fluorescence microscopy, flow cytometry, mass spectrometry, and biological assays. By combining state of the art tools with molecular design, we believe that challenges of creating biocompatible metal catalysts could be overcome.

Chapter 2. Organoiridium-Quinone Conjugates for Facile H_2O_2 Generation

Portions of this work have been previously published.

Reproduced with permission from Nguyen, H. T. H; Do, L. H., *Chem. Commun.*, **2020**, *56*, 13381-13384. DOI: 10.1039/D0CC04970K

2.1 Introduction

In anti-cancer chemotherapy, modulation of reactive oxygen species (ROS) such as peroxide, super peroxide, and hydroxyl radical has been shown to be an effective strategy to kill cancer cells.[98] ROS-inducing agents can increase endogenous ROS, inhibit natural antioxidant enzymes, or deplete glutathione concentrations. Although these agents can operate by distinct mechanisms, achieving high efficiency and selectivity are still major challenges.

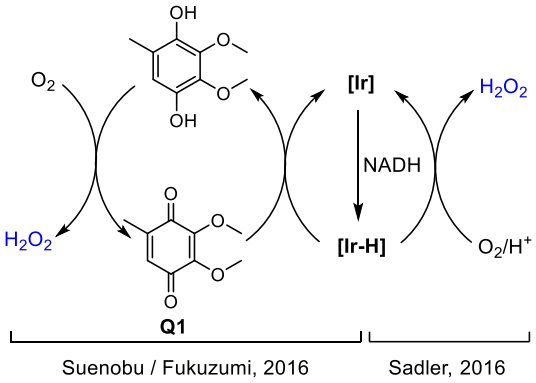

Scheme 2.1 Hydrogen peroxide formation achieved by transfer hydrogenation.

In 2016, Sadler and co-workers introduced a series of half-sandwich organoiridium complexes that could catalyze the formation of hydrogen peroxide from O_2, H^+, and reduced nicotinamide adenine dinucleotide (NADH) via a transfer hydrogenation mechanism.[99] These synthetic compounds could also be used as ROS generating agents under aqueous condition

and were demonstrated to have more potent anti-cancer activity than the well-known drug cisplatin in some cell lines (Scheme 2.1). In related studies, Suenobu, Fukuzumi, and co-worker showed that 2,3-dimethoxy-6-methyl-1,4-benzoquinone (**Q1**) and organoiridium compounds react with NADH and O_2 to produce H_2O_2 in a tandem catalytic process.[61]

The iridium/**Q1** example above is particularly intriguing because the coupling of transfer hydrogenation with autocatalytic O_2 reduction could significantly boost H_2O_2 formation.[61] However, at low catalyst concentrations, a possible concern with this dual component system is the probability for the iridium and **Q1** species to react with each other. Especially in cell studies, the recommended catalytic concentration is typically below 50 μM to minimize possible metal toxicity and the reagents could also be distributed to different cellular locations. To circumvent this potential problem, we propose in this work design of an organoiridium complex that is covalently tethered to a quinone group to promote intramolecular reactivity. The benefits of this bifunctional catalyst design are that both iridium-hydride and hydroquinone units formed during reactions with NADH would be capable of reducing O_2 to H_2O_2 and oxidized quinone could be continuously regenerated regardless of catalyst concentration. This strategy of incorporating redox active moieties into transition metal complexes has been shown to be highly effective for a variety of catalytic applications.[100-101]

2.2 Results and Discussion

2.2.1 Synthesis of Iridium-Quinone Conjugates

To test the feasibility of our bifunctional catalyst concept, we devised a novel molecular construct by attaching the ubiquinone mimic **Q1** to [Cp*Ir(*N*-phenyl pyridinecarboxamidate)Cl] (**Ir1**, Cp* = pentamethylcyclopentadienyl anion). Complex **Ir1** was found in our previous work to be an active transfer hydrogenation catalyst under

biologically relevant conditions and inside cells. Additionally, the substituents around the quinone ring in **Q1** will also help to prevent the formation of Michael adducts. The **Q1** group was tethered to **Ir1** using either an ether or alkyl linker to give complexes **Ir2** and **Ir3a**, respectively (Chart. 2.1).

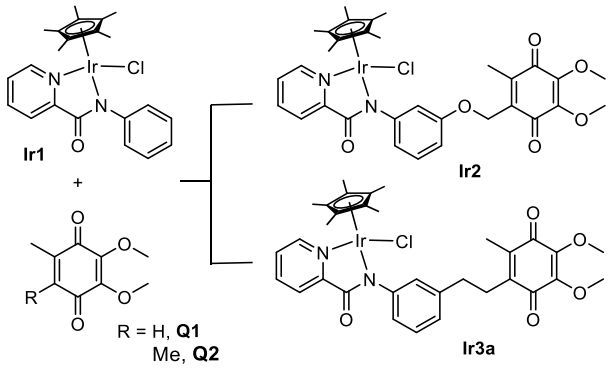

Chart 2.1 Design of organoiridium–quinone conjugates.

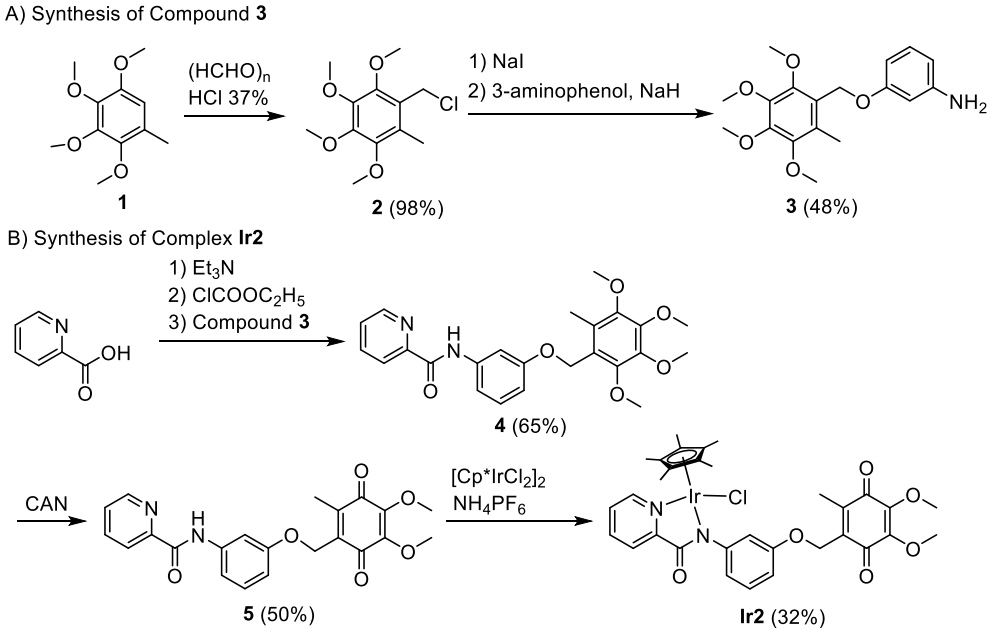

Scheme 2.2 Synthesis of complex **Ir2**.

A 5-step procedure was used to synthesize complex **Ir2** starting from the chloromethylation of tetramethoxytoluene followed by Williamson ether reaction with 3-aminophenol. Compound **3** was amidated with picolinic acid then the product was oxidized by ceric ammonium nitrate (CAN) to obtain ligand **4**. The metalation reaction using

$[Cp^*IrCl_2]_2$ and NH_4PF_6 was performed to obtain **Ir2** catalyst in 20% isolated yield (Scheme 2.2).

To synthesize **Ir3a**, a modified procedure was used. A Wittig was utilized to prepare ligand **8** in moderate yield. Metalation of **8** gave catalyst **Ir3a** in 60% isolated yield (Scheme 2.3).

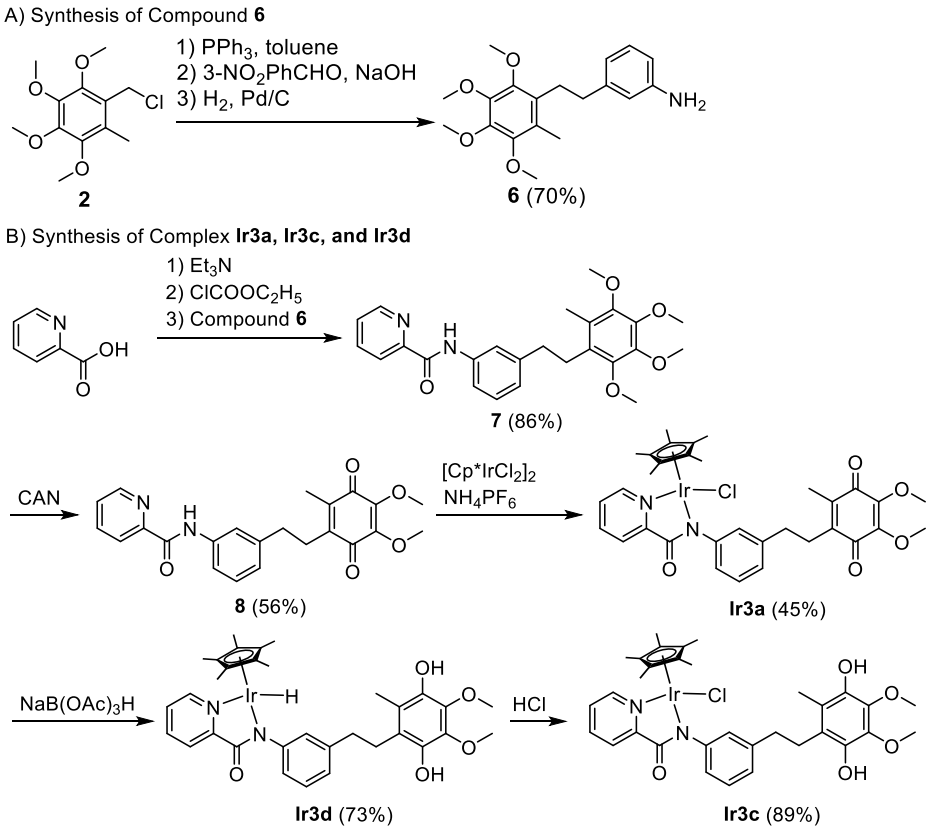

Scheme 2.3 Synthesis of complexes **Ir3a**, **Ir3c**, and **Ir3d**.

The final iridium complexes were obtained in analytically pure form and characterized by various spectroscopic and mass spectrometric methods. Single crystals of **Ir3a** were grown from acetone/pentane and analyzed by X-ray diffraction. The molecular structure of **Ir3a** showed the expected piano-stool motif, in which the iridium center was coordinated by a Cp* ring, two nitrogen donors from ligand **8**, and a chloride. The reduced products of **Ir3a** were prepared as the hydride form **Ir3d** and the chloride form **Ir3c** by

treatment with $NaB(OAc)_3H$ and HCl, respectively. These complexes were used as standards for NMR spectroscopic studies.

2.2.2 Evaluation of H_2O_2 Generation

To examine whether our iridium-quinone conjugates are competent transfer hydrogenation catalysts, we first evaluated their reactions with sodium formate. Because the hydride source NADH has a complicated structure, it was not used for NMR spectroscopy studies. The simpler sodium formate salt was used instead because it shows only 1 ^{1}H NMR signal and has good solubility in water.

Ir2 reaction with NaHCOO *in air* was first examined in acetone-d_6 by NMR spectroscopy. We used a 5 mM solution of **Ir2** in the presence of 2.0 equiv. of NaHCOO and monitored the reaction for 16 h (Fig. 2.1).

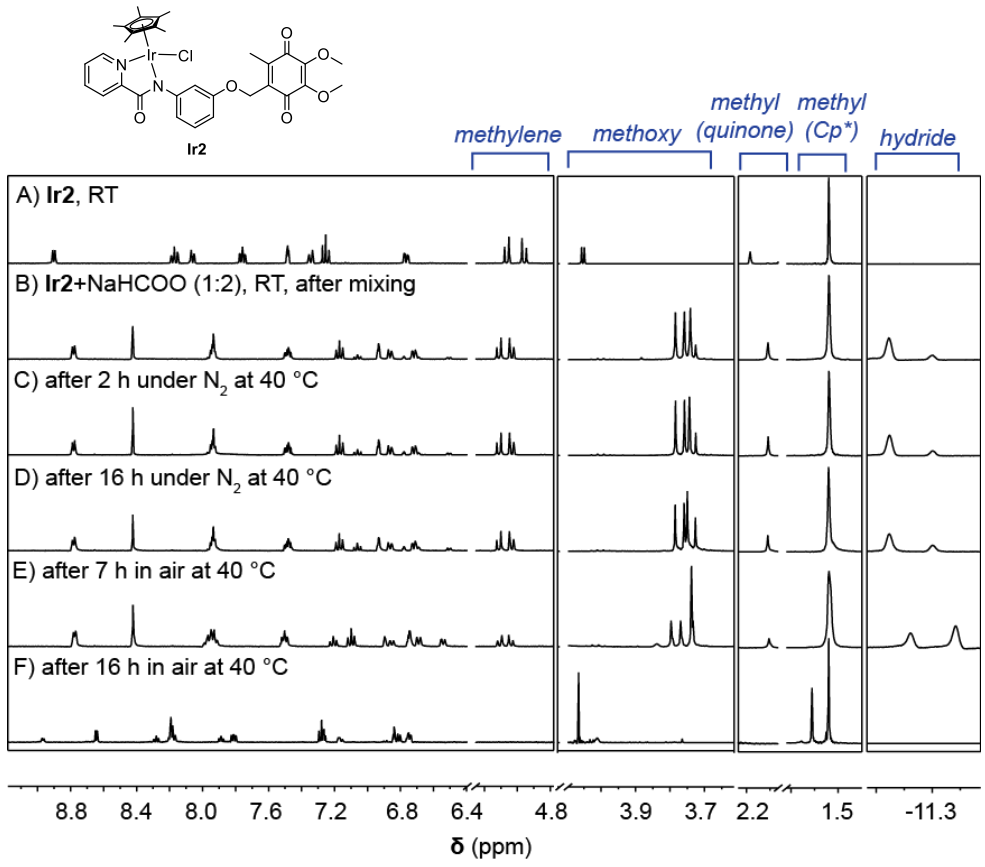

Figure 2.1 The reaction of **Ir2** with 5 equiv. of NaHCOO in acetone-d_6 – D_2O 9:1

We observed change in the NMR spectra immediately after the addition of NaHCOO, which indicated the formation of a new product. This species was stable under an inert atmosphere for up to 16 h at 40 °C. However, as can be seen in spectrum F (Fig. 2.1), the benzylic (methylene) hydrogen peaks disappeared upon exposure to air, suggesting that the ether group had cleaved. This result revealed that **Ir2** had decomposed, most likely due to oxidative cleavage of its benzyl ether bond by the hydrogen peroxide generated. Fortunately, this cleavage was not observed when we tested **Ir3a** under similar reaction conditions. Due to its great chemical stability, **Ir3a** was used for all subsequent studies.

Next, the hydrogen peroxide formation efficiency was compared between the tethered vs. untethered iridium-quinone catalysts. Although a variety of H_2O_2 quantification methods have been reported, some used reagents that are not readily available,[102-104] incompatible with hydroquinone,[105-106] or have insufficient detection range.[107] We found that commercial H_2O_2 test strips provided fast response time and adequate sensitivity for our studies. Using this semi-quantitative detection method combined with ImageJ software analysis, we measured the hydrogen peroxide concentration from reactions of either **Ir3a** or **Ir1**/**Q1** (1:1) with 20 equiv. of NaHCOO in H_2O/DMSO (99:1) under air at several concentrations (Fig. 2.2). The data shown are representative plots. Because of the limitation of the image-based H_2O_2 quantification method, the absolute H_2O_2 concentrations can vary between repeat experiments, but the relative trends are consistent.

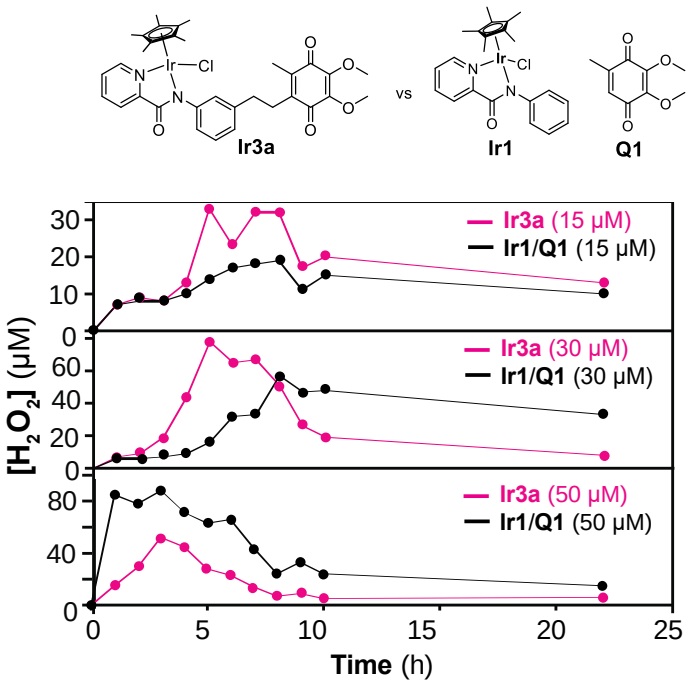

Figure 2.2 Formation of H_2O_2 from reaction of either **Ir3a** or **Ir1**/**Q1** in H_2O/DMSO (99:1) with 20 equiv. of NaHCOO.

At low catalyst concentrations (Fig. 2.2, top/middle), **Ir3a** gave more hydrogen peroxide and at a faster rate than **Ir1**/**Q1.** For example, after 5 h, **Ir3a** produced 2.4-fold (33 vs. 14 μM) and 4.9-fold (78 vs. 16 μM) more H_2O_2 than **Ir1**/**Q1** at catalyst concentrations of 15 and 30 μM, respectively. Interestingly, when the amount of catalyst was increased to 50 μM, the opposite trend was observed (Fig. 2.2, bottom). After 1 h, **Ir1**/**Q1** gave a 5.7-fold increase in H_2O_2 compared to that by **Ir3a** (85 vs. 15 μM, respectively). Additionally, a control experiment showed that **Ir1** generated less H_2O_2 in the reaction with NaHCOO than that using either **Ir3a** or **Ir1**/**Q1** (Fig. 2.15), indicating that the presence of quinone had a beneficial effect. The combination of **Q1** with NaHCOO in the absence of iridium also gave no H_2O_2. These results demonstrated that the tethered **Ir3a** catalyst is more efficient in H_2O_2 generation than the iridium and quinone tandem catalysts at low concentrations (<30 mM), which showed the benefit of having a tethered multi-functional complex. The H_2O_2 results

when using **Ir3a** vs **Ir1**/**Q1** were similar to that when using **Ir3a** vs. **Ir1**/**Q2** at 30 μM catalyst concentration, suggesting that slight differences in the quinone redox potential do not account for the faster rate observed in the former. (Fig. 2.16).

The plots in Fig. 2.2 revealed that H_2O_2 growth was accompanied by subsequent decay, which suggests that the hydrogen peroxide produced may be reacting with one of the reaction components. We observed that when excess H_2O_2 was mixed with 30 μM of **Ir1** or **Ir3a**, the hydrogen peroxide concentration gradually decreased over time (Fig. 2.3, column II, III). In contrast, control solutions containing H_2O_2 only or **Q1**/H_2O_2 showed no significant change in hydrogen peroxide levels over 22 h (Fig. 2.3, column I, IV). We hypothesized that the iridium catalyst was the species responsible for decomposing H_2O_2.

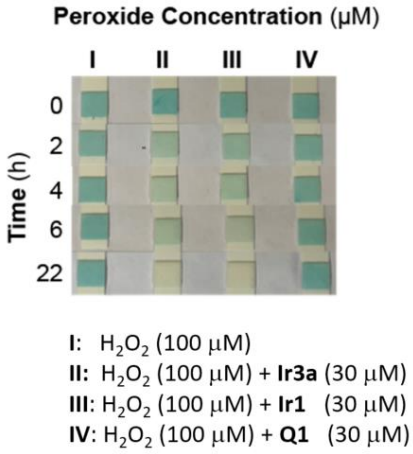

Figure 2.3 Time study of the decomposition of H_2O_2

We also examined the catalyst stability in the present of hydrogen peroxide (Fig. 2.4). The NMR spectra of iridium complexes treated with 5.0 equiv. H_2O_2 showed decreased signal intensity compared to that obtained of fresh catalyst. Upon treatment with 50 equiv. H_2O_2, spectrum of catalyst **Ir3a** contained many additional peaks that were assigned to at least one or more decomposition products (marked with red asterisks *). suggesting that **Ir1** and **Ir3a** were susceptible to oxidative damage in

the presence of excess hydrogen peroxide over an extended period. Attempts to determine the identity of the decomposed Ir species were unsuccessful.

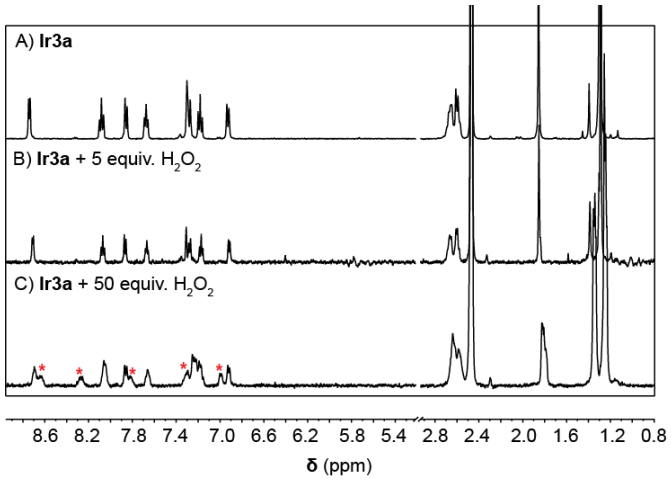

Figure 2.4 ^{1}H NMR spectra (DMSO-d_6, 400 MHz) of complex **Ir3a** before and after H_2O_2 treatment.

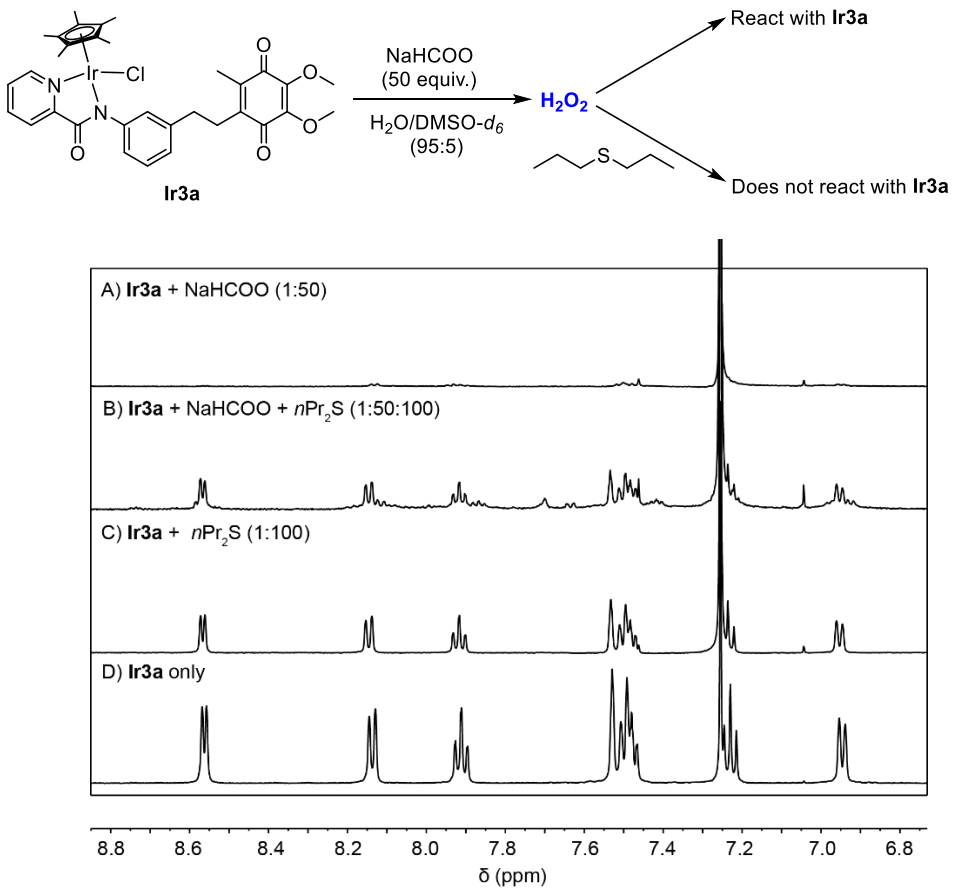

Figure 2.5 ^{1}H NMR spectra ($CDCl_3$, 500 MHz) of **Ir3a** + NaHCOO (+ nPr$_2$S)

To confirm that H_2O_2 is responsible for catalyst decay, we monitored the reaction of **Ir3a** (2 μmol) with NaHCOO (100 μmol) in the absence and presence of propyl sulfide (200 μmol) as an antioxidant (Fig. 2.5).[108] After 18 h, our NMR spectra showed that the sample containing *n*Pr$_2$S still contained significant amounts of **Ir3a** whereas the sample without *n*Pr$_2$S had nearly no detectable amounts of **Ir3a** present. We verified that *n*Pr$_2$S did not inhibit the Ir catalyst activity, so its role was primarily an H_2O_2 scavenger. We can conclude that organoiridium-quinone conjugates are more efficient H_2O_2-generating catalysts than iridium and quinone tandem catalysts at low concentrations (<50 μM). However, after a long reaction time, hydrogen peroxide and iridium catalysts could react with each other, leading to their mutual degradation.

2.2.3 Redox Behavior of the Ir-Quinone Conjugate

Next, we wanted to examine the redox behavior of the Ir-quinone complexes by cyclic voltammetry. The sample solutions contained iridium complexes (1.0 mM) and quinone (0.5 mM) in 0.1 M phosphate buffer saline (PBS). The measurement was recorded at 0.1 V/s using a glassy carbon working electrode, Ag/AgCl reference electrode, and Pt wire as the auxiliary electrode. All potentials are referenced to NHE. (Figure 2.6a).

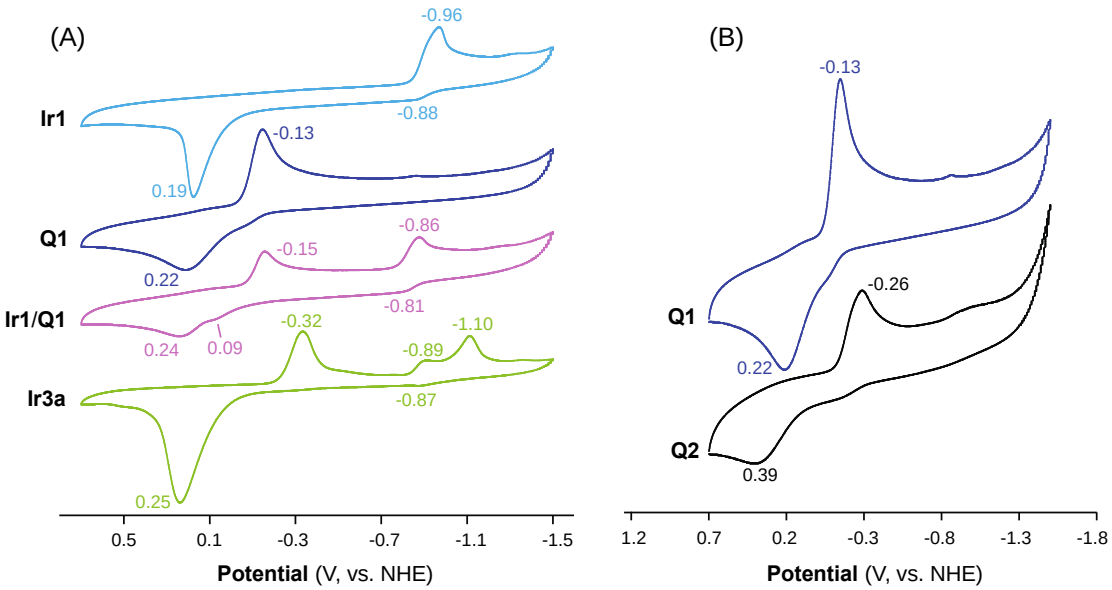

Figure 2.6 Cyclic voltammograms of iridium complexes and quinones in PBS.

Complex **Ir1** displayed an irreversible reduction wave at -0.96 V and oxidation waves at -0.88 (weak) and 0.19 V vs. NHE, similar to those reported in our previous work.[109] Compound **Q1** exhibited a reduction peak at -0.13 V and oxidation peak at 0.22 V. The combined **Ir1** and **Q1** (1:1) sample showed cathodic processes occurring at -0.86 and -0.15 V. Surprisingly, the former peak shifted from that of **Ir1** by about +0.10 V. In order to understand the reason behind this change, we compared the NMR spectra of the mixture of **Ir1**/**Q1** to the spectra of each individual components in $CDCl_3$ (Fig. 2.7).

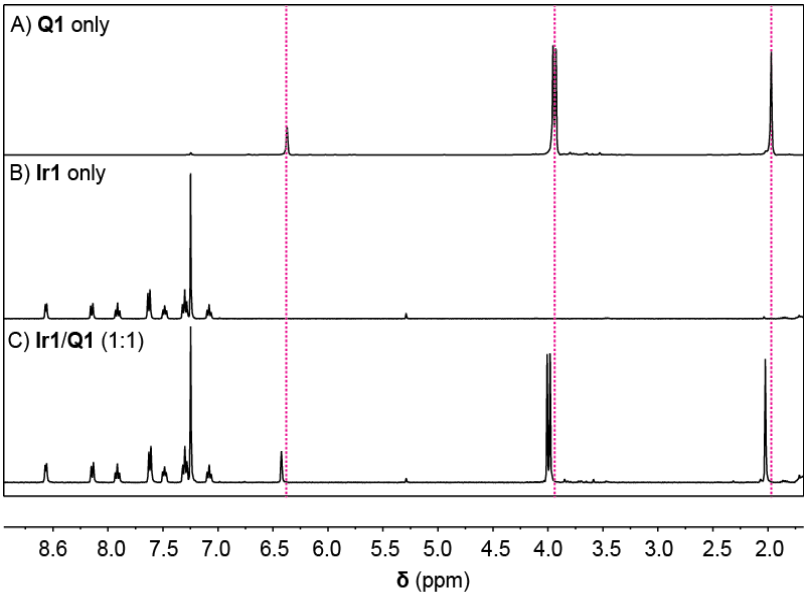

Figure 2.7 Interaction of **Ir1** - **Q1** studied by ^{1}H NMR spectroscopy ($CDCl_3$, 400 MHz).

A small change in the chemical shift was observed in the mixture of **Ir1** and **Q1** compared to that of **Ir1** or **Q1** only, which demonstrated an interaction between those two molecules. The coordination between **Q1** with the iridium center was considered as one possible interaction. We conducted an NMR control experiment where the chloride coordination was replaced by a weaker ligand such as solvent by adding AgOTf to the solution of **Ir1** in CD_3OD/D_2O, 4:1 ratio. The new iridium-solvato species was proposed to bind to quinone easily via a ligand exchange process.[109] However, generation of a new product upon the treatment of **Q1** was not observed (Fig. 2.8). This result suggested that the shift in reduction potential is *not* due to coordination interaction between **Q1** with the iridium complex. We hypothesize that perhaps weak outer sphere interactions (e.g., halogen bonding[110]) between **Ir1** and **Q1** might be responsible for the Ir-centered redox potential change.

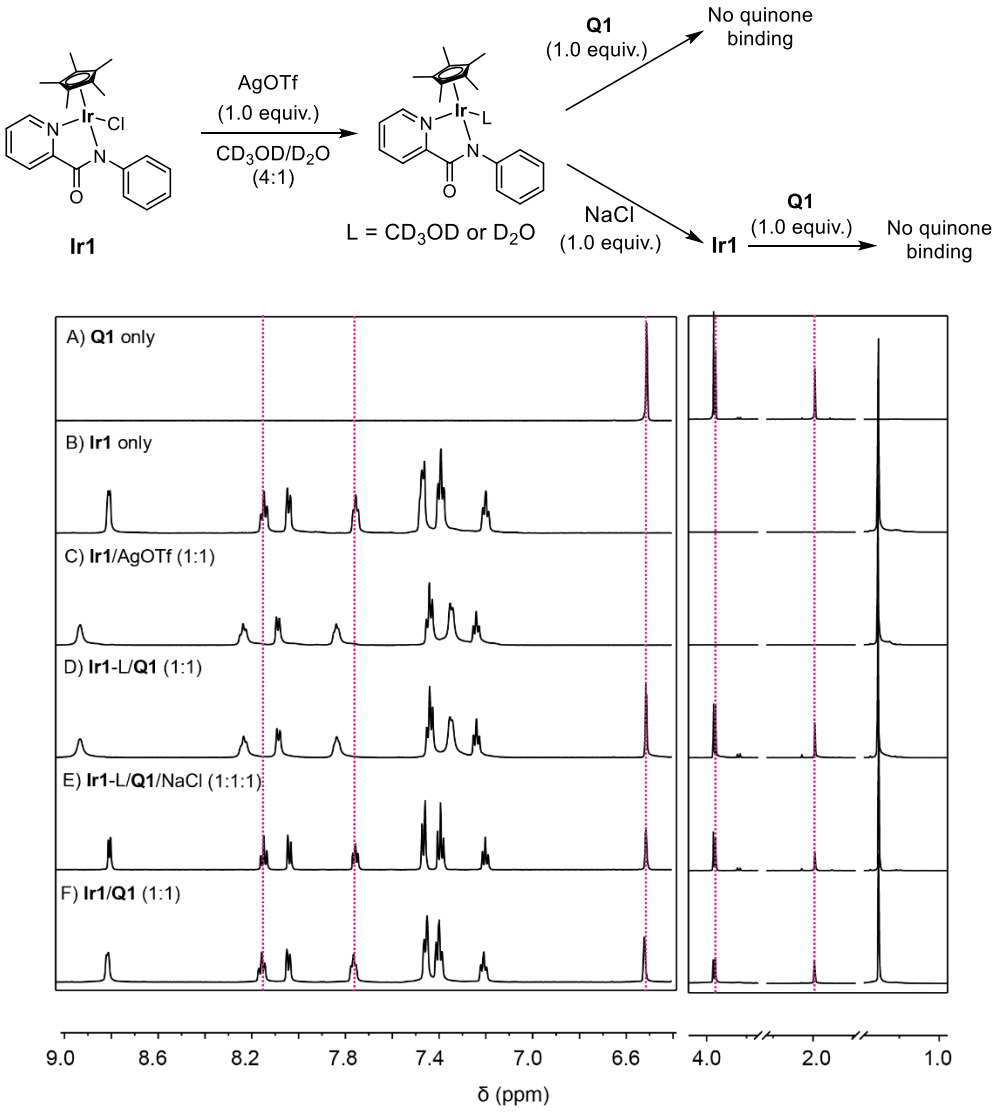

Figure 2.8 Interaction of **Ir1** - **Q1** in the addition of AgOTf studied by ^{1}H NMR spectroscopy (CD_3OD/D_2O, 4:1, 600 MHz)**.**

The CV of **Ir3a** displayed reduction peaks at -1.10, -0.89, and -0.32 V and oxidation peaks at -0.87 (weak) and 0.25 V. The cathodic process at -0.32 V was attributed to reduction of the quinone ring. This potential is similar to that observed in the CV of **Q2** (E_{red}= -0.26 V), which is expected given that **Q2** has a 5-methyl group analogous to the alkyl chain attached to the quinone ring in **Ir3a (**Fig. 2.6b). We presume that the peaks at -1.10 and -0.89 V correspond to iridium-based reductions but are uncertain why there are two peaks in this region since **Ir1** showed only one. One possibility is that **Ir3a** coordinates to each other

intermolecularly to give a mixture of monometallic and multimetallic species. However, further studies are needed to determine the nuclearity of **Ir3a** in solution.

2.2.4 Mechanistic Studies

To understand the reaction of the iridium catalyst and NaHCOO, we performed additional NMR study using **Ir3a**. In experiments conducted at room temperature, reaction of **Ir3a** with excess NaHCOO led to quantitative conversion to the reduced hydroquinone product **Ir3d** within ~5 min followed (Scheme 2.4).

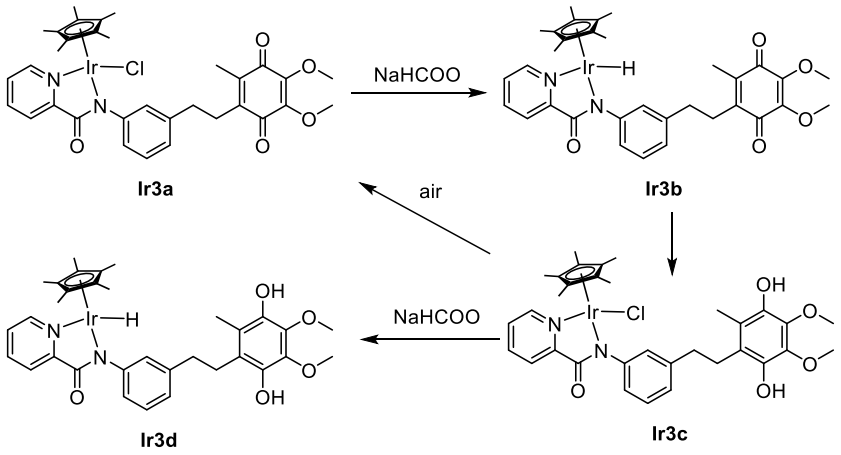

Scheme 2.4 Proposed reaction pathway between **Ir3a** and NaHCOO.

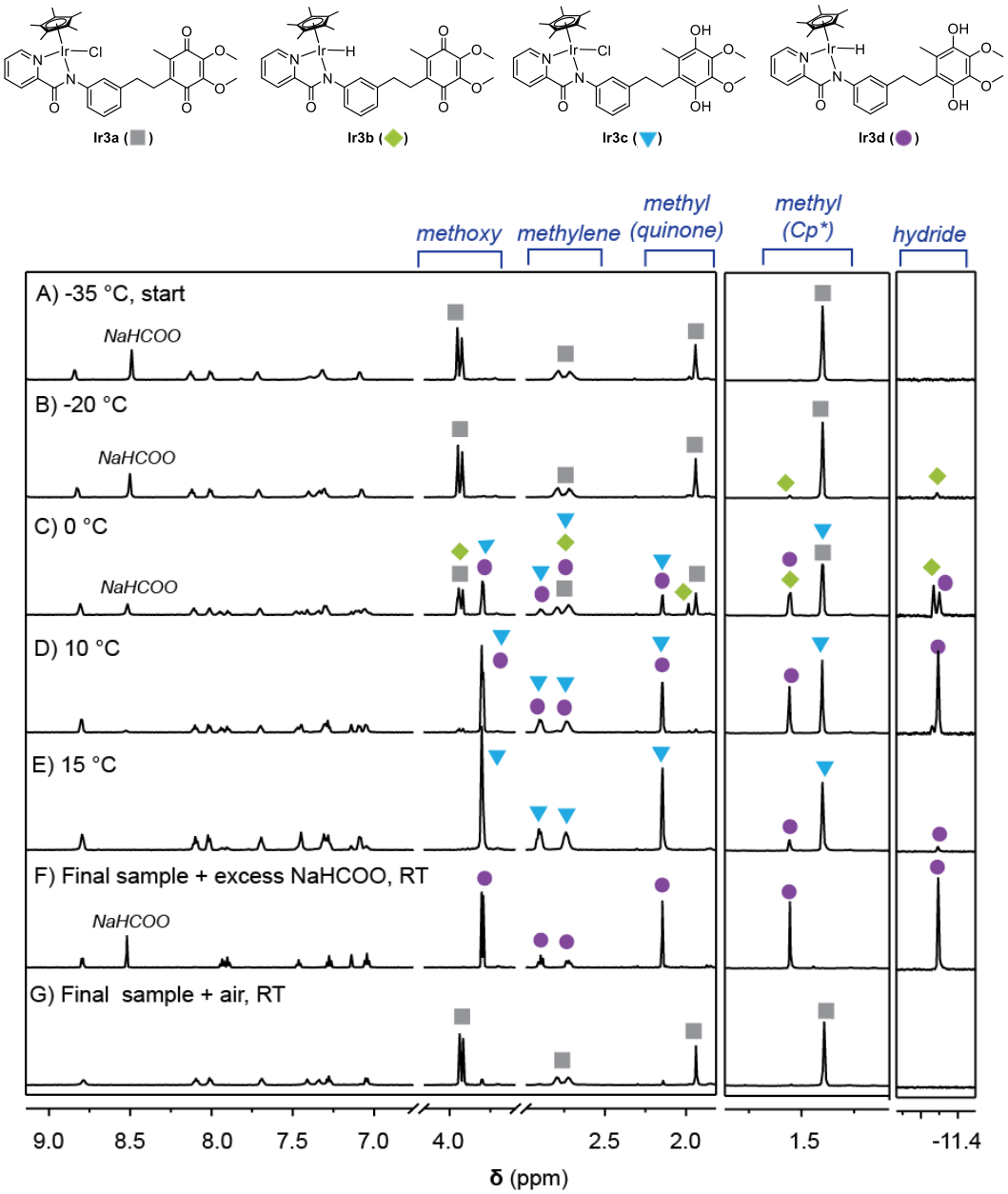

Figure 2.9 Reaction of **Ir3a** with NaHCOO (2.0 equiv.) in CD_3OD studied by variable temperature ^1H NMR spectroscopy (600 MHz).

To follow the reaction *in situ*, variable temperature NMR spectroscopic measurements were performed (Fig. 2.9). When **Ir3a** and NaHCOO (1:2) were combined at -35 °C under nitrogen, only peaks corresponding to the starting iridium complex and NaHCOO were present, suggesting no reaction had taken place. Upon warming to -20 °C, a distinct signal at -11.29 ppm appeared, which is characteristic of an iridium-hydride species.[109, 111] This intermediate is proposed to be the iridium-hydride/quinone complex **Ir3b** formed from

decarboxylation of NaHCOO by the Ir center. When the reaction mixture was increased to 0 °C, the formation of two additional species was apparent. Their identities were determined to be the iridium-chloride/hydroquinone (**Ir3c**) and iridium-hydride/hydroquinone (**Ir3d**) species based on comparison with the NMR spectra obtained from independently prepared samples. Complex **Ir3c** can be formed spontaneously from **Ir3b** as a result of either intermolecular or intramolecular hydride transfer between Ir–H and quinone functionalities.[112-113] Subsequent conversion to **Ir3d** could then proceed by reaction of **Ir3c** with another equivalence of formate. Surprisingly, when the NMR sample was warmed from 10 to 15 °C, the amount of **Ir3d** decreased whereas the amount of **Ir3c** increased (*cf.* spectrum D vs. E in Fig. 2.9). However, to establish that **Ir3d** is the most reduced product, addition of excess NaHCOO to the 15 °C sample gave quantitative amounts of **Ir3d** (spectrum F). Finally, when the 15 °C sample was exposed to air overnight, the starting **Ir3a** complex was regenerated (spectrum G).

Table 2.1 ^{1}H NMR Spectral Peak Assignments from Reaction of **Ir3a** with NaHOO[a]

Complex	Hydride	Methyl (Cp*)	Methyl (quinone)	Methylene	Methoxy
Ir3a	none	1.381	1.924	2.686, 2.766	3.907, 3.934
Ir3b	-11.287	1.534	1.967	2.70, 2.88[b]	3.917, 3.927
Ir3c	none	1.379	2.126	2.70, 2.77[b]	3.77, 3.78[b]
Ir3d	-11.309	1.540	2.131	2.707, 2.880	3.779, 3.789

[a]All chemical shift values are reported in ppm. There were minimal peak shifts due to temperature. These data were obtained from the experiment in Fig. 2.10. The peaks for **Ir3a**, **Ir3c**, and **Ir3d** matched those observed in independently prepared complexes. [b]These peaks overlap with those of one or more additional species.

Table 2.2 Population of Iridium Species at Various Temperatures[a]

Temperature	Ir3a	Ir3b	Ir3c	Ir3d
-35 °C	100%	0	0	0
-20 °C	97%	3%	0	0
0 °C	39%	19%	24%	19%
10 °C	trace	trace	47%	53%
15 °C	0	0	86%	14%

[a]Percentage population determined based on the peak integrations of the various iridium species at the specified temperature. These data were obtained from the reaction of **Ir3a** with NaHCOO shown in Fig. 2.10.

To identify the intermediates, the chemical shifts of the species observed were compared to those of individually prepared standards. (Table 2.1). We then calculated the population of the various iridium species at specific temperatures based on the peak integrations (Table 2.2). We found that ~4 equiv. of NaHCOO is required for complete conversation of **Ir3a** to **Ir3d** (Fig. 2.10). Although the amount of NaHCOO is greater than the quantity needed for stoichiometric conversion from **Ir3a** → **Ir3c** → **Ir3d**, the growth of **Ir3d** with greater amounts of reductant added indicates it is the most reduced species. Since this reaction should only require two rather than four reducing equivalents, these results suggest that perhaps the Ir-H units could decay via reaction with solvent or other proton sources.[114-115]

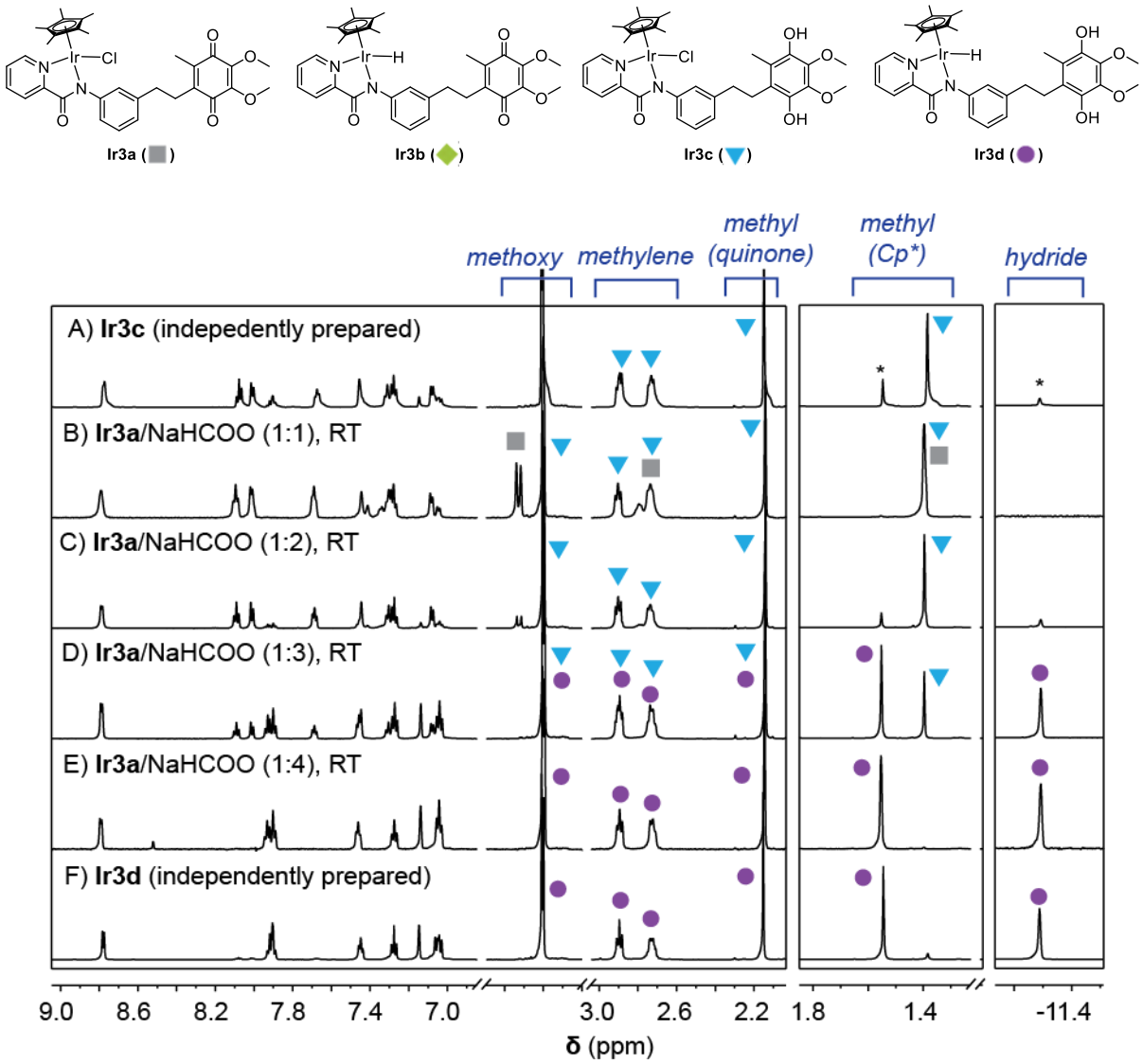

Figure 2.10 Reaction of **Ir3a** with NaHCOO (1-4 equiv.) in CD_3OD at RT (500 MHz).

The catalytic efficiency of **Ir3a** was determined by measuring its turnover number (TON). Because quantifying the total amount of H_2O_2 produced was problematic due to its subsequent reactivity with Ir, changes in NaHCOO concentration was monitored instead. We observed that reaction of NaHCOO (20 µmol) with **Ir3a** (0.5 µmol) was complete after 21 h (Fig. 2.11) and gave a TON = 40, which suggests that our iridium-quinone complex is indeed catalytic.

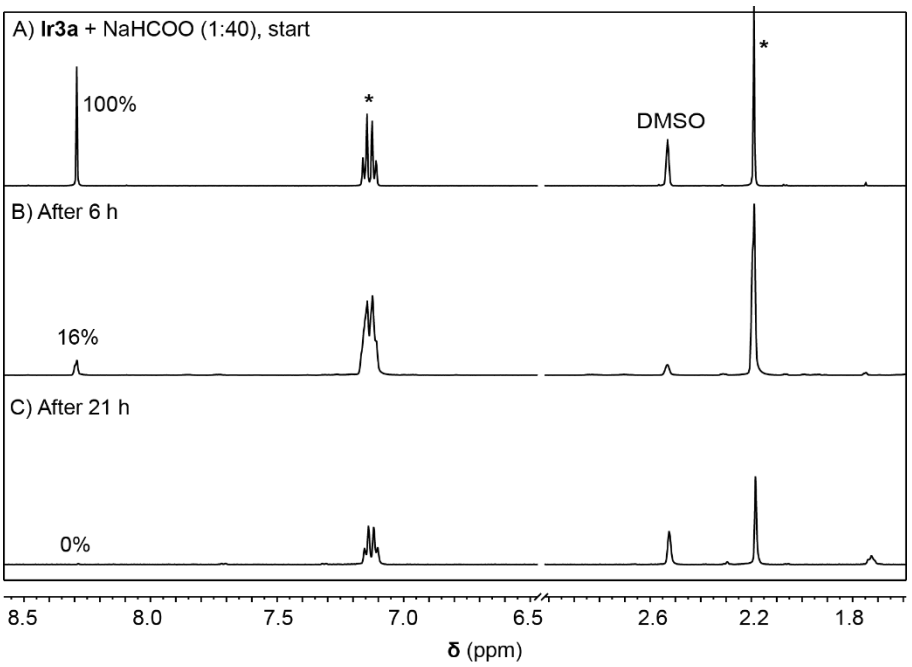

Figure 2.11 Reaction of **Ir3a** (0.5 µmol) with NaHCOO (20 µmol) over a period of 21 h (DMSO-d_6/D_2O, 500 MHz).

We propose that the iridium-quinone and NaHCOO reactions operate by several competing pathways. In our tethered **Ir3a** catalyst, H_2O_2 could form from reaction of O_2 with **Ir3b**, **Ir3c** or **Ir3d** (Scheme 2.5 – Structures drawn in simplified form). Because the iridium and quinone units are covalently linked, the rate of intramolecular hydride transfer to reactivate the quinone unit (i.e., **Ir3b** → **Ir3c**) is independent of catalyst concentration. Intermolecular reactions between the **Ir3a**-**Ir3d** species are also possible but less likely to occur at lower catalyst concentrations. In the untethered **Ir1**/**Q1** system, similar reaction pathways are potentially accessible. However, the key difference is that hydride transfer from **Ir1**-hydride to **Q1** is a bimolecular reaction and thus, this step is concentration dependent (assuming the hydride transfer step is rate-limiting).[112-113] At high catalyst concentrations, we propose that the above transfer hydrogenation process to generate H_2O_2 is less important than the autocatalytic reaction between hydroquinone and O_2. In fact, studies by Suenobu/Fukuzumi and co-workers showed the rate of H_2O_2 formation was

dependent only on the concentrations of **Q1** and O_2 and not iridium or NADH (when [**Q1**] > [Ir]).[61] They established that reaction of hydroquinone and O_2 followed a sigmoidal curve, which is indicative of autocatalysis. Our observation that **Ir3a** is more efficient at low concentration whereas **Ir1**/**Q1** is more efficient at high concentration is consistent with a switch in major vs. minor reaction pathways. More detailed kinetic studies, however, are needed to interrogate this mechanistic hypothesis.

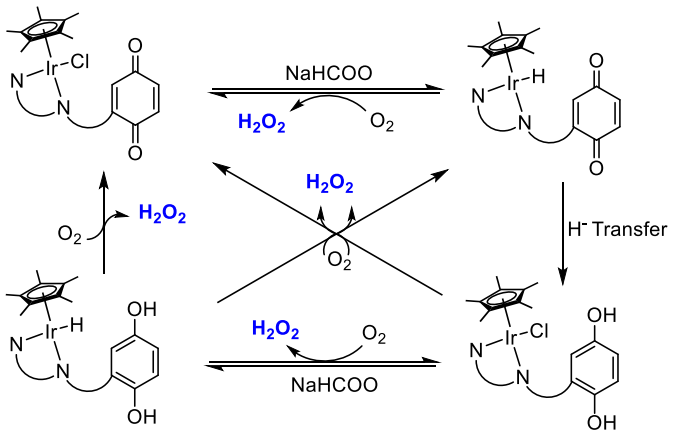

Scheme 2.5 Possible intramolecular pathways to produce H_2O_2 from the reaction of **Ir3a** with NaHCOO.

2.2.5 Evaluation of Biocompatibility

Biological tests were performed to evaluate the ability of **Ir3a** to produce reactive oxygen species in different cell lines. The toxicity of catalyst **Ir3a** was compared to that of **Ir1**, quinone, and a mixture of **Ir1** and quinone. Because MTS assay is NADH-dependent, we used SRB assays instead to measure cell viability. Using A2780 – human lung cancer cells, we determined that **Ir3a** and **Ir1** had similar IC_{50} values (24 h) of 54 and 53 μM, respectively. Additionally, the IC_{50} of **Q1** and **Ir1**/**Q1** were 44 and 25 μM, respectively. These values indicate that cells exposed to both Ir and quinone exhibited greater cell death,

although these results are too preliminary for us to draw any conclusions about the biological mechanism of action.

Next, we tested whether the addition of a hydride source to the iridium catalyst could enhance cell killing, presumably by increasing generation of ROS. After 24 h incubation with catalysts at 0.3× of their IC_{50} values, the A2780 cells were washed, and then treated with HCOONa at 0.5, 1.0 and 2.0 mM respectively for another 24 h. Addition of HCOONa showed no change in cell killing with cell viability at ~100% under all conditions, which was not what we predicted based on work by Sadler and coworkers.[45] We hypothesized that after the washing step, there were not enough accumulated catalysts inside cells that no notable differences were observed between different treatments. Additionally, we propose that the oxidation of hydroquinone into quinone is slower inside living cells than in the reaction flask. Further studies are needed to understand this surprising result.

2.3 Conclusion

In summary, we showed for the first time that organoiridium-quinone conjugates are more efficient H_2O_2-generating catalysts than iridium and quinone tandem catalysts at low concentrations (<50 μM). We expect that inside living cells, the hydrogen peroxide produced by **Ir3a** would likely be scavenged by reactive biomolecules such as glutathione before having the opportunity to degrade the catalyst as observed in the reaction flask. Although we were able to achieve up to ~4.9-fold increase in H_2O_2 formation using **Ir3a**, we anticipate that further optimization of the iridium-quinone construct could lead to even greater rate enhancements. Our results could have important biological relevance because these studies were performed under ambient[99] rather than oxygen-enriched (e.g., 0.5-1.0 atm of O_2)[116] environments. Because some of the most potent quinone-based anti-cancer agents have 50% growth inhibition concentrations below 50 μM,[117-118] they are not typically used in amounts

that would allow them to fully exploit their autocatalytic H_2O_2 forming capabilities. Thus, our strategy of combining half-sandwich iridium complexes[97, 119] with quinones could take advantage of synergistic reactivity to maximize their therapeutic benefits even in low-doses.

2.4 Experimental Section

2.4.1 General Procedures

Commercial reagents were used as received without further purification. All air- and water-sensitive manipulations were performed using standard Schlenk techniques or under a nitrogen atmosphere inside a glovebox. NMR samples of iridium-hydride complexes were prepared inside the glovebox and then transferred to J-Young tubes before taken outside. Anhydrous solvents were obtained from an Innovative Technology solvent drying system saturated with Argon. Complex **Ir1, Q1** and **Q2** were prepared as previously described.

Physical Methods: NMR spectra were acquired using JEOL spectrometers (ECA-400, 500, and 600) at room temperature and referenced using residual solvent peaks. All ^{13}C NMR spectra were proton-decoupled. Gas chromatography-mass spectrometry (GC/GC-MS) was performed using an Agilent 7890 GC/5977A MSD instrument equipped with an HP-5MS capillary column. Cyclic voltammetry (CV) experiments were performed using a BAS Epsilon electroanalytical system. Ultraviolet-visible (UV) absorption spectroscopic studies were performed using an Agilent Cary 60 spectrophotometer. Cyclic voltammograms of the iridium complexes and quinone were recorded at 0.1 V/s in phosphate buffer saline (0.1M, PBS) using a glassy carbon working electrode, an Ag/AgCl reference electrode, and a Pt wire as the auxiliary electrode. All potentials were referenced to NHE.

2.4.2 Synthesis and Characterization

Preparation of Compound 2. To a stirred mixture of 1,2,3,4-tetramethoxytoluene (3.0 g, 14.1 mmol, 1.0 equiv.) and paraformaldehyde (633 mg, 21.1 mmol, 1.5 equiv.) at room temperature, 3 mL of concentrated HCl was added. The mixture was then stirred at 40 °C for 2 h. Water (10 mL) was added and the organic layer was extracted into ethyl acetate (4 x 5 mL). The combined mixture was washed with brine (4 x 5 mL), dried over Na_2SO_4, filtered to removing the drying agent, and then evaporated to obtain a yellow oil **2** (3.6 g, 98%). ^{1}H NMR ($CDCl_3$, 600 MHz): δ (ppm) = 4.58 (s, 2H), 3.83 (s, 3H), 3.81 (s, 3H), 3.80 (s, 3H), 3.769 (s, 3H), 2.19 (s, 3H). ^{13}C NMR ($CDCl_3$, 150.91 MHz): δ (ppm) = 148.49, 148.06, 147.72, 144.77, 126.60, 124.85, 61.59, 60.92, 60.57, 60.56, 38.48, 10.98. IR: ν = 1037, 1071, 1195, 1279, 1352, 1406, 1466, 2830 and 2936 cm^{-1}. GC-MS: calc. for $C_{12}H_{17}ClO_4$ $[M]^+$ = 260.0, found 260.1

Preparation of Compound 3. Compound **2** (1.2 g, 4.0 mmol) and NaI (1.2 g, 8.0 mmol) were combined in 25 mL of acetone. In a separate flask, 3-aminophenol (480 mg, 4.4 mmol) and NaH (60% in mineral oil; 240 mg, 6.0 mmol) were stirred in 25 mL of dry THF. These two solutions were stirred separately at room temperature for 2 h before the former was transferred into the latter via syringe. This mixture was stirred at room temperature for ~14 h and was monitored by thin layer chromatography. After the reaction was complete, the solvent was removed, and the organic products were dissolved into DCM and washed with water. The organic layer was separated, evaporated to dryness, and purified by silica gel column chromatography using ethyl acetate:hexane (1:2) to obtain the final product as a colorless oil (640 mg, 48%). ^{1}H NMR ($CDCl_3$, 400 MHz): δ (ppm) = 7.25 (s, 1H), 7.09 (t, J_{HH} = 8.0 Hz, 1H), 6.46 (dd, J_{HH} = 8.0, 2.4 Hz, 1H), 6.36 (t, J_{HH} = 2.0 Hz, 1H), 6.33 (dd, J_{HH}

= 8.0, 2.0 Hz, 1H), 4.98 (s, 2H), 3.94 (s, 3H), 3.91 (s, 3H), 3.83 (s, 3H), 3.80 (s, 3H), 2.24 (s, 3H). ^{13}C NMR ($CDCl_3$, 150.91 MHz): δ (ppm) = 160.31, 149.15, 148.26, 148.09, 147.60, 144.84, 130.20, 127.76, 123.89, 108.12, 104.74, 101.78, 62.29, 61.99, 61.29, 61.18, 60.79, 11.66 IR: *ν* = 730, 1010, 1046, 1105, 1158, 1185, 1267, 1353, 1408, 1464, 1495, 1599, 2381, 2936, and 3373 cm^{-1}. GC-MS calc. for $C_{18}H_{23}NO_3$ $[M]^+$ = 333.4, found 333.1.

Preparation of Compound 4. In a 100 mL round bottom flask, picolinic acid (431 mg, 3.5 mmol, 1.75 equiv.) was stirred in 20 mL of anhydrous dichloromethane. Trimethylamine (980 μL, 7 mmol, 3.5 equiv.) was added and the reaction mixture was cooled in an ice bath for 10 min. Next, ethyl chloroformate (335 μL, 3.5 mmol, 1.75 equiv.) was added dropwise and the reaction was stirred at 0 °C for another 20 min before warming to RT. After compound **3** (666 mg, 2 mmol, 1.0 equiv.) was added, the reaction was refluxed for 5 h. Finally, the reaction mixture was quenched by the addition of 30 mL of water, extracted into dichloromethane (3×20 mL), dried over sodium sulfate, filtered to remove the salt, and concentrated. The final product was purified by column chromatography (ethyl acetate:hexane 1:1) as a yellow oil (564 mg, 65%). ^{1}H NMR ($CDCl_3$, 500 MHz): δ (ppm) = 10.05 (s, 1H), 8.63 (d, J_{HH} = 4.0 Hz ,1H), 8.30 (d, J_{HH} = 8.0 Hz, 1H), 7.91 (td, J_{HH} = 6.4, 1.6 Hz, 1H), 7.68 (s, 1H), 7.50-7.48 (m, 1H), 7.30 (d, J_{HH} = 4.4 Hz, 2H), 6.83-6.81 (m, 1H), 5.08 (s, 2H), 3.95 (s, 3H), 3.92 (s, 3H), 3.84 (s, 3H), 3.81 (s, 3H), 2.26 (s, 2H). ^{13}C NMR ($CDCl_3$, 125.73 MHz): δ (ppm) = 162.10, 159.81, 149.82, 149.21, 148.22, 148.08, 147.67, 144.82, 139.04, 137.82, 129.89, 127.76, 126.61, 123.61, 122.46, 112.24, 111.33, 106.01, 62.37, 62.27, 61.30, 61.20, 60.83, 11.70. IR: *ν* = 687, 1010, 1046, 1106, 1160, 1185, 1280, 1353, 1408, 1464, 1528, 1597, 1686, 2934, and 3337 cm^{-1}. ESI–MS(+) calc. for $C_{24}H_{26}N_2O_6$ $[M+Na]^+$ = 461.1688, found 461.1690.

Preparation of Compound 5. A solution of compound **4** (1.0 g, 2.3 mmol, 1.0 equiv.) in

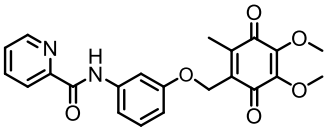

THF (20 mL) was stirred in an ice bath for 5 min. Ceric ammonium nitrate (3.2 g, 5.75 mmol, 2.5 equiv.) in water (20 mL) was added dropwise into the reaction flask over a 10 min period. After the addition was complete, the mixture turned from colorless to orange. The reaction was allowed to warm up to RT and stirred for an additional 1 h while monitoring by TLC. To workup the reaction, THF was gently removed under vacuum and the crude product was extracted into ethyl acetate. The organic layer was washed with water, dried over Na_2SO_4, filtered to remove the salt, and then concentrated. The final product was obtained after purification by silica gel column chromatography (ethyl acetate:hexane, 2:1) as a sticky orange oil (466 mg, 50%).^{1}H NMR ($CDCl_3$, 500 MHz): δ (ppm) = 10.02 (s, 1H), 8.58 (d, J_{HH} = 5.0 Hz , 1H), 8.26 (d, J_{HH} = 10.0 Hz, 1H), 7.88 (t, J_{HH} = 5.0 Hz, 1H), 7.62 (s, 1H), 7.50-7.47 (m, 1H), 7.25 (s, 2H), 6.71 (d, J_{HH} = 10.0 Hz, 1H), 4.95 (s, 2H), 4.01 (s, 3H), 3.98 (s, 3H), 2.14 (s, 2H). ^{13}C NMR ($CDCl_3$, 125.7 MHz): δ (ppm) = 184.39, 183.01, 162.13, 159.02, 149.67, 148.08, 144.84, 144.56, 144.24, 139.07, 137.85, 135.79, 129.98, 126.67, 122.48, 112.75, 110.98, 106.21, 61.40, 61.33, 60.41, 12.52. IR: ν = 687, 729, 1041, 1158, 1186, 1268, 1445, 1528, 1607, 1651, 1683, 2948, and 3329 cm^{-1}. ESI–MS(+) calc. for $C_{22}H_{20}N_2O_6$ $[M+Na]^+$ = 431.1219, found 431.1213.

Preparation of Complex Ir2. In a round bottom flask $[Cp^*IrCl_2]_2$ and (40 mg, 0.05 mmol,

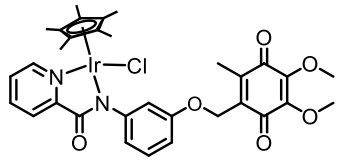

1.0 equiv.) and ligand **5** (42.4 mg, 0.105 mmol, 2.1 equiv.) were added into 8 mL of degassed ethanol and stirred for 15 min at 80 °C. The reaction mixture was treated with ammonium hexafluorophosphate (33 mg, 0.225 mmol, 4.5 equiv.) and stirred overnight at 80 °C. The ethanol solvent was removed by rotary evaporation to obtain a dark yellow solid. This crude

material was dissolved in a minimal amount of DCM and then mixed with hexanes until a solid precipitate formed, which was isolated by filtration (25 mg, 32%). ^{1}H NMR ($CDCl_3$, 500 MHz): δ (ppm) = 8.56 (d, J_{HH} = 5.0 Hz, 1H), 8.15 (d, J_{HH} = 5.0 Hz, 1H), 7.92 (t, J_{HH} = 10.0 Hz, 1H), 7.49 (t, J_{HH} = 8.0 Hz, 1H), 7.40 (s, 1H), 7.28-7.22 (m, 1H), 7.21 (t, J_{HH} = 8.0 Hz, 1H), 6.67 (d, J_{HH} = 10.0 Hz, 1H), 4.95-4.84 (m, 2H), 4.02 (s, 3H), 3.99 (s, 3H), 2.12 (s, 3H), 1.42 (s, 15H). ^{13}C NMR ($CDCl_3$, 125.7 MHz): δ (ppm) = 184.54, 183.10, 168.45, 158.63, 155.80, 149.73, 149.48, 144.75, 144.71, 144.22, 138.67, 136.06, 128.72, 127.46, 126.57, 120.47, 112.70, 111.50, 86.76, 61.36, 60.30, 12.49, 8.56. IR: ν = 686, 726,763, 914, 1030, 1195, 1268, 1376, 1467, 1589, 1632, 1651, 2850, and 2920 cm^{-1}. UV-Vis: λ_{max} = 270 ($\varepsilon = 25.28\times10^3$ $M^{-1}cm^{-1}$), ESI–MS(+) calc. for $C_{32}H_{34}ClIrN_2O_6$ $[M+Na]^+$ = 793.1632, found 793.1664. MP: 83 °C (decompose).

Preparation of Compound 6. A mixture of compound **2** (2.0 g, 7.6 mmol, 1.0 equiv.) and

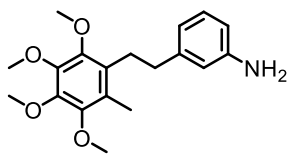

triphenylphosphine (3.0 g, 11.5 mmol, 1.5 equiv.) was refluxed in 65 mL of toluene overnight. The white solid formed was collected by filtration and then dried under vacuum overnight. The phosphonium salt and 3-nitrobenzaldehyde (1.27 g, 8.4 mmol, 1.1 equiv.) were combined in 70 mL of DCM and then treated with a 15 mL a solution of 50 % NaOH in H_2O through dropwise addition (1 drop/sec). The reaction was stirred at room temperature for ~14 h. The organic layer was separated, washed with water (2 x 35 mL), dried over Na_2SO_4, filtered to remove the salt, and concentrated under vacumn. The crude material was purified by silica gel column chromatography (ethyl acetate:hexane, 1:1.5) to afford the desired Wittig product as a colorless oil. This compound was combined with 10% Pd/C (615 mg, 8.6 mmol, 0.1 equiv.) in 150 mL of methanol and stirred for ~14 h under an atmosphere of hydrogen gas at RT. The reaction mixture was then filtered through a pad of celite and the solvent was removed to

obtain compound **7** as clear oil (1.7 g, 70%). ^{1}H NMR ($CDCl_3$, 500 MHz): δ (ppm) = 7.13 (t, J_{HH} = 10 Hz, 1H), 6.79-6.78 (m, 2H), 6.74 (d, J_{HH} = 10 Hz, 1H), 3.92 (s, 3H), 3.91 (s, 3H), 3.85 (s, 3H), 3.79 (s, 3H), 2.86-2.83 (m, 2H), 2.69-2.65 (m, 2H), 2.18 (s, 3H). ^{13}C NMR ($CDCl_3$, 125.7 MHz): δ (ppm) = 147.88, 145.19, 144.75, 143.89, 143.01, 129.59, 129.51, 129.21, 125.19, 121.04, 117.10, 114.81, 61.24, 61.20, 61.13, 60.79, 36.51, 29.34, 11.73. IR: *v* = 693, 877, 1012, 1040, 1069, 1102, 1350, 1405, 1463, 1534, 1685, 2827, 2934, and 3344 cm^{-1}. GC-MS calc. for $C_{19}H_{25}NO_4$ $[M]^+$ = 331.2, found 331.2.

Preparation of Compound 7. The same procedure as that described for the synthesis of

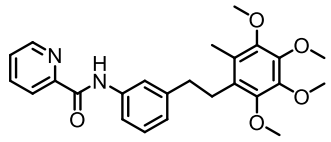

compound **4** was followed, except that picolinic acid (431 mg, 3.5 mmol, 1.75 equiv.) and compound **6** (870 mg, 2 mmol, 1 equiv.) were used instead. The product was obtained as a yellow oil (750 mg, 86%). ^{1}H NMR ($CDCl_3$, 600 MHz): δ (ppm) = 10.01 (s, 1H), 8.63-8.61 (m, 1H), 8.30 (dt, J_{HH} = 7.6, 1.5 Hz, 1H), 7.91 (td, J_{HH} = 7.5, 1.5 Hz, 1H), 7.69-7.67 (m, 1H), 7.64 (s, 1H), 7.47 (ddd, J_{HH} = 7.5, 5.0, 1.0 Hz, 1H), 7.31 (t, J_{HH} = 8.0 Hz, 1H), 7.02 (d, J_{HH} = 7.5 Hz, 1H), 3.92 (s, 3H), 3.91 (s, 3H), 3.84 (s, 3H), 3.77 (s, 3H), 2.91-2.88 (m, 2H), 2.79-2.75 (m, 2H), 2.17 (s, 3H). ^{13}C NMR ($CDCl_3$, 150.9 MHz): δ (ppm) = 162.04, 149.92, 148.05, 147.92, 147.85, 145.23, 144.75, 143.51, 137.81, 129.17, 129.08, 126.55, 125.22, 124.56, 122.46, 119.68, 117.42, 61.24, 61.23, 61.13, 60.79, 36.57, 29.38, 11.76. IR: *v* = 692, 882, 1013, 1042, 1070, 1103, 1350, 1406, 1464, 1534, 1686, 1741, 2857, 2930, and 3342 cm^{-1}. ESI–MS(+) calc. for $C_{25}H_{28}N_2O_5$ $[M+Na]^+$ = 459.1896, found 459.1888.

Preparation of Compound 8. The same procedure as that described for the synthesis of **5**

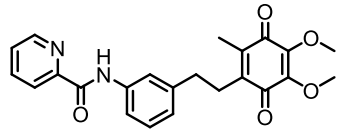

was followed, except that compound **7** (750 mg, 1.72 mmol, 1 equiv.) in 20 mL of THF and CAN (2.1 g, 3.4 mmol, 2.0 equiv.)

in 10 mL of water were used. The pure product was obtained by silica gel column chromatography (ethyl acetate:hexane, 1:1) as an orange solid (390 mg, 56%). ^{1}H NMR ($CDCl_3$, 400 MHz): δ (ppm) = 10.01 (s, 1H), 8.62-8.60 (m, 1H), 8.27 (dt, J_{HH} = 7.5, 1.0 Hz, 1H), 7.90 (td, J_{HH} = 7.5, 1.5 Hz, 1H), 7.68 (s, 1H), 7.61-7.58 (m, 1H), 7.48 (ddd, J_{HH} = 7.5, 5.0, 1.0 Hz, 1H), 7.29 (t, J_{HH} = 7.5 Hz, 1H), 6.97 (d, J_{HH} = 7.5 Hz, 1H), 3.98 (s, 3H), 3.98 (s, 3H), 2.81-2.77 (m, 2H), 2.74-2.71 (m, 2H), 1.89 (s, 3H). ^{13}C NMR ($CDCl_3$, 50.91 MHz): δ (ppm) = 184.58, 184.07, 162.01, 149.76, 148.04, 144.51, 144.33, 142.05, 141.55, 139.64, 137.94, 137.94, 137.83, 129.26, 126.60, 124.57, 122.42, 119.77, 117.67, 61.27, 61.24, 34.81, 28.73, 11.98. IR: *v* = 692, 739, 844, 1037, 1152, 1205, 1257, 1442, 1526, 1592, 1592, 1609, 1643, 1676, 2948, and 3315 cm^{-1}. ESI–MS(+) calc. for $C_{23}H_{22}N_2O_5$ $[M+Na]^+$ = 429.1426, found 429.1428. MP: 80–82 °C.

Preparation of Complex Ir3a. In a round bottom flask $[Cp^*IrCl_2]_2$ and (160 mg, 0.2 mmol, 1.0 equiv.) and the ligand **8** (170.5 mg, 0.42 mmol, 2.1 equiv.) were added into 20 mL of degassed ethanol and stirred for 15 min at 80 °C. The reaction mixture was treated with ammonium hexafluorophosphate (147 mg, 0.9 mmol, 4.5 equiv.) and stirred overnight at 80 °C. The ethanol solvent was removed by rotary evaporation to obtain a dark yellow solid. The final product was obtained by precipitating the Ir complex out of DCM using hexane (140 mg, 45%). ^{1}H NMR ($CDCl_3$, 500 MHz): δ (ppm) = 8.56 (d, J_{HH} = 5.2 Hz, 1H), 8.13 (d, J_{HH} = 7.6 Hz, 1H), 7.92 (t, J_{HH} = 7.6 Hz, 1H), 7.53-7.46 (m, 3H), 7.25-7.21 (m, 1H), 6.94 (d, J_{HH} = 7.6 Hz, 1H), 3.99 (s, 3H), 3.98 (s, 3H), 2.79-2.77 (m, 2H), 2.71-2.69 (m, 2H), 1.95 (s, 3H), 1.40 (s, 15H). ^{13}C NMR ($CDCl_3$, 100.5 MHz): δ (ppm) = 184.69, 184.14, 168.58, 155.66, 149.79, 148.38, 144.47, 144.40, 141.90, 140.63, 139.63, 138.70, 128.29, 127.57, 126.97, 126.37, 124.94, 86.66, 61.28, 61.26, 34.71, 28.64, 12.08, 8.52. IR: *v* = 686, 763, 1030, 1076, 1151,

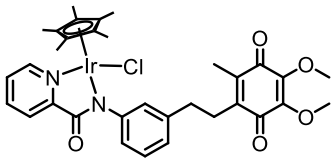

1204, 1263, 1377, 1447, 1594, 1644, and 2921 cm^{-1}. UV-Vis: λ_{max} = 272 ($\varepsilon = 20.0\times10^3$ M^{-1} cm^{-1}), ESI–MS(+) calc. for $C_{33}H_{36}ClIrN_2O_5$ $[M+Na]^+$ = 791.1840, found 791.1850. Anal. Calc for $C_{33}H_{36}ClIrN_2O_5$: MP: 125–126 °C.

Preparation of Complex Ir3d. Inside the glovebox, excess $NaB(OAc)_3H$ (138 mg, 0.66 mmol, 3.0 equiv.) was added to a solution of **Ir3a** (167 mg, 0.22 mmol, 1.0 equiv.) in DCM. The reaction mixture was stirred for 2 h at room temperature. The organic mixture was washed with water three times and then dried under vacuum for 2 h. The final product was obtained as a pale orange solid (118 mg, 73%). ^{1}H NMR (MeOD, 600 MHz): δ (ppm) = 8.77 (d, J_{HH} = 0.6 Hz, 1H), 7.92-7.88 (m, 2H), 7.45-7.43 (m, 1H), 7.28 (t, J_{HH} = 0.9 Hz, 2H), 7.14 (s, 3.79 (s, 6H), 2.90-2.87 (m, 2H), 2.72 (t, J_{HH} = 1.2 Hz, 2H), 2.14 (s, 3H), 1.53 (s, 15H), -11.30 (s, 1H). ^{13}C NMR (MeOD, 150.9 MHz): δ (ppm) = 168.42, 154.96, 151.96, 148.54, 142.98, 140.55, 140.48, 138.70, 136.36, 127.95, 126.63, 126.55, 125.42, 124.24, 123.83, 122.81, 118.10, 88.18, 59.84, 59.76, 35.52, 28.81, 10.42. IR: ν = 684, 823, 956, 1032, 1102, 1380, 1574, 1618, 2034, and 2916 cm^{-1}. UV-Vis: λ_{max} = 269 ($\varepsilon = 8.5\times10^3$ $M^{-1}cm^{-1}$), ESI–MS(+) calc. for $C_{33}H_{39}IrN_2O_5$ $[M+Na]^+$ = 759.2386, found 759.2404. MP: 130 °C (decompose).

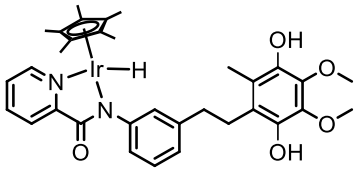

Preparation of Complex Ir3c. Inside the glovebox, **Ir3d** (118 mg, 0.18 mmol) was treated with one drop of HCl in Et_2O and stirred in 2 mL of $CDCl_3$ for 2 h. The organic mixture was washed with water 3 times and then dried under vacuum for 2 h. The final product was obtained as a pale orange solid (125 mg, 89%). ^{1}H NMR (MeOD, 600 MHz): δ (ppm) = 8.77 (s, 1H), 8.08-8.05 (m, 1H), 7.99 (d, J_{HH} = 0.6 Hz, 1H), 7.68-7.66 (m, 1H), 7.44 (s, 1H), 7.31-7.25 (m, 2H), 7.07-7.04 (m, 1H), 3.79 (s, 6H), 2.90-2.87 (m, 2H), 2.74-2.71 (m, 2H), 2.14 (s,

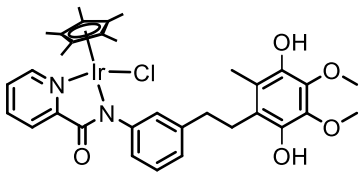

3H), 1.37 (s, 13H). ^{13}C NMR ($CDCl_3$, 100.5 MHz): δ (ppm) = 168.31, 153.42, 151.41, 146.42, 143.52, 140.57, 140.49, 139.42, 138.73, 138.46, 128.87, 128.39, 126.08, 125.84, 125.61, 123.06, 122.59, 118.10, 87.75, 59.84, 59.76, 35.39, 28.67, 10.47, 7.16. IR: ν = 685, 731, 760, 955, 1031, 1096, 1378, 1426, 1560, 1589, 1618, and 2930 cm^{-1}. UV-Vis: λ_{max} = 291 ($\varepsilon = 9.8\times10^3$ M^{-1} cm^{-1}), ESI–MS(+) calc. for $C_{33}H_{38}ClIrN_2O_5$ $[M+Na]^+$ = 793.1996, found 793.5092. MP: 130 °C (decompose).

2.4.3 X-ray Crystallographic Data

Single crystal of complex **Ir3a** was grown from vapor diffusion of pentane into a solution of the complex in acetone. The yellow orange crystals were mounted at -150 °C on a Bruker diffractometer equipped with a CCD APEX II detector using Mo-Kα radiation. Data reduction was performed within the APEX II software and empirical absorption corrections were applied using SADABS. The structures were solved by direct methods in SHELXS and refined by full-matrix least squares based on F2 using SHELXL. All non-hydrogen atoms were located and refined anisotropically. Hydrogen atoms were fixed using a riding model and refined isotropically. The acetone solvent molecule was located on an inversion center and was refined with half occupancy using a negative part number to suppress generation of special position constraints and bonds to symmetry-related atoms.

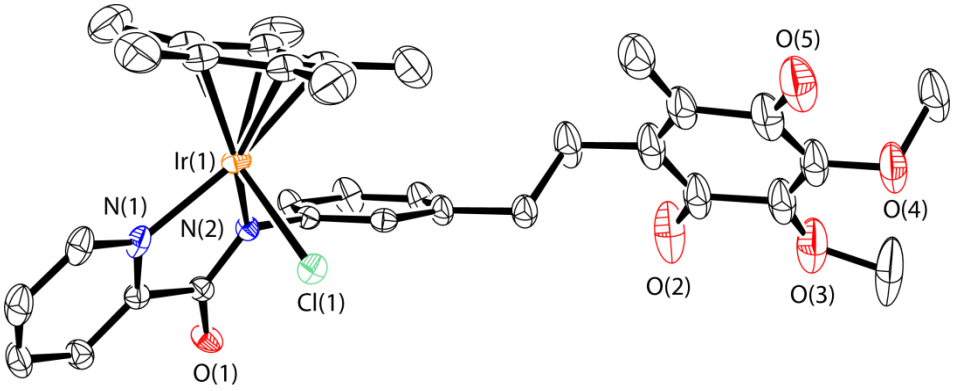

Figure 2.12 The molecular structure of **Ir3a**.

The structure shown in ORTEP view with displacement ellipsoids drawn at 50% probability level. The hydrogen atoms and acetone solvent molecule have been omitted for clarity.

Table 2.3 Crystallographic Table for Complex **Ir3a**.

	Ir3a·acetone
Empirical Formula	$(IrC_{33}H_{35}ClN_2O_5)\cdot(C_3H_6O)_{0.5}$
Formula Weight	796.32
Temperature (°C)	-150
Wavelength (Å)	0.71073
Crystal System,	Triclinic,
Space Group	P-1
Unit Cell Dimensions	
a (Å)	7.7989(15)
b (Å)	9.4618(18)
c (Å)	24.171(5)
α (°)	95.058(2)
β (°)	94.646(3)
γ (°)	112.464(2)
Volume ($Å^3$)	1629.0(5)
Z, Calculated Density (Mg/m^3)	2, 1.623
Absorption Coefficient (mm^{-1})	4.225
F(000)	794
Crystal Size (mm^3)	0.20 x 0.17 x 0.1
Theta Range for Data Collection (°)	0.852 to 26.372
Limiting Indices	$-9 \le h \le 8$ $-11 \le k \le 11$ $-21 \le l \le 29$
Reflections Collected/ Unique	8585 / 6530 [R(int) = 0.0114]
Completeness	99.1%
Absorption Correction	Empirical
Max. and Min. Transmission	0.7456 and 0.5454
Refinement Method	Full-Matrix Least–Squares on F^2
Data/ Restraints/ Parameters	6530 / 107 / 356
Goodness of Fit on F^2	1.322
Final R Indices	R_1= 0.0478
[I > 2σ(I)]	wR_2 = 0.1170
R Indices (All Data)*	R_1 = 0.0488
	wR_2 = 0.1188
Largest Diff. Peak and Hole (e $Å^{-3}$)	2.713 and -2.168

*$R_1 = \Sigma\,||F_o|-|F_o||/\Sigma|F_o|$; $wR_2 = [\Sigma[w(F_o^2 - F_c^2)^2]/\Sigma[w(F_o^2)_2]]^{1/2}$; GOF = $[\Sigma[w(F_o^2 - F_c^2)_2]/(n-p)]^{1/2}$, where *n* is the number of reflections and *p* is the total number of parameters refined.

2.4.4 General Procedure for Transfer Hydrogenation of Ir3a

Procedure: Stock solutions of **Ir1**, **Ir2**, **Ir3a** and **Q1** were prepared in DMSO at a concentration of 10 mM and stored in the freezer for subsequent use. Solutions containing H_2O_2 and NaHCOO (100 mM) in water were freshly prepared each time. Reactions were performed in 20 mL vials at room temperature. In each experiment, the catalyst and quinone stock solutions were diluted to concentrations ranging from 15 to 50 μM. Additional DMSO was added to maintain a constant co-solvent concentration of 1% in 10 mL of solvent. To 10 mL of this mixture, 20 equiv. of NaHCOO relative to the Ir complex or quinone, was added. The H_2O_2 concentration was monitored using Quantofix H_2O_2 test strips every 1 h. The amount of peroxide present was determined based on the grayscale intensity of the test strip after exposure to the reaction mixture for 30 sec. Each set of experiments was repeated two times to confirm that the trends observed were consistent and reproducible.

Decomposition of H_2O_2 in the Presence of Ir Complexes: Stock solutions of **Ir1**, **Ir3a**, and **Q1** were prepared as described above and then diluted to 10 μM. Solutions containing 30 μL of either the Ir complex or quinone were treated with H_2O_2 (5 μL). No sodium formate was used in these experiments. The reactions were followed for 22 h by periodically measuring the peroxide concentration using the H_2O_2 test strips. Decrease in the concentration of H_2O_2 was observed over time in the presence of the iridium complexes.

Analysis of Peroxide Test Strips: Photos of the original-colored test strips were taken using an iPhone Xs Max under normal lab lighting. The colored photos were converted to 8-bit grayscale and the mean gray intensity was determined using the area selection tool in ImageJ. The grayscale intensity was then converted to peroxide concentration using the equation: [peroxide concentration] = $1000880\ e^{(-0.050755 \times \text{intensity})}$, which was obtained from an

exponential fit of the intensity data obtained by converting the color scale provided by the manufacturer to grayscale (Fig. 2.13). This method of peroxide concentration determination is meant only to be semi-quantitative since errors associated with inhomogeneous photo lighting, test strip response, and other uncontrolled experimental factors could affect the accuracy of the results.

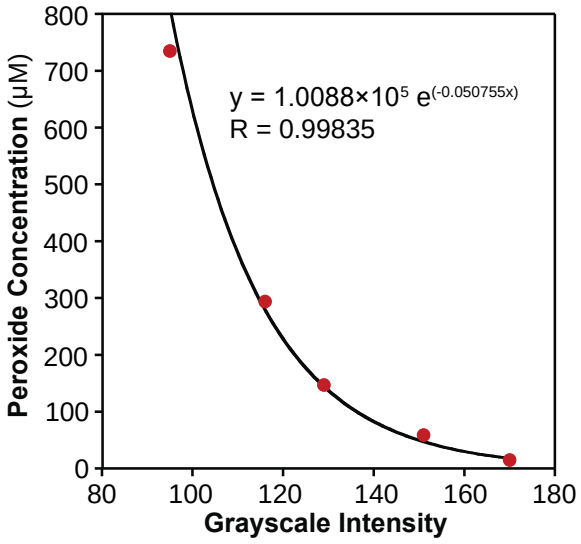

Figure 2.13 Correlation between the H_2O_2 concentration and the converted grayscale of Quantofix test strip.

A best fit of the data points provided an exponential equation relating the grayscale intensity with peroxide concentration.

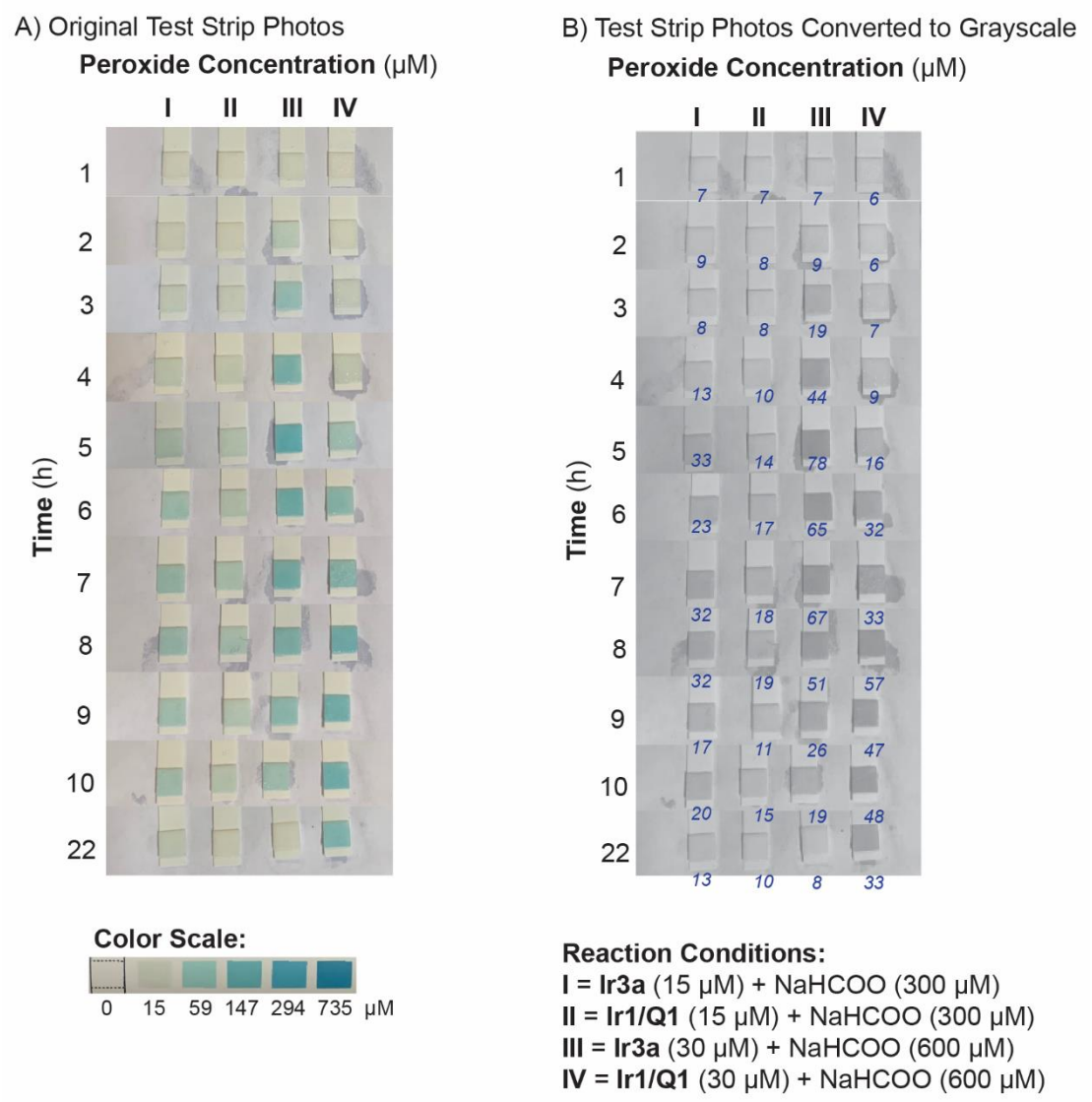

Figure 2.14 Photos of the test strips obtained from a time study of the formation of hydrogen peroxide by Ir complexes and NaHCOO.

(Part A: original; Part B: converted to grayscale). The blue numbers in the grayscale image indicate the peroxide concentration of the test area. The reactions were carried out in 10 mL of solvent (1% DMSO in water) using the concentration of reagents given above.

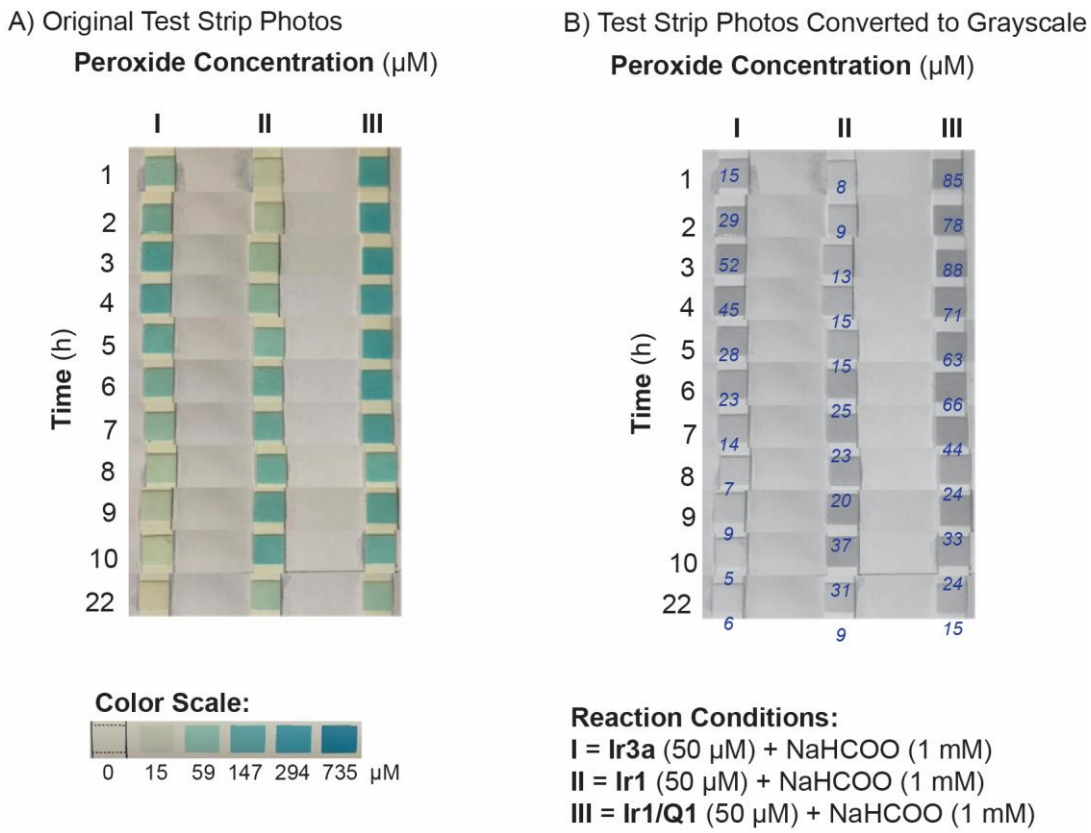

Figure 2.15 Photos of the test strips obtained from a time study of the formation of H_2O_2 by Ir complexes and NaHCOO

(Part A: original; Part B: converted to grayscale). The blue numbers in the grayscale image indicate the peroxide concentration of the test area. The reactions were carried out in 10 mL of solvent (1% DMSO in water) using the concentration of reagents given above.

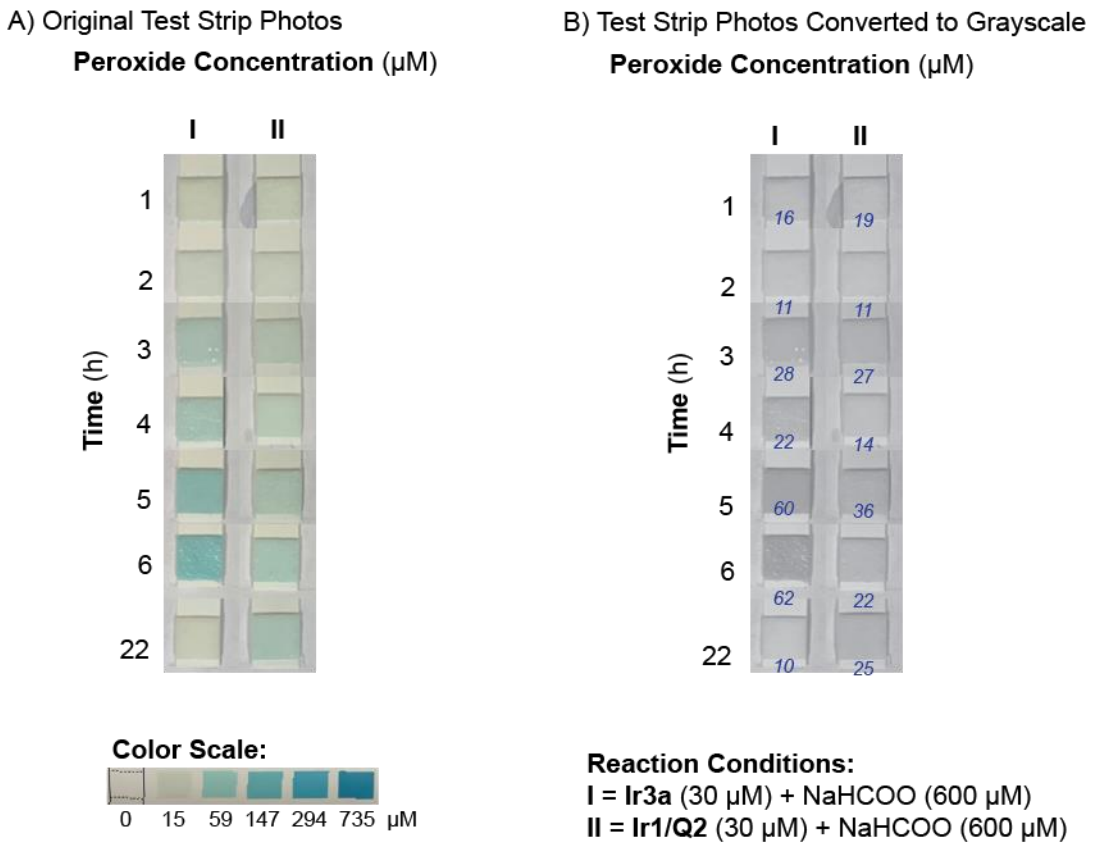

Figure 2.16 Photos of the test strips obtained from a time study of the formation of hydrogen peroxide by Ir complexes and NaHCOO.

(Part A: original; Part B: converted to grayscale). The blue numbers in the grayscale image indicate the peroxide concentration of the test area. The reactions were carried out in 10 mL of solvent (1% DMSO in water) using the concentration of reagents given above.

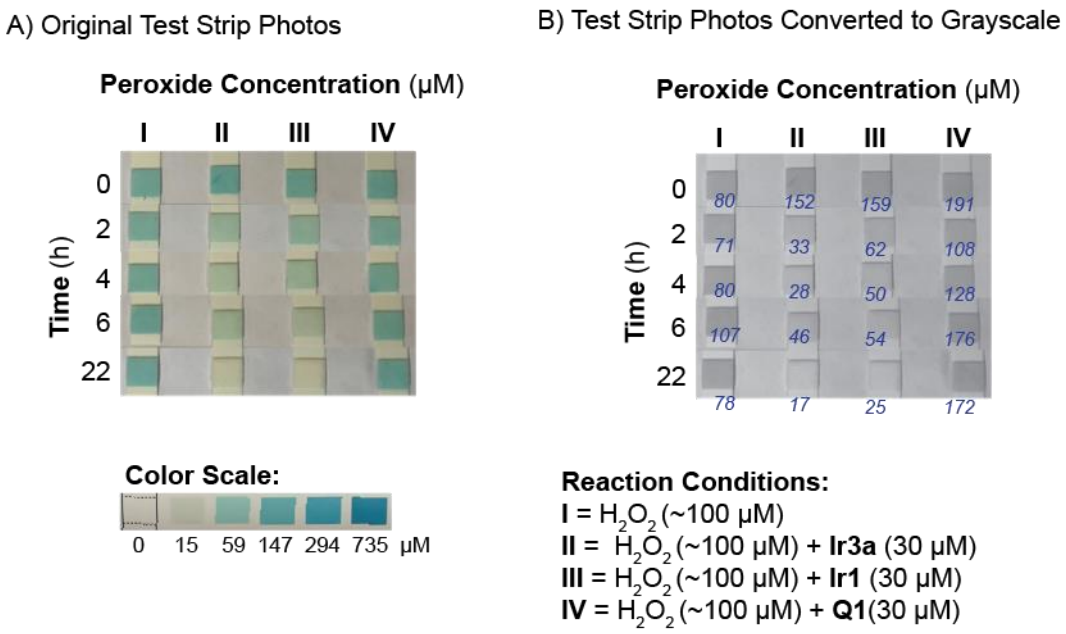

Figure 2.17 Photos of the test strips obtained from a time study of the decomposition of H_2O_2 in the presence and absence of Ir complexes.

(Part A: original; Part B: converted to grayscale). The blue numbers in the grayscale image indicate the peroxide concentration of the test area. The reactions were carried out in 10 mL of solvent (1% DMSO in water) using the concentration of reagents given above. The wide variation in the starting H_2O_2 concentration (e.g., from 80-191 μM at time = 0 h) was attributed to slightly different amounts of H_2O_2 added since the total volume of H_2O_2 used was very low (~5 μL); however, in these experiments, we were interested in the *relative changes* over time rather than the absolute amounts of H_2O_2 present, which would require more rigorous analytical studies.

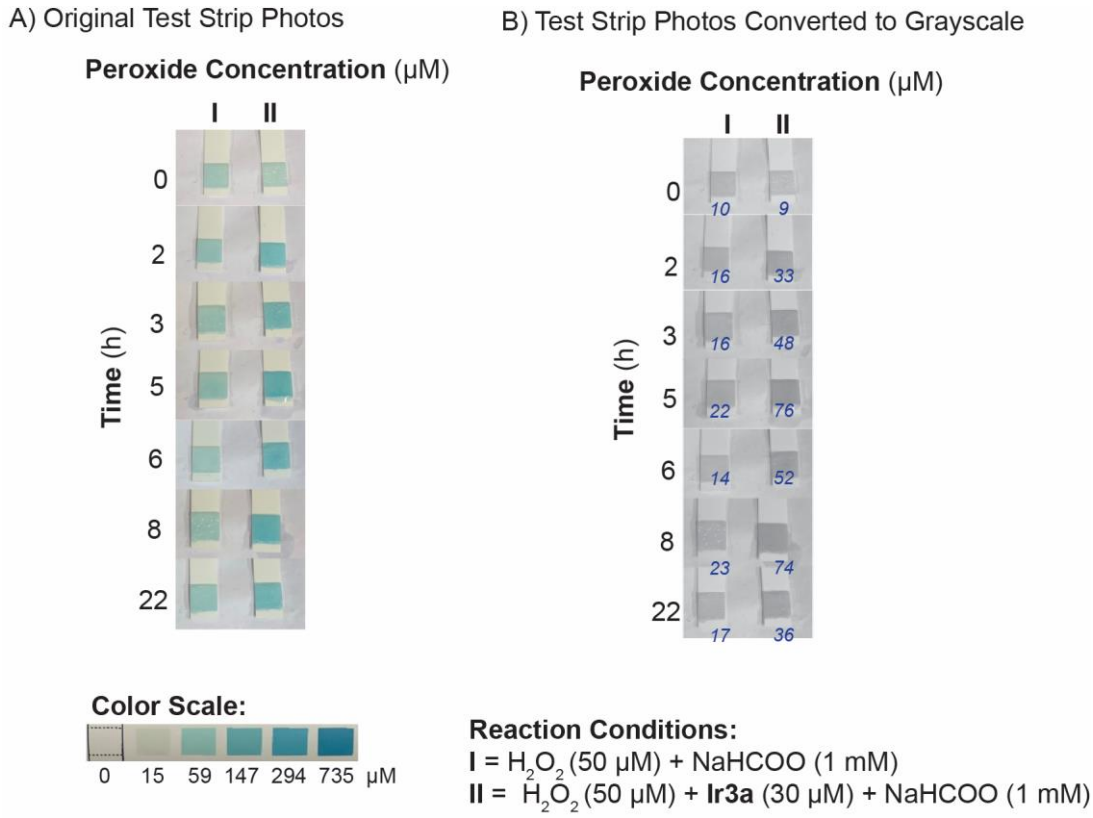

Figure 2.18 Photos of the test strips obtained from a time study of the decomposition of hydrogen peroxide in the presence and absence of **Ir3a** and NaHCOO.

(Part A: original; Part B: converted to grayscale). The blue numbers in the grayscale image indicate the peroxide concentration of the test area. The reactions were carried out in 10 mL of solvent (1% DMSO in water) using the concentration of reagents given above.

2.4.5 Reaction Monitoring by NMR Spectroscopy

Procedure for reaction of Ir1 with NaHCOO: A mixture of catalyst **Ir1** (5 mg, 6.5 μmol) and NaHCOO (2.2 mg, 5 equiv.) was prepared in the glove box. A 1.2 mL solution of acetone-d_6 /D_2O (9:1) was used to dissolve this mixture. The NMR spectrum was measured immediately, which showed that NaHCOO was completely consumed. This sample was then divided equally into 2 NMR tubes. One was kept at 40 ℃ °under an inert atmosphere whereas the other was exposed to air. Both samples were then monitored by NMR spectroscopy. The air exposed sample showed significant **Ir1** decomposition, as indicated by the disappearance of the ^{1}H NMR peaks corresponding to the ether linkage.

Procedure for reaction of Ir3a with NaHCOO: A 100 mM stock solution of **Ir3a** in CD_3OD was prepared in the glovebox. A 25 μL aliquot of this solution was diluted with 450 μL of CD_3OD in a J-Young NMR tube. The NMR tube was cooled to -40 °C inside the spectrometer and then the spectrum of the starting compound was measured. The sample was ejected, treated with a -40 °C solution containing 50 μL of NaHCOO (100 mM) in CD_3OD, and then quickly reinserted back into the NMR spectrometer. The temperature was slowly increased at a rate of 5 °C /10 min up to 15 °C and NMR spectra were recorded at -35, -20, 0, 10, and 15 °C. Finally, the NMR sample was warmed to RT, removed from the instrument, and the solution was exposed to air overnight. This sample was analyzed by NMR spectroscopy to confirm the reduced species was oxidized by air. Alternatively, the final NMR sample was treated with excess sodium formate and then recorded by NMR spectroscopy to observe the formation of **Ir3d**.

Quantification of turnover number: The following reagents from individually prepared stock solutions were combined in a 3 mL scintillation vial: NaHCOO (20 μmol) and

methyl benzyl alcohol as an internal standard (10 μmol) in 1 mL of D_2O/DMSO-d_6 (9:1). This solution was stirred for 1 min. The sample was prepared by taking out a 100 μL aliquot of the mixture and combining it with 300 μL of D_2O/DMSO-d_6 (9:1). The Ir catalyst (0.45 μmol) was then added to the vial and the reaction was monitored directly by NMR spectroscopy at 6 and 21 h.

Procedure for reaction of Ir3a with NaHCOO/nPr_2S: The appropriate volumes of stock solutions containing the following reagents were combined in a 20 mL scintillation vial: NaHCOO (100 μmol), **Ir3a** (2 μmol) and *n*Pr_2S (200 μmol) in 10 mL of H_2O/DMSO (95:5). This solution was stirred at room temperature for 18 h. After the reaction was complete, the organic compounds were extracted into dichloromethane (2×1 mL), dried over Na_2SO_4, filtered, to remove the drying agent, and characterized by NMR spectroscopy. A control experiment was set up following the same procedure except *n*Pr_2S was not added. Measurement of the samples by NMR spectroscopy confirmed that *n*Pr_2S did not inhibit the catalyst activity of **Ir3a** since NaHCOO was still consumed.

2.4.6 Procedure for In Vitro Experiments

Cell cytotoxicity studies: Cells A2780 were seeded in a 96-well plate (7,000-10,000 cells/well) and incubated at 37 ℃ in a culture incubator with a humidified atmosphere containing 5% CO_2 to allow cells to adhere to the bottom of the wells (~18 h). Stock solutions of tested compound were prepared in DMSO, then diluted in cell culture media (Dulbecco's Modified Eagle Medium (DMEM):F12 (1:1) supplemented with 10% fetal bovine serum (FBS) and 1% penicillin-streptomycin 100X solution) to make a series of desired concentrations. Cell culture medium was replaced by new cell culture media with test compounds at different concentrations, and cells were incubated for a 24 h. After that, the

medium was aspirated, and the cells were washed with fresh cell culture medium before 100 μL of cell culture medium (with no FBS) was added to each well, followed by 50 μL of fixative reagent (Cytoscan™ SRB Cytotoxicity Assay, G-Biosciences, catalog #786-213). The well plate was kept at 4 ℃ in 1 h, then the cells was washed three times with distilled water before drying 2-3 h at 37 ℃. 100 μL of sulforhodamine B (SRB) dye solution was then added to each well and the 96 well plate was kept in the dark at room temperature for 30 minutes. The cells were washed four times with 1x dye wash solution before drying 2-3 h at 37 ℃ 200 μL of SRB solubilization buffer was added to each well, mixed by pipetting up and down to dissolve the dye completely. The absorbance of the 96-well plate was then measured at 495 nm to determine the amount of rhodamine complex formed. Cell viability was considered to be proportional to the absorbance of the wells. The absorbance value of the wells containing only solubilization buffer (background) was subtracted from those of the wells containing treated and control cells. Cell viability was determined following this equation: % Cell viability = ($A_{conc}/A_{control}$)x100%, where A_{conc} is the absorbance at a specific probe concentration and $A_{control}$ is the absorbance of the untreated cells sample. IC_{50} value was calculated from the sigmoidal curve fit of this data at 50% cell alive.

Sodium formate co-treatment studies:

A similar to cytotoxicity study was used with a slight modification when treating cells. A549 cells were incubated with catalysts at 1/3 of their IC_{50} values for 24 h. After that, the cells were washed three times with clean media, and then be treated with HCOONa at 0.5, 1.0, and 2.0 mM, respectively for another 24 h. The standard procedure of SRB assay was then performed to determine cell viability in each treatment.

2.5 Spectral Characterization

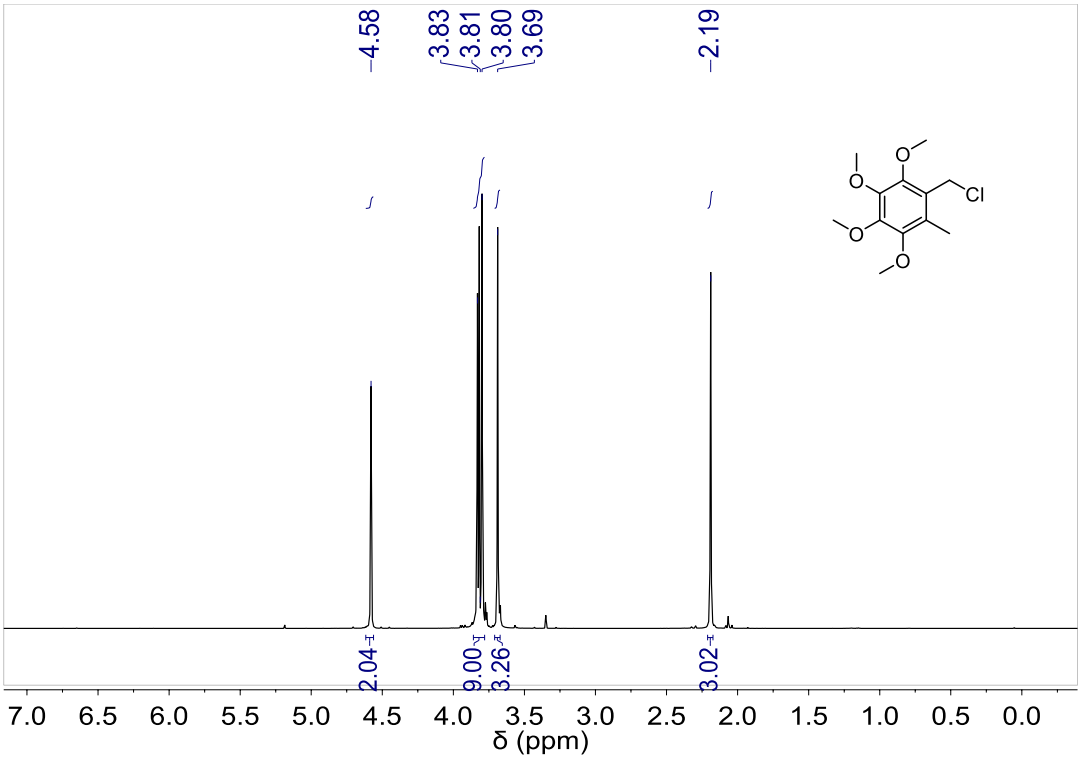

Figure 2.19 ^{1}H NMR spectrum ($CDCl_3$, 600 MHz) of compound **2**.

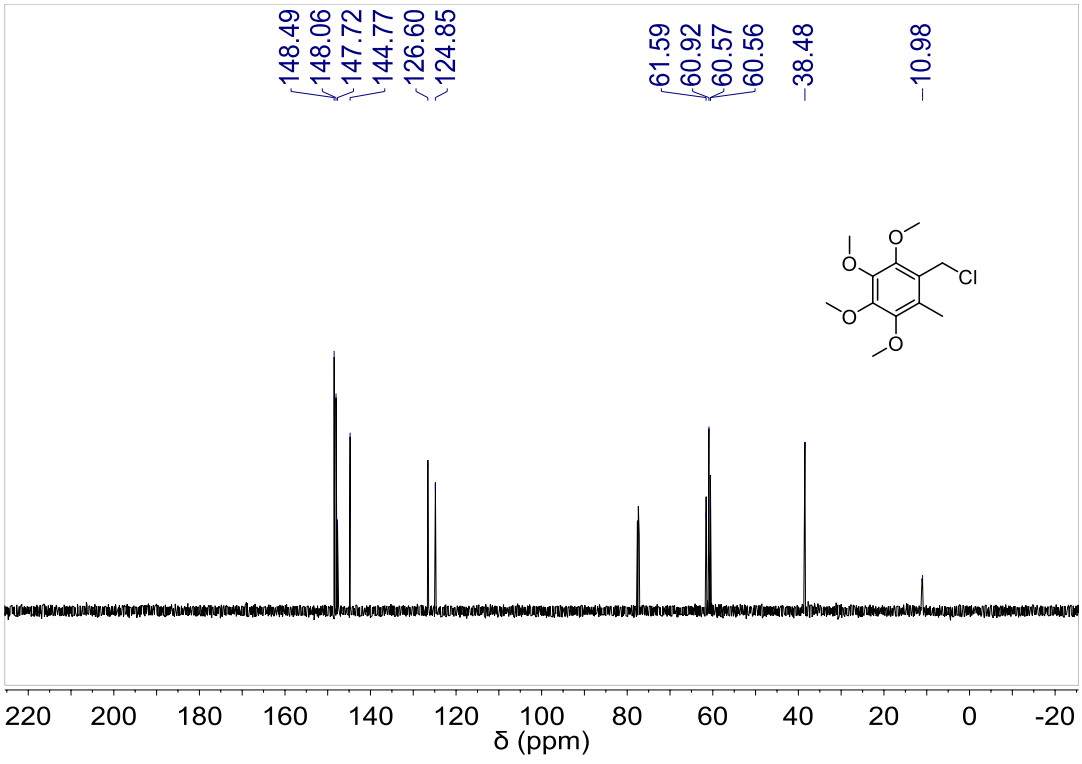

Figure 2.20 ^{13}C NMR spectrum ($CDCl_3$, 151 MHz) of compound **2**.

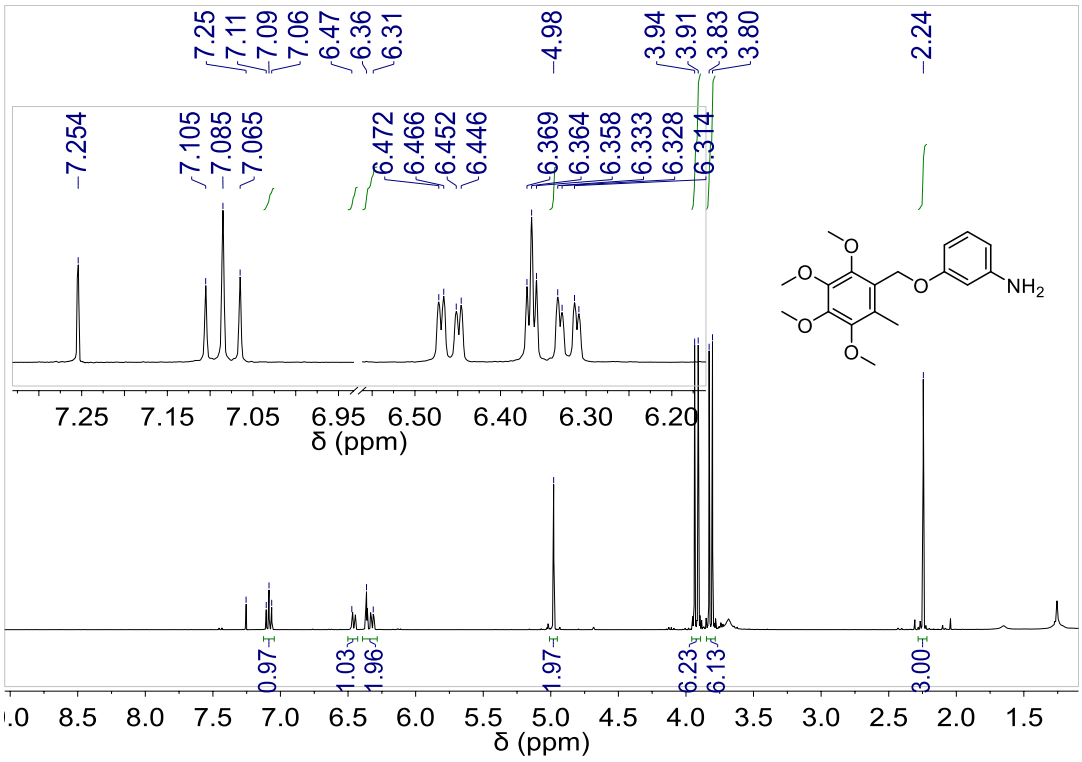

Figure 2.21 ^{1}H NMR spectrum ($CDCl_3$, 400 MHz) of compound **3**.

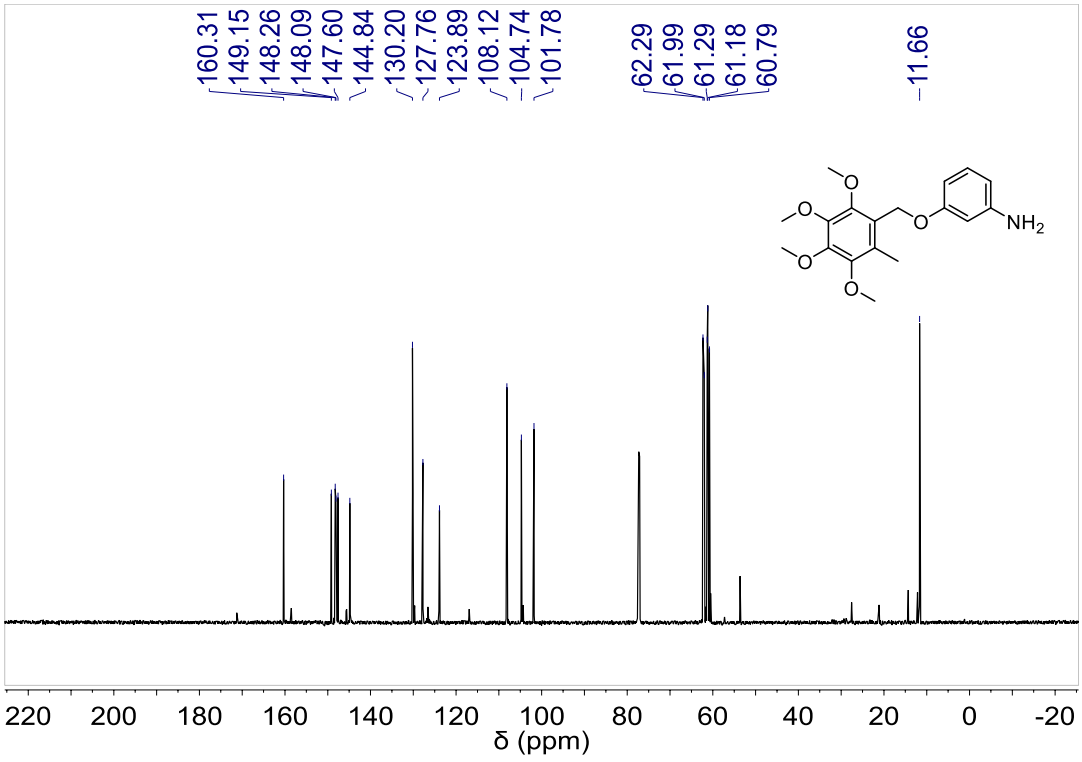

Figure 2.22 ^{13}C NMR spectrum ($CDCl_3$, 151 MHz) of compound **3**.

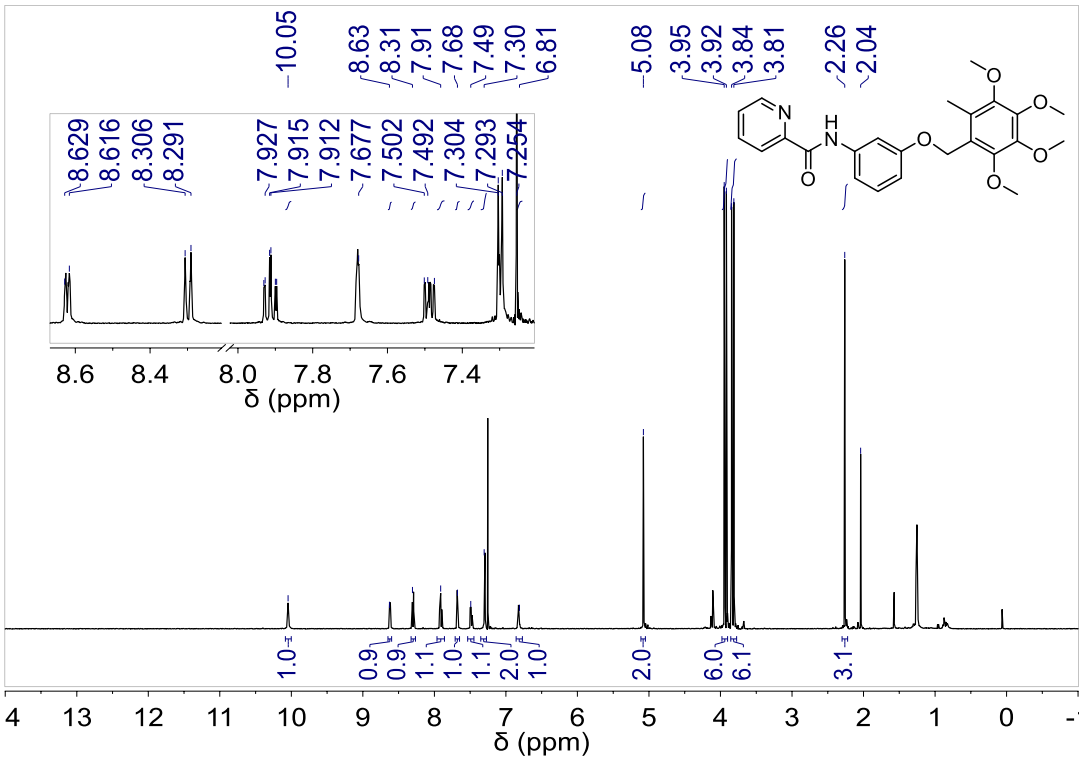

Figure 2.23 ^{1}H NMR spectrum ($CDCl_3$, 500 MHz) of compound **4**.

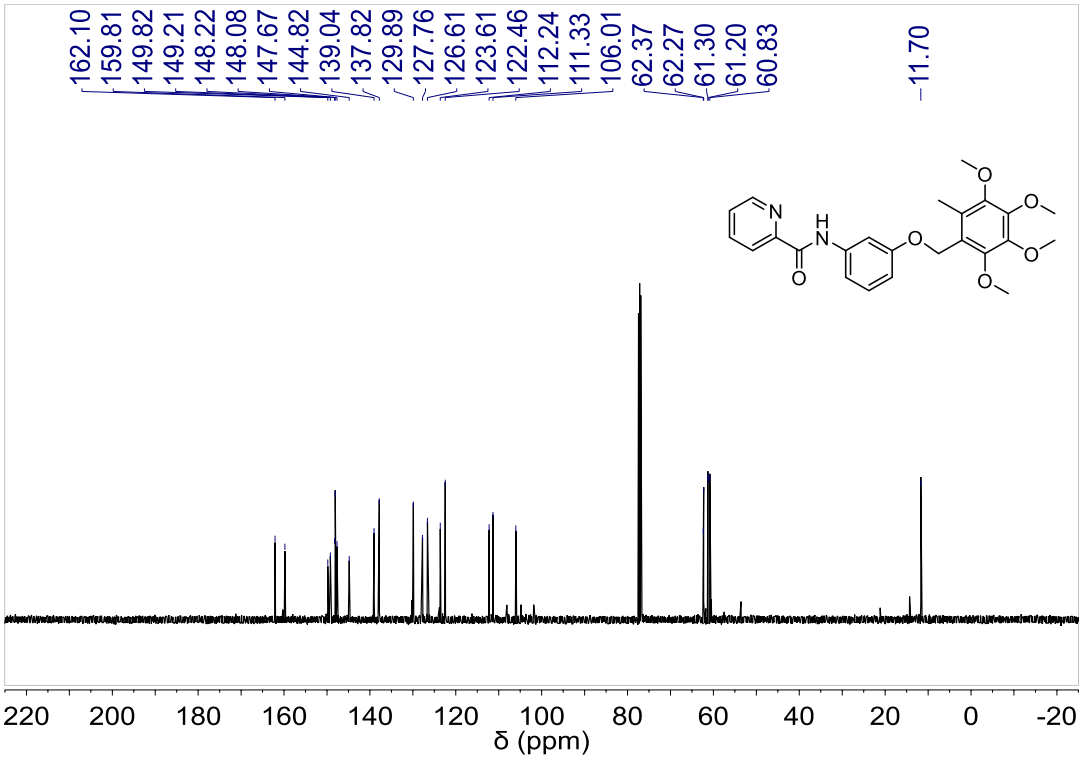

Figure 2.24 ^{13}C NMR spectrum ($CDCl_3$, 126 MHz) of compound **4**.

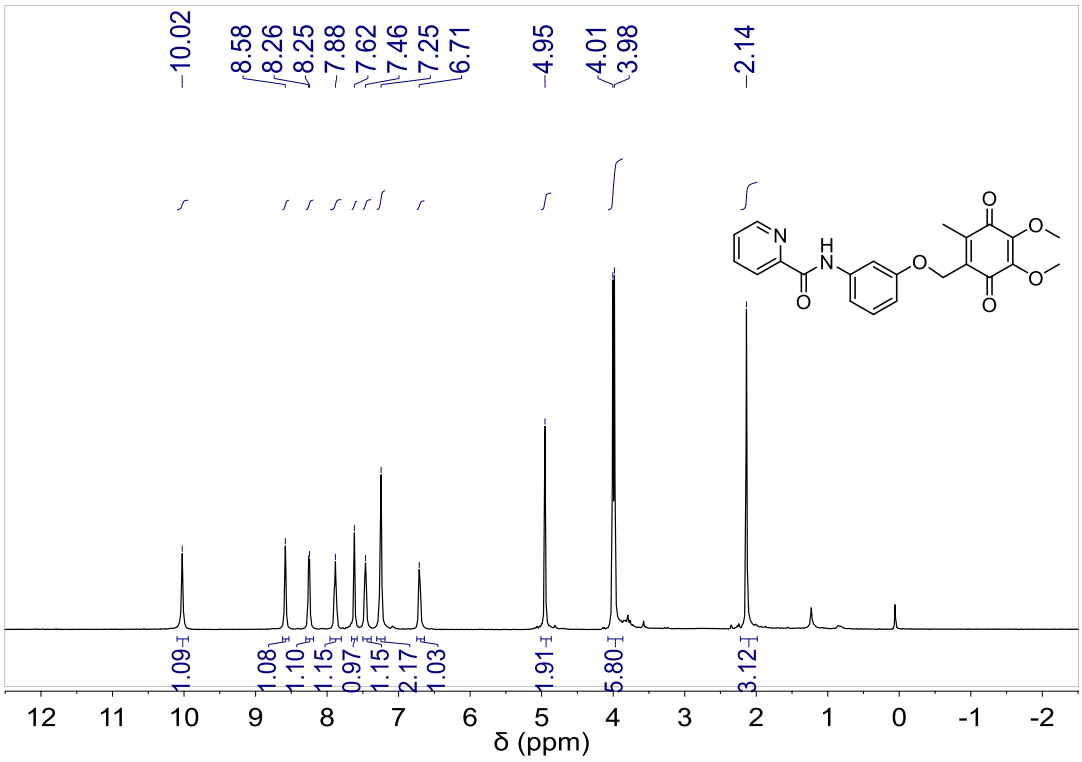

Figure 2.25 ^{1}H NMR spectrum ($CDCl_3$, 500 MHz) of compound **5**.

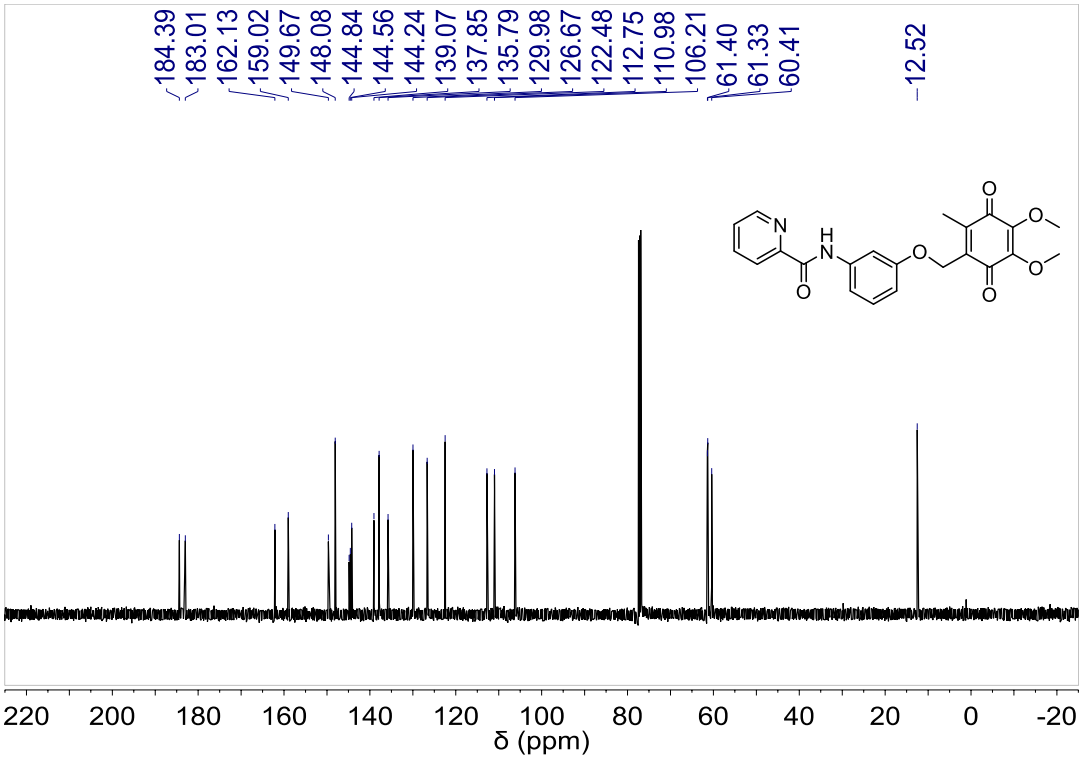

Figure 2.26 ^{13}C NMR spectrum ($CDCl_3$, 126 MHz) of compound **5**.

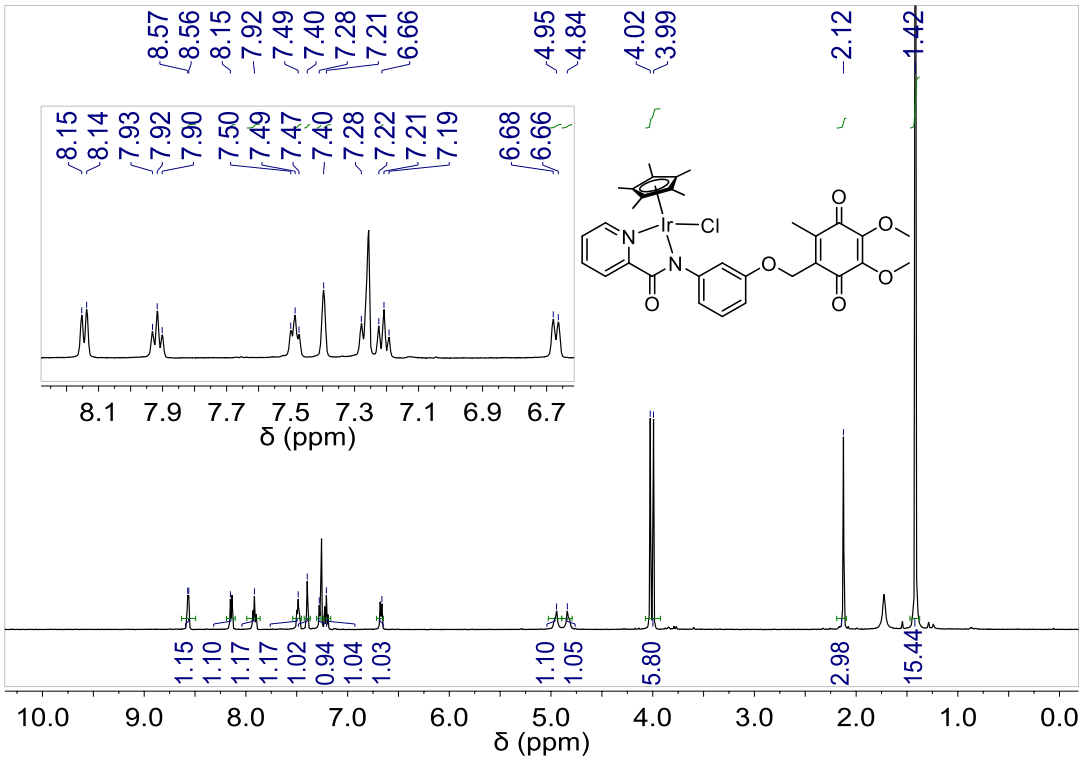

Figure 2.27 ^{1}H NMR spectrum ($CDCl_3$, 500 MHz) of compound **Ir2**.

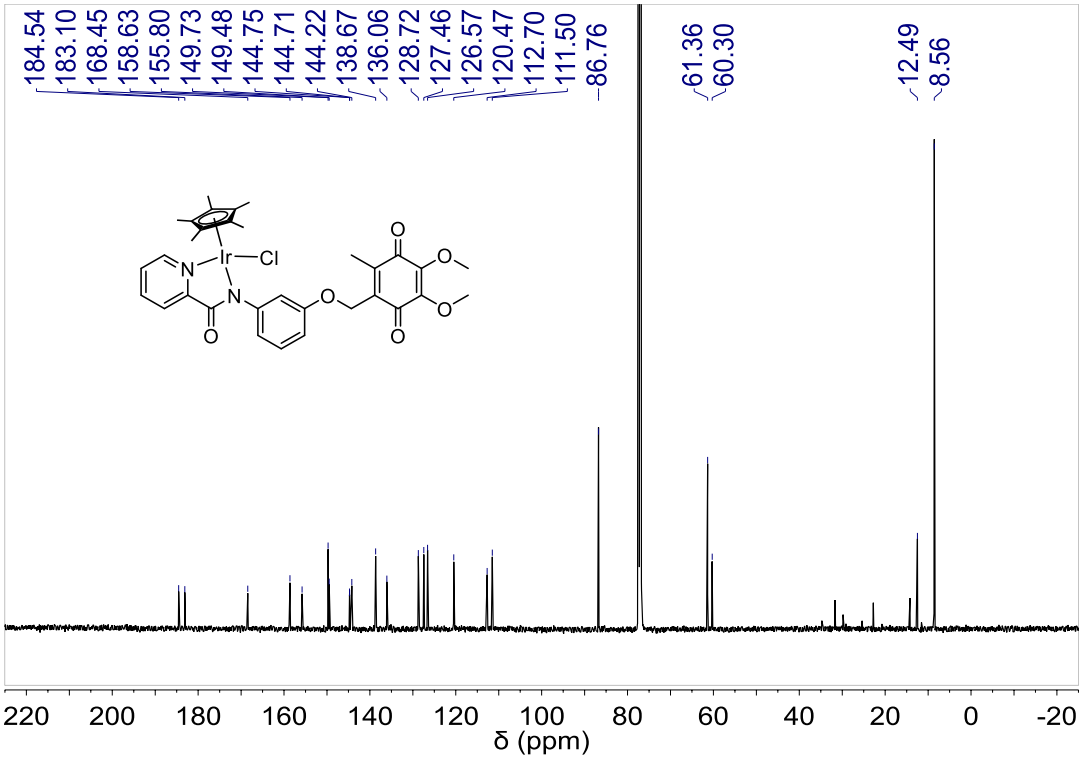

Figure 2.28 ^{13}C NMR spectrum ($CDCl_3$, 126 MHz) of compound **Ir2.**

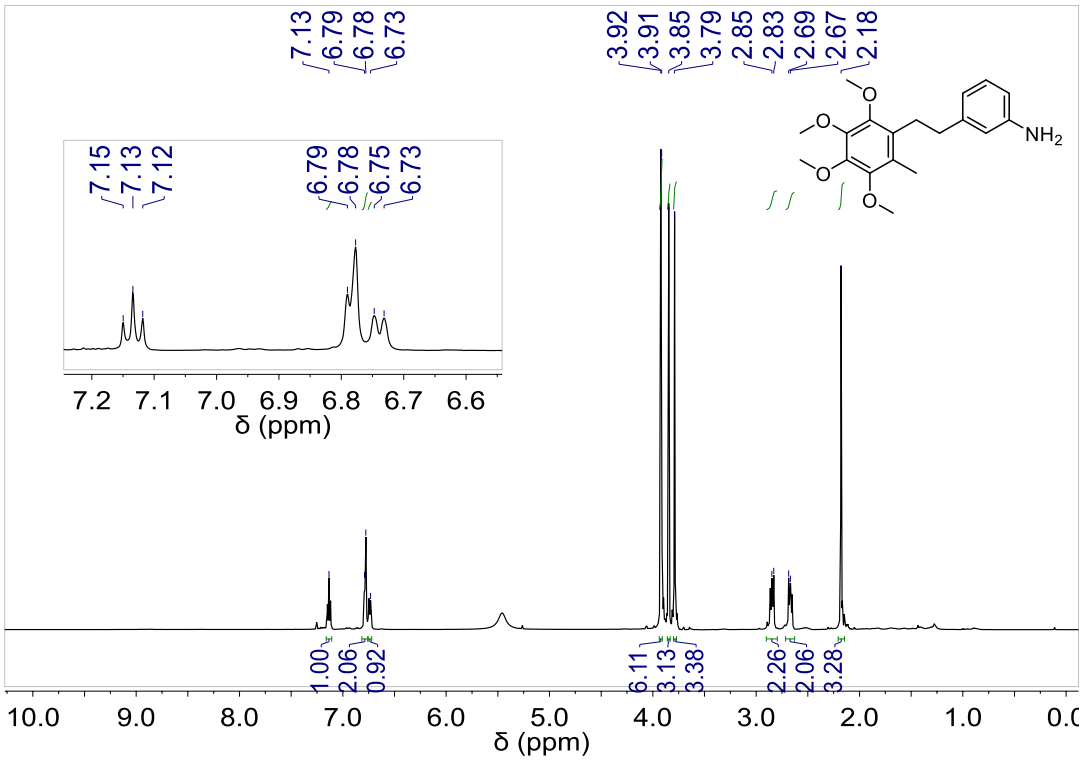

Figure 2.29 ^{1}H NMR spectrum ($CDCl_3$, 500 MHz) of compound **6**.

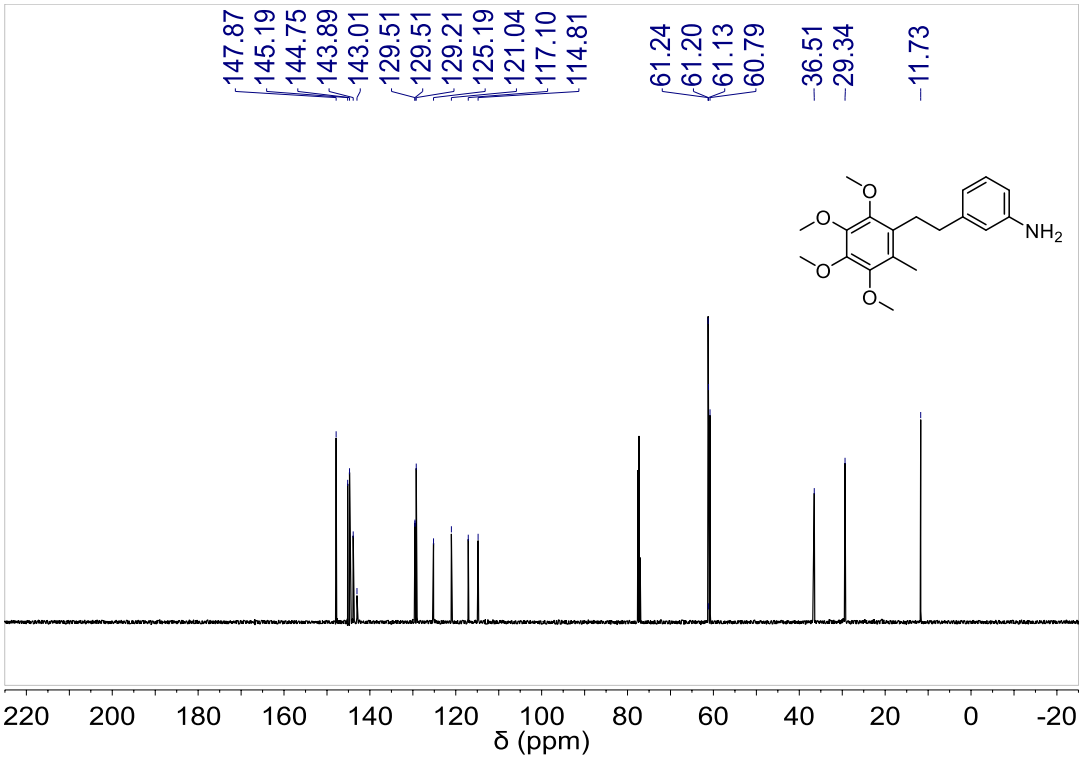

Figure 2.30 ^{13}C NMR spectrum ($CDCl_3$, 126 MHz) of compound **6**.

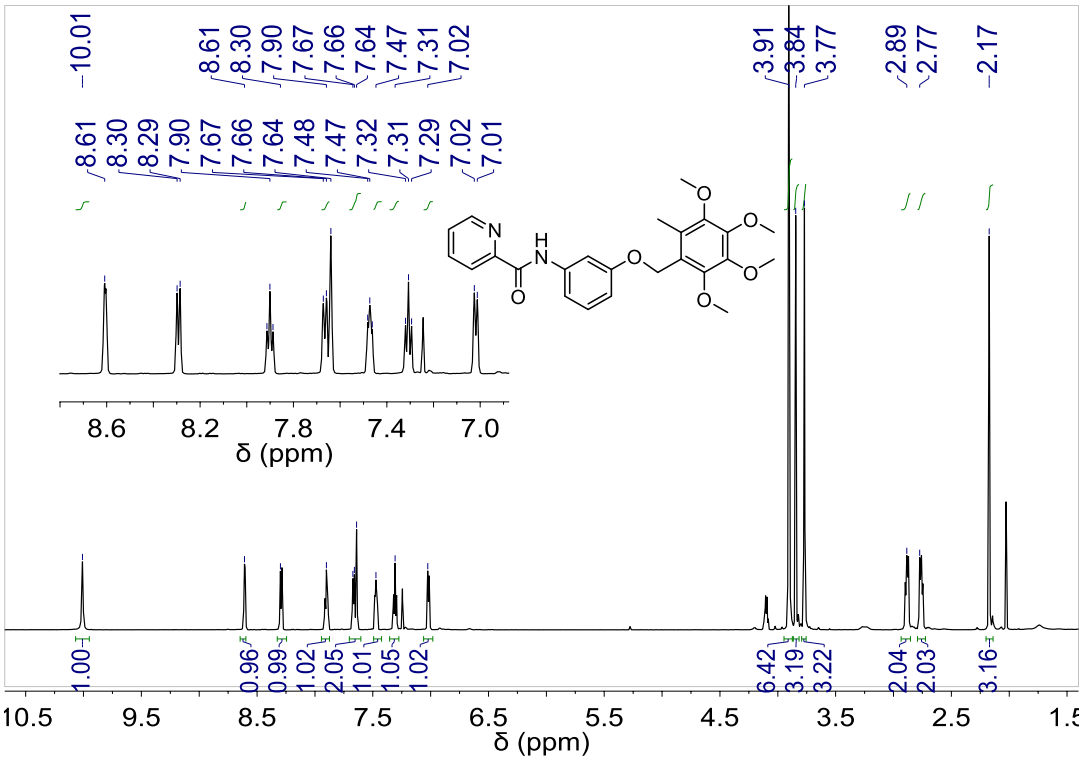

Figure 2.31 ^{1}H NMR spectrum ($CDCl_3$, 600 MHz) of compound **7**.

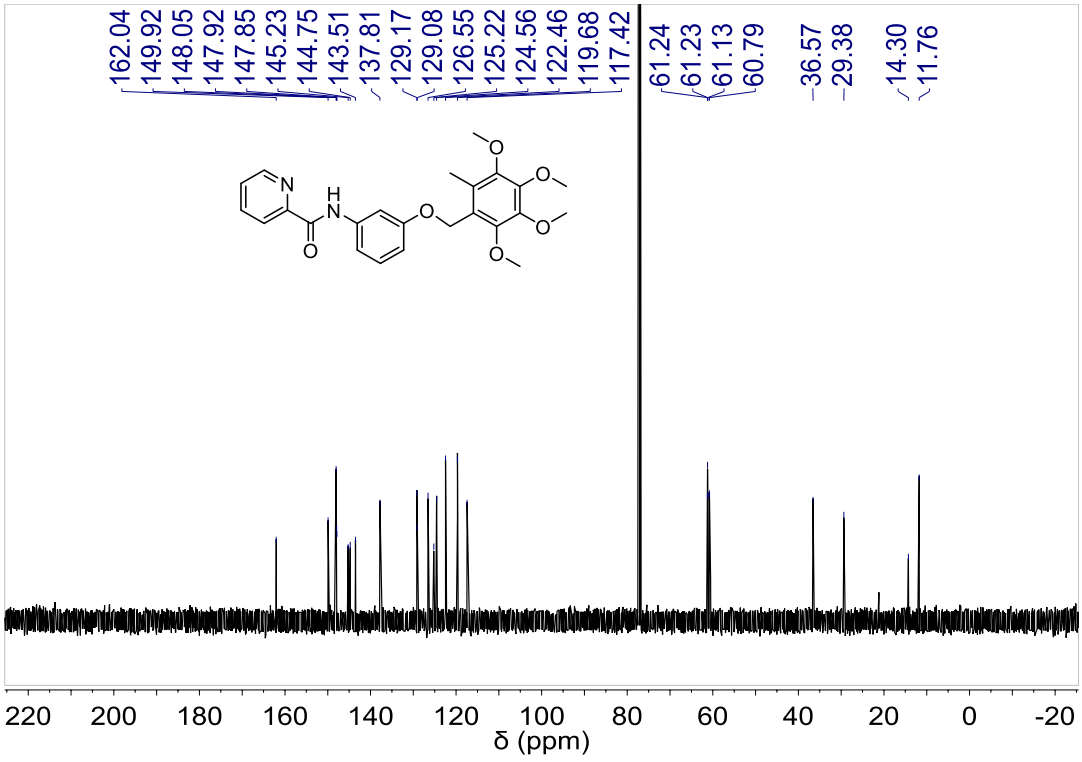

Figure 2.32 ^{13}C NMR spectrum ($CDCl_3$, 151 MHz) of compound **7**.

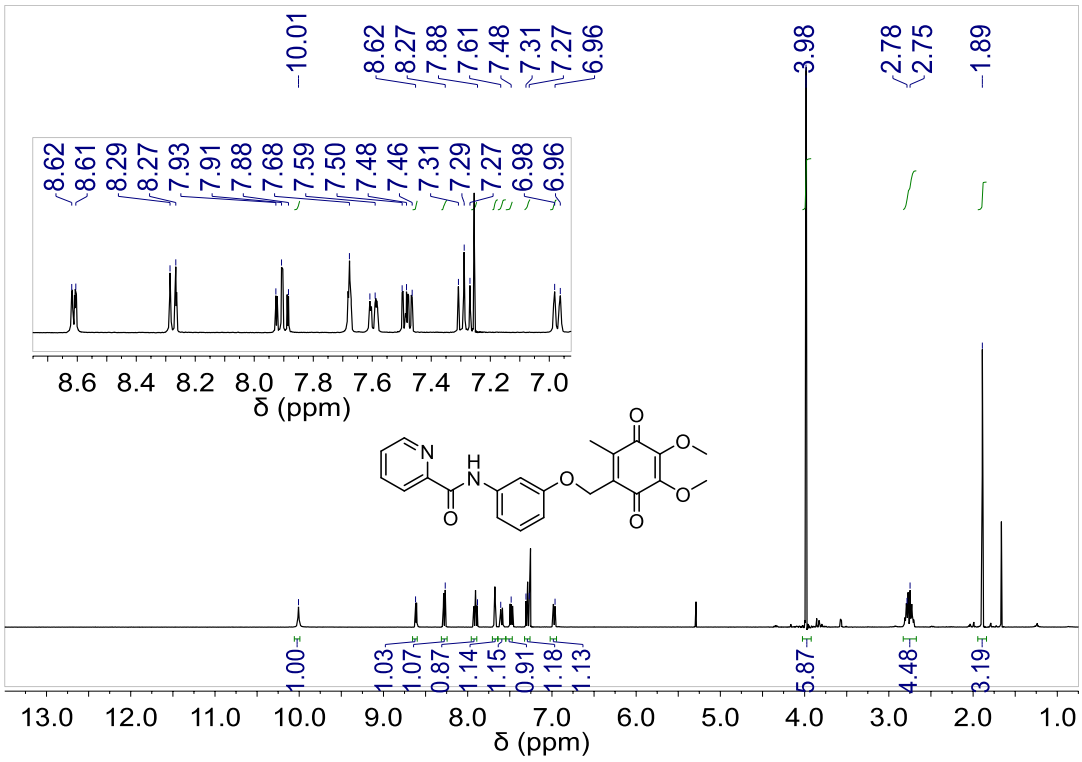

Figure 2.33 ^{1}H NMR spectrum ($CDCl_3$, 400 MHz) of compound **8**.

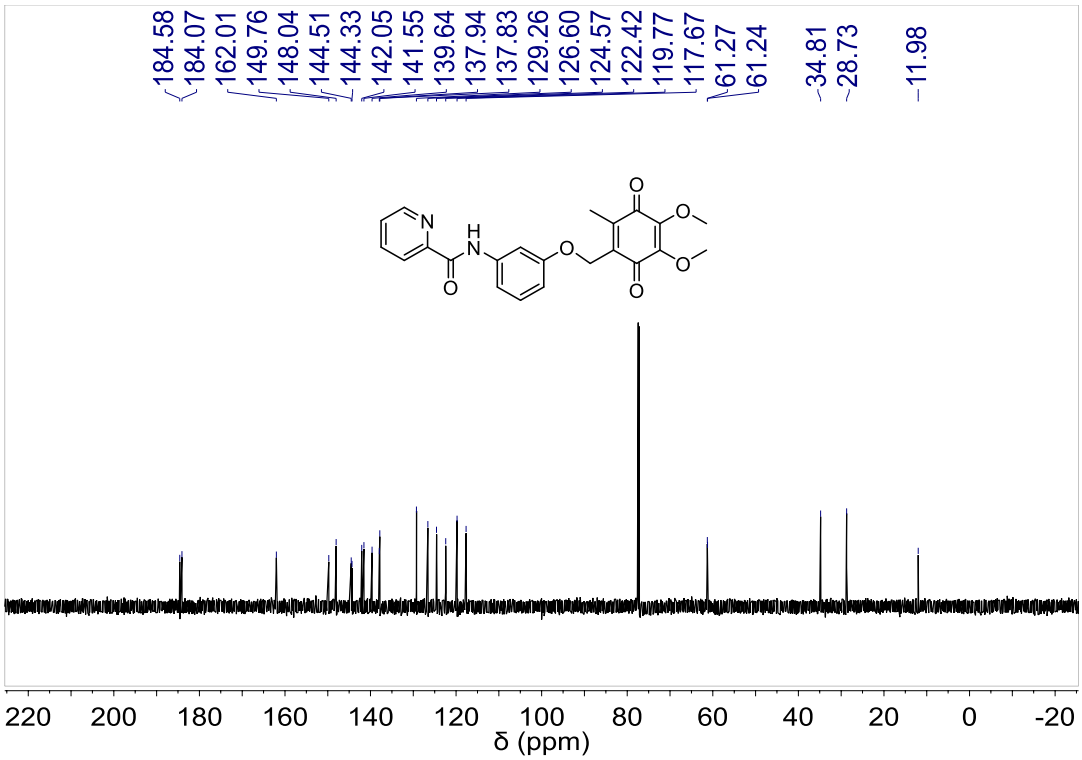

Figure 2.34 ^{13}C NMR spectrum ($CDCl_3$, 151 MHz) of compound **8**.

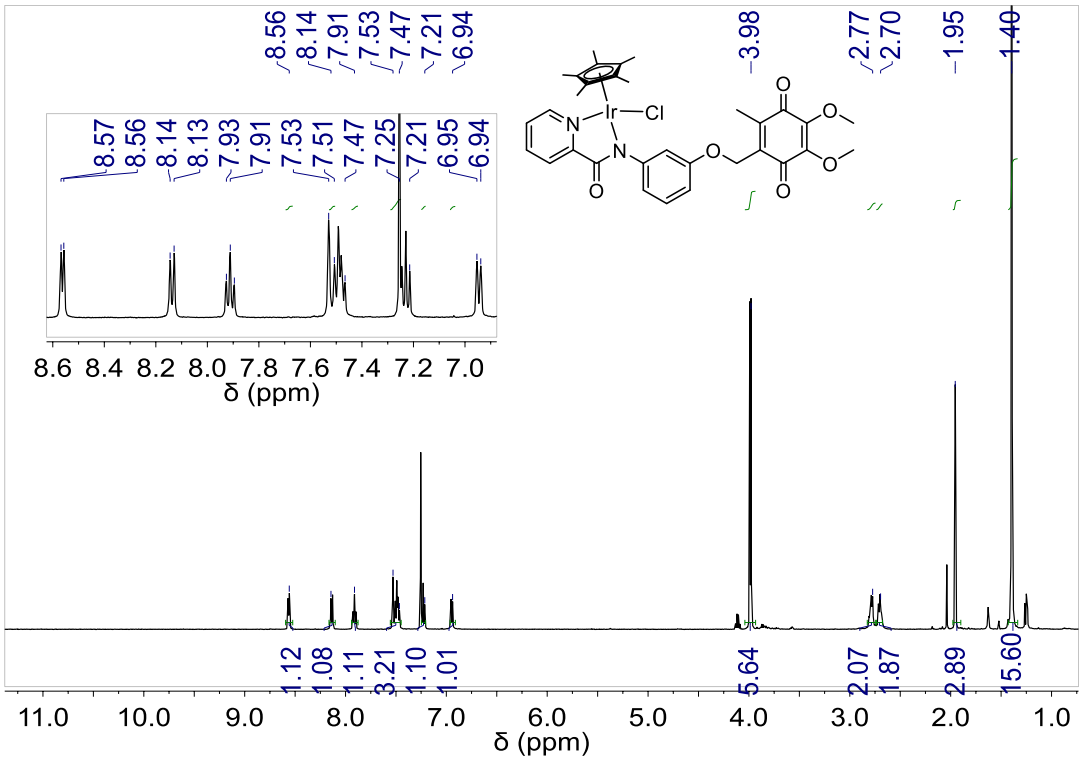

Figure 2.35 ^{1}H NMR spectrum ($CDCl_3$, 500 MHz) of compound **Ir3a**.

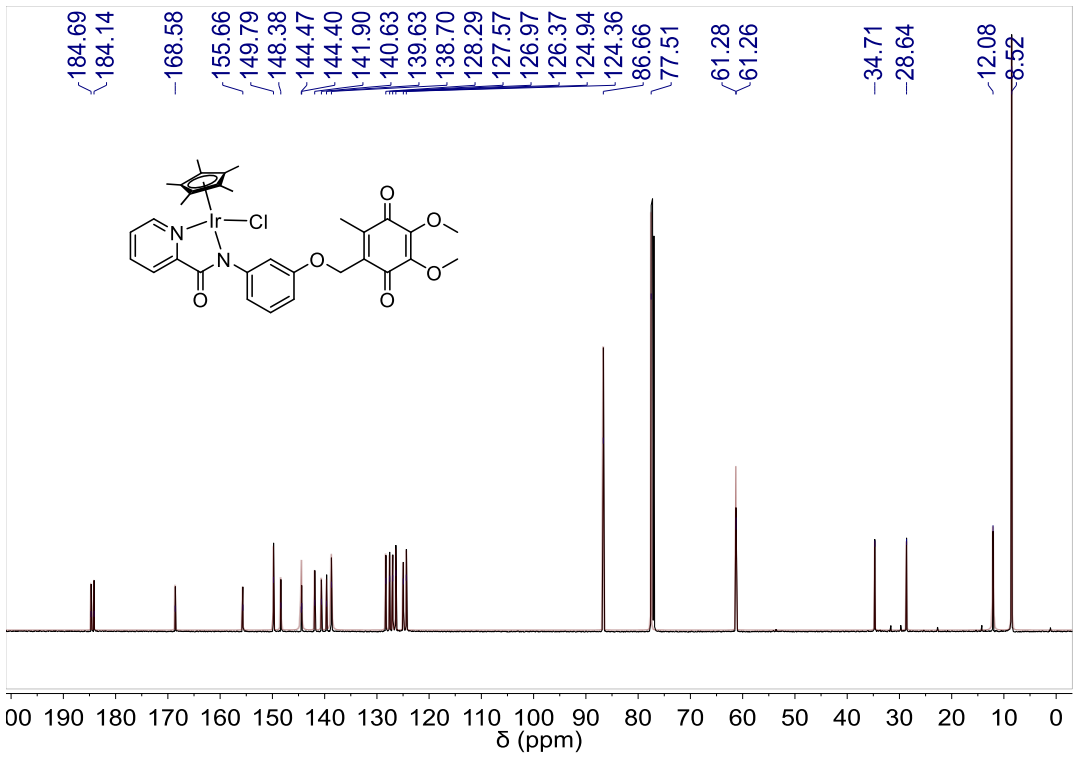

Figure 2.36 ^{13}C NMR spectrum ($CDCl_3$, 101 MHz) of compound **Ir3a**.

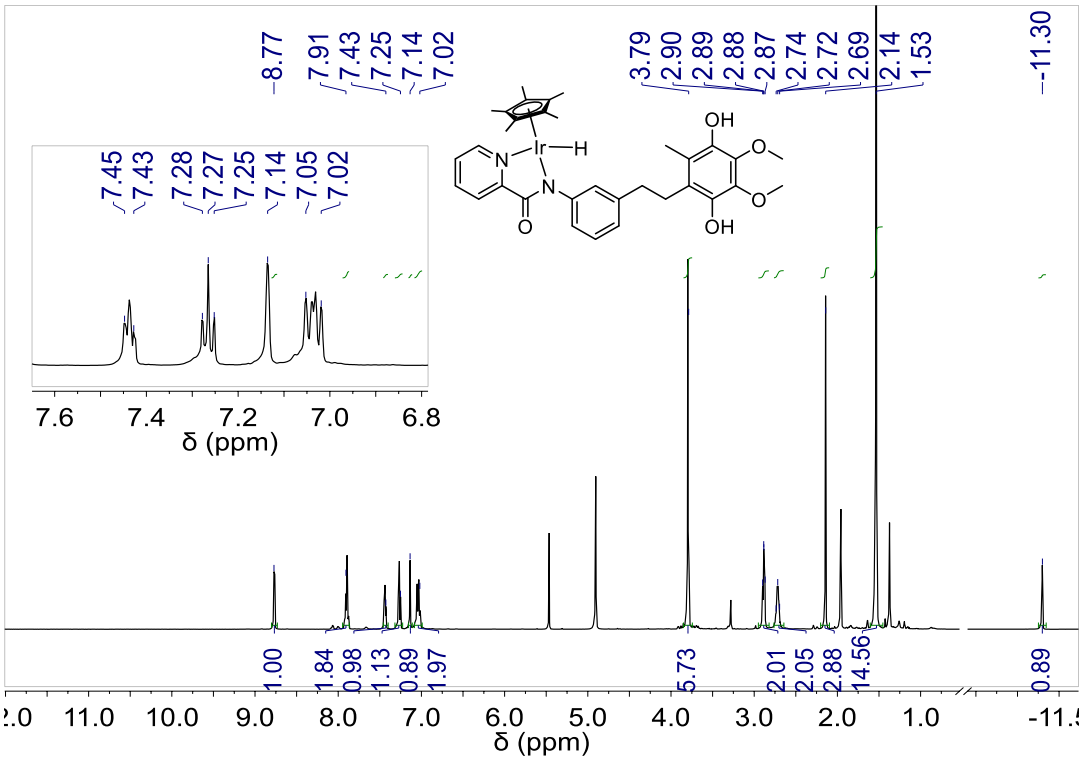

Figure 2.37 ^{1}H NMR spectrum (CD_3OD, 600 MHz) of compound **Ir3d**.

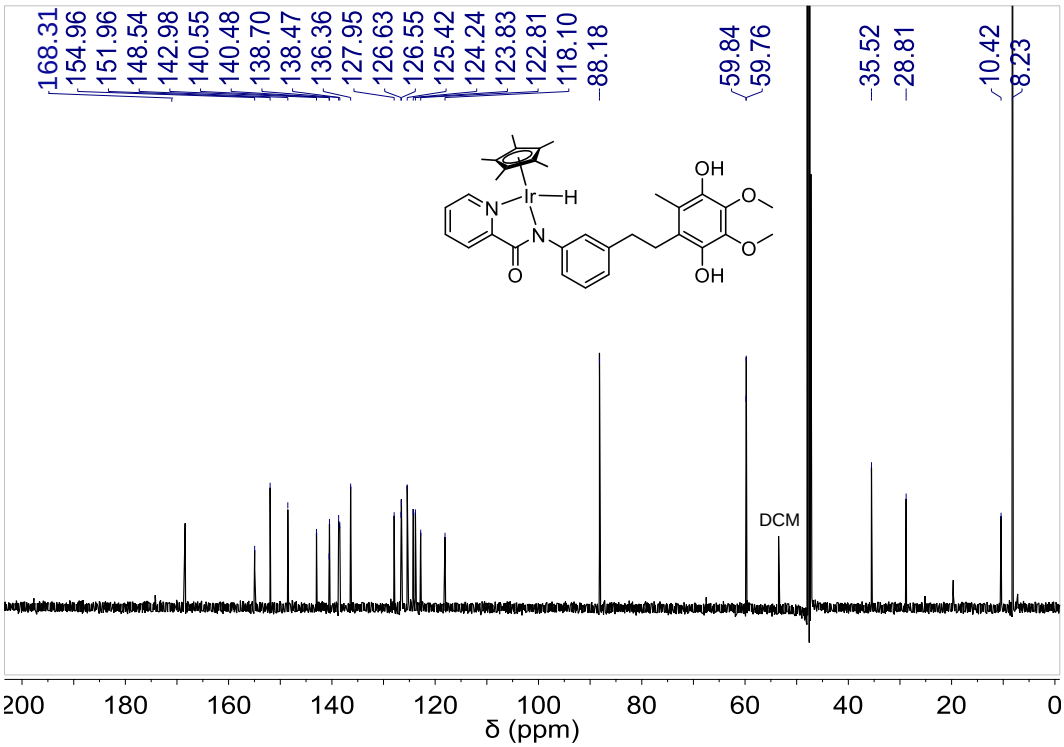

Figure 2.38 ^{13}C NMR spectrum (CD_3OD, 151 MHz) of compound **Ir3d**.

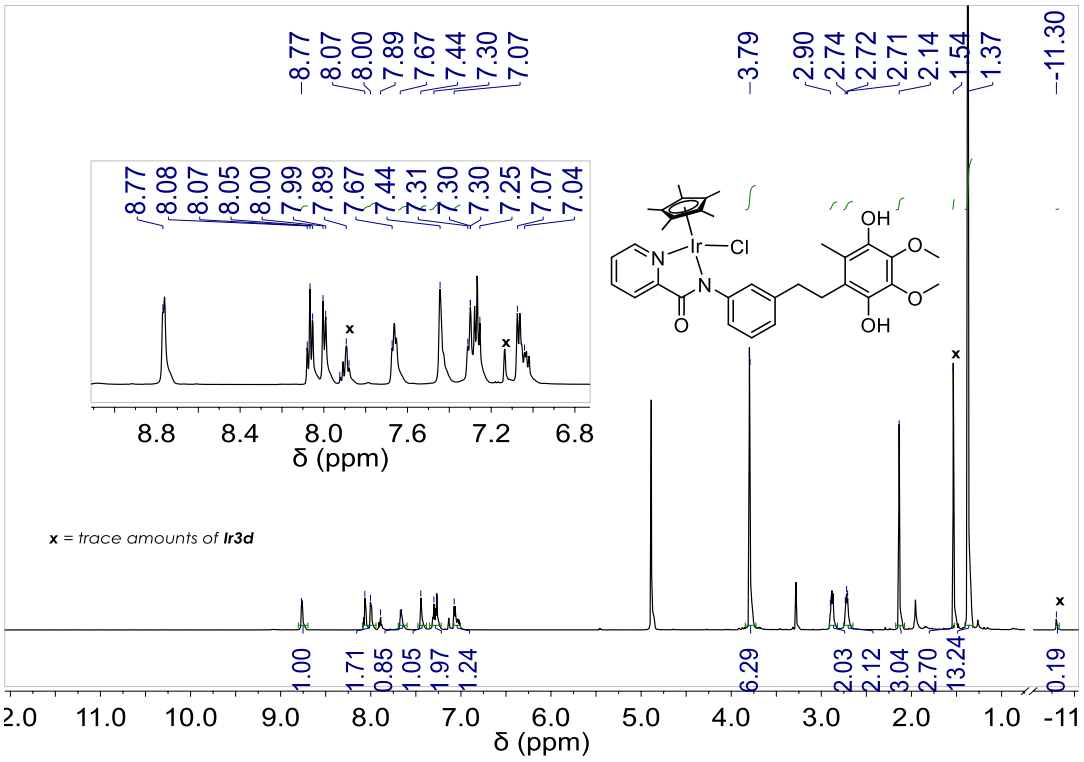

Figure 2.39 ^{1}H NMR spectrum (CD_3OD, 600 MHz) of compound **Ir3c**. Peaks corresponding to trace amounts of **Ir3d** present are marked with "x."

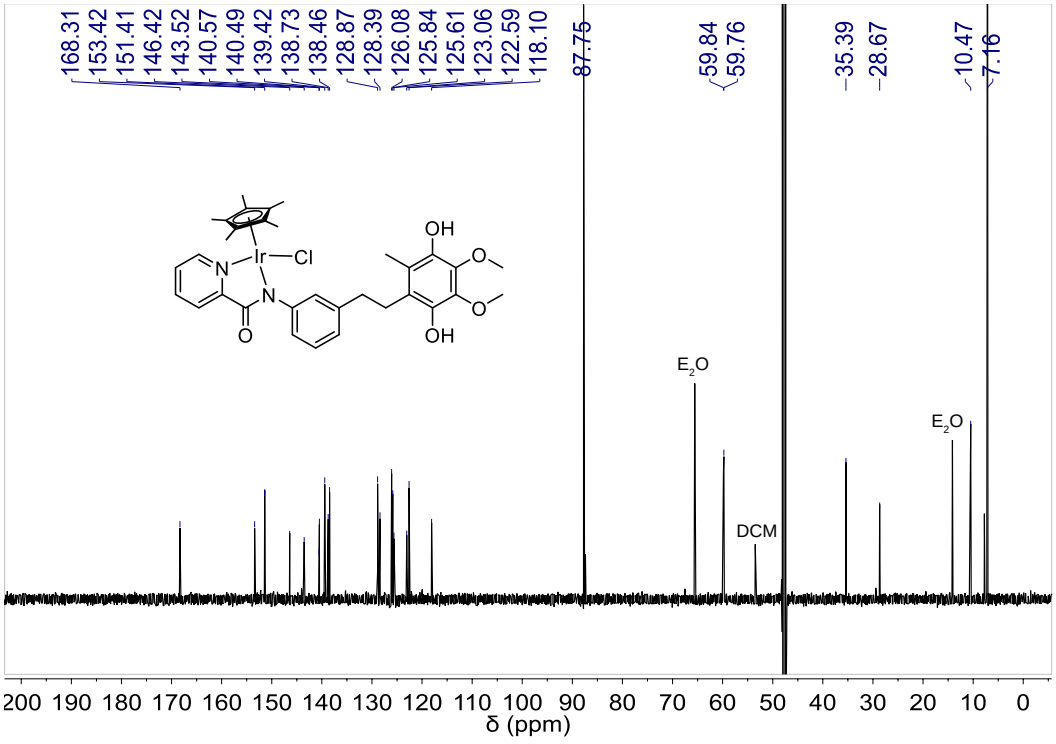

Figure 2.40 ^{13}C NMR spectrum (CD_3OD, 151 MHz) of compound **Ir3c**.

Chapter 3. Development of Metal-Based Liver X Receptor Agonists

3.1 Introduction

Liver X receptors (LXRs) are important members of the nuclear receptor family that regulate in many physiological processes such as cell differentiation, lipid metabolism, embryonic development, and metabolism.[120] Two isoforms of LXRs, LXRα and LXRβ, have been identified and have been found to be important for cholesterol, fatty acid, glucose metabolism as well as inflammatory responses. LXRα isoform is expressed in many major metabolic organs, and LXRβ is expressed ubiquitously. Upon binding of an agonist, such as natural oxysterols, LXR forms a heterodimer complex with other nuclear receptors, to active transcriptional function. The selective activation of LXRs has become an attractive approach for developing treatments for metabolic diseases. Several synthetic LXR agonists have been developed by pharmaceutical companies and were shown to have beneficial effects in the treatment of diabetes, Alzheimer's disease, and atherosclerosis.[121] **T0901317** was the first synthetic LXR ligand reported and it has become the most commonly used in research. However, due to its poor selectivity toward LXRβ over LXRα, it also activates the production of triglyceride and fatty liver.[122] In 2002, compound **GW3965** was demonstrated to be three times more selective for LXRβ over LXRα than **T0901317**. It first identified in a screen of synthetic nonsteroidal tertiary amine by GlaxoSmithKline (Brentford, UK).[122-125]

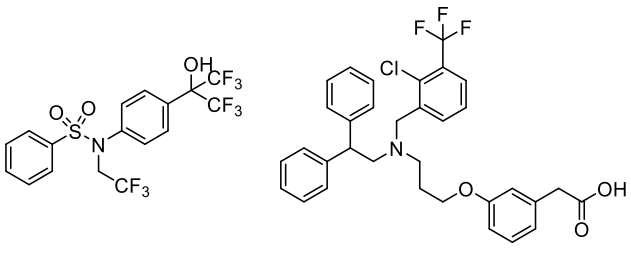

T0901317 GW3965

Figure 3.1 Synthetic LXR agonists.

Research suggests that LXRs are also involved in numerous types of cancer, which makes them potential targets for cancer therapeutics. In *in vitro* and *in vivo* breast cancer

models, LXRs can regulate hepatic estrogen expression, which serves an important role in estrogen-dependent cell growth and apoptosis.[126] It was shown that LXR agonists decrease the proliferation of cells in S-phase and induce G_1 arrest and apoptosis in MCF-7 cells.[127] In 2009, Steffensen and coworkers showed that the antiproliferative effect was independent of the lipogenic activity of **GW3965.** They proposed that the regulation of lipid production followed a different mechanism than that for the cell proliferation inhibition.

Although LXR has been intensively studied for its nuclear role in combating cholesterol/lipid related diseases, the non-nuclear signaling pathway has never been studied and remains unknown. Non-nuclear signaling pathway studies can be important in discovering new LXR target genes, as well as determining genomic and nongenomic mechanism. While LXR nuclear pathway requires agonist to enter the nucleus in order to active transcriptional activity, we propose a new synthetic GW3965 agonist that will prevent infiltrating into the nucleus, blocking LXR from direct nucleus activation.

In this project, we aim to prepare **GW3965** inorganic hybrids to increase the molecular weight of the LXR agonist. These complexes are proposed to retain the anti-proliferation properties of **GW3965** toward cancer cells while minimizing the activation of genes that lead to increases in plasma and fatty acid levels in the liver. Fluorogenic scaffolds were used in some designs in order to visualize the intracellular distribution of the synthetic complexes inside living cells.

3.2 Results and Discussion

3.2.1 Synthesis of Compound GW3965

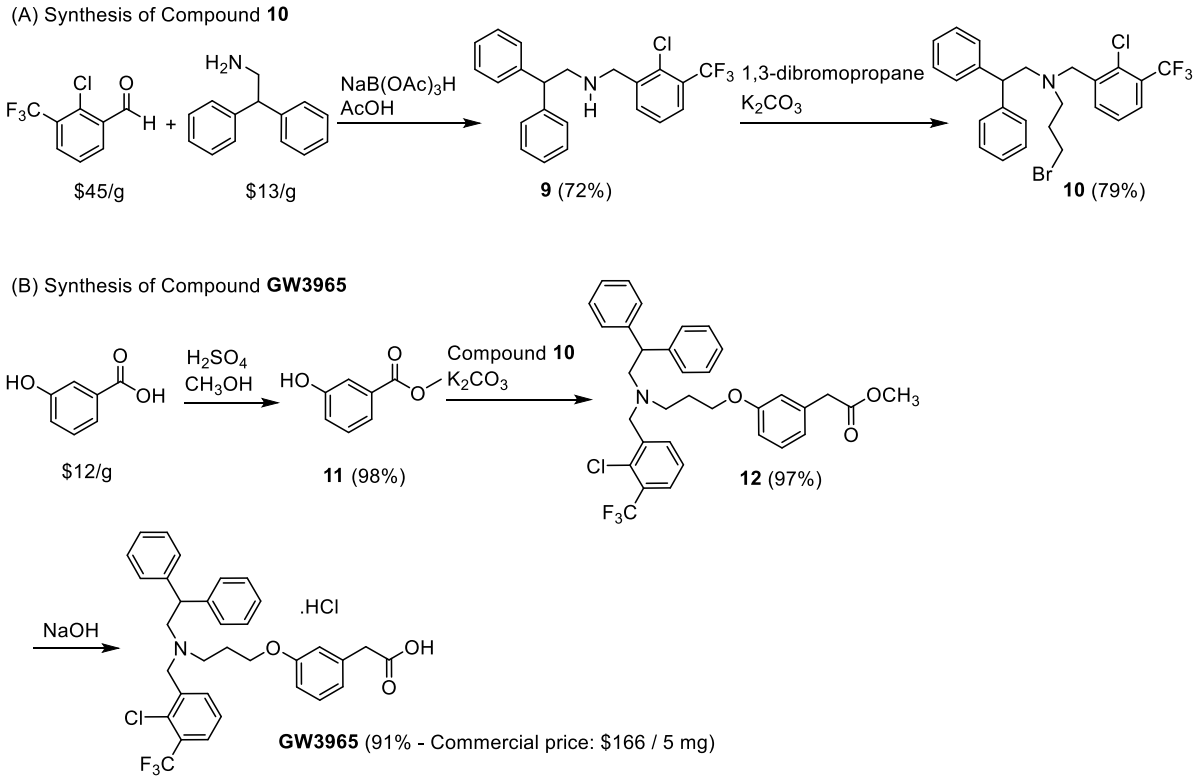

Scheme 3.1 Synthesis of compound **GW3965**.

Although GW3965 is commercially available, it is expensive ($166/5 mg). To obtain sufficient amounts of the compound for testing different metalation designs, we followed a 5-step procedure (Scheme 3.1).[128] We started with the reductive amination of affordable starting materials 2,2-diphenylethanamine ($13/g) and 2-chloro-3-(trifluoromethyl)benzaldehyde ($45/g) by using $NaB(OAc)_3H$ in DCM. This step resulted in the desired amine product in high yield (72%), which was utilized in the following nucleophilic substituent reaction with 1,3-dibromopropane. Compound **10** was then subjected to a Williamson ether synthesis with a protected hydroxyphenyl acetic acid. The final **GW3965** was obtained by ester hydrolysis of compound **12**. The neutral **GW3965** was a pale-yellow oil. However, for ease of handling and storage, it was converted into the ammonium salt by acidifying with HCl.

It is noteworthy that overall yield was 49%, which was significantly greater than the reported yields of 5% and 8%.[129-130] The final product was fully characterized by standard analytical techniques. A luciferase enzymatic activity assay data showed that our synthetic reagent had a similar biological activity as that obtained from a commercial source. Our method provides a more economical alternative for the production of **GW3965**, thereby increasing the practicality of *in vitro* biological testing of the compound.

3.2.2 Synthesis of Complex RhGW

With the synthesized **GW3965** in hand, we attempted to metalate it with rhodium to prepare dirhodium paddlewheel complexes. We surmised that having 4 **GW3965** units would enhance its biological activity as well as reduce its nuclear permeability.

A literature method was adapted for the synthesis of the paddlewheel complex. An excess amount of **GW3965** was combined with the precursor $Rh(OAc)_4$ in dry chlorobenzene and then heated at high temperature.[131] Once the reaction was complete, the solvent and acetic acid were removed by distillation, while the desired product remained in the reaction flask as a deep green solid. However, perhaps because of the steric bulk of **GW3965**, the reaction was inefficient. Our synthesis provided less than 10 mg of the **RuGW** complex, which was characterized by NMR spectroscopy.

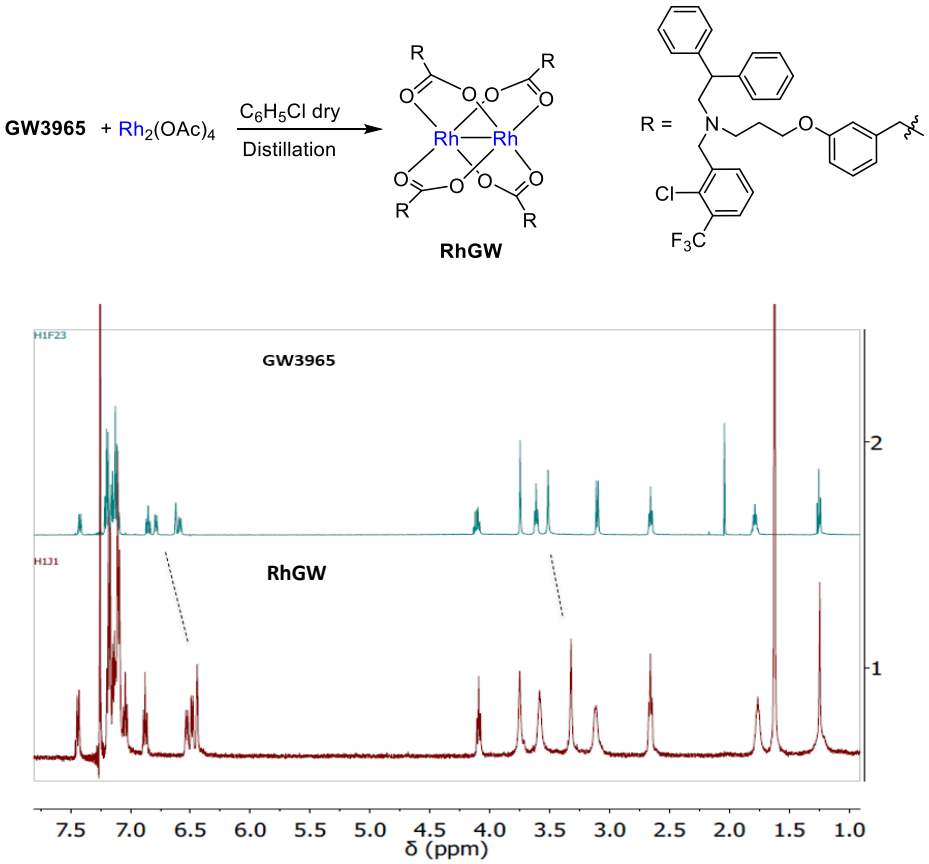

Figure 3.2 Synthesis and spectrum of compound **RhGW**.

The ^{1}H NMR and FTIR spectra of the $Rh_2(OAc)_4$/**RhGW** product suggest that the desired dirhodium complex had been formed (Fig. 3.2). However, attempts to scale up the synthesis led to observation of several byproducts, one of which may be the partially substituted rhodium complex. Purification of the crude material by column chromatography gave little to no improvement in purity. The rhodium complexes were found to change color from dark green to dark red color over the span of a week, which suggested it is chemically unstable under ambient conditions. We proposed that the large size of **GW3965** makes the complex become too bulky and thus, is susceptible to ligand dissociation.

3.2.3 Synthesis of Complex RuGW

Ruthenium complexes have been studied extensively as metallodrugs and shown promise as clinical candidates.[31] Inspired by these reports, we decided to attach **GW3965** to

6-coordinated Ru complexes. Since [Ru(II)(2,6-bis(pyrazol-1-yl)pyridine$_3$]$^{2+}$ is fluorescent emission, we proposed that it could be used as an emissive reporter in live cell imaging studies to visualize the intracellular localization of the Ru-**GW3965** hybrid.

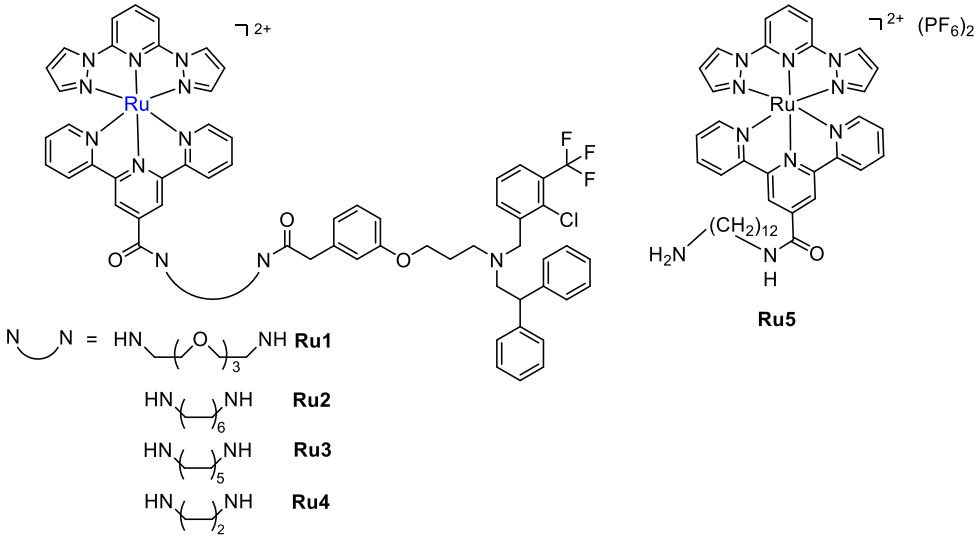

Figure 3.3 Designs of ruthenium – **GW3965** conjugates.

To enhance the solubility of the Ru complexes in water, we used a hydrophilic polyethylene glycol (PEG) chain as the bridge to connect **GW3965** and the ruthenium center via two amide bond formation reactions as indicated in Fig. 3.3 (**Ru1**). The terpyridine ligand was successfully connected to the PEG chain. However, attempts to generate an amide bond of this compound to **GW3965** did not give the desired product. Replacing the PEG chain with aliphatic linkers led to successful coupling. Complex **Ru5**, which has 12-carbon chain in its structure was also prepared. This was the precursor to synthesize the final complex **Ru2.** Unfortunately, after several attempts, we still could not obtain the final amide product. Shortening the aliphatic chain with 10-carbon and 4-carbon linkers (**Ru3**, **Ru4**) did not improve the synthetic efficiency. We hypothesized that the benzoic acid of **GW3965** was not reactive, which made it challenging to generate a new bond. Therefore, a derivative of the active molecule, which had the acid group replaced by an alcohol functional group, was prepared - **GW3965b.** Additionally, forming amide bonds is generally more difficult than

forming ether bonds. Our final **RuGW** design contained two ether linkers with small modifications on both the agonist moiety and the ruthenium ligand (Scheme 3.2).

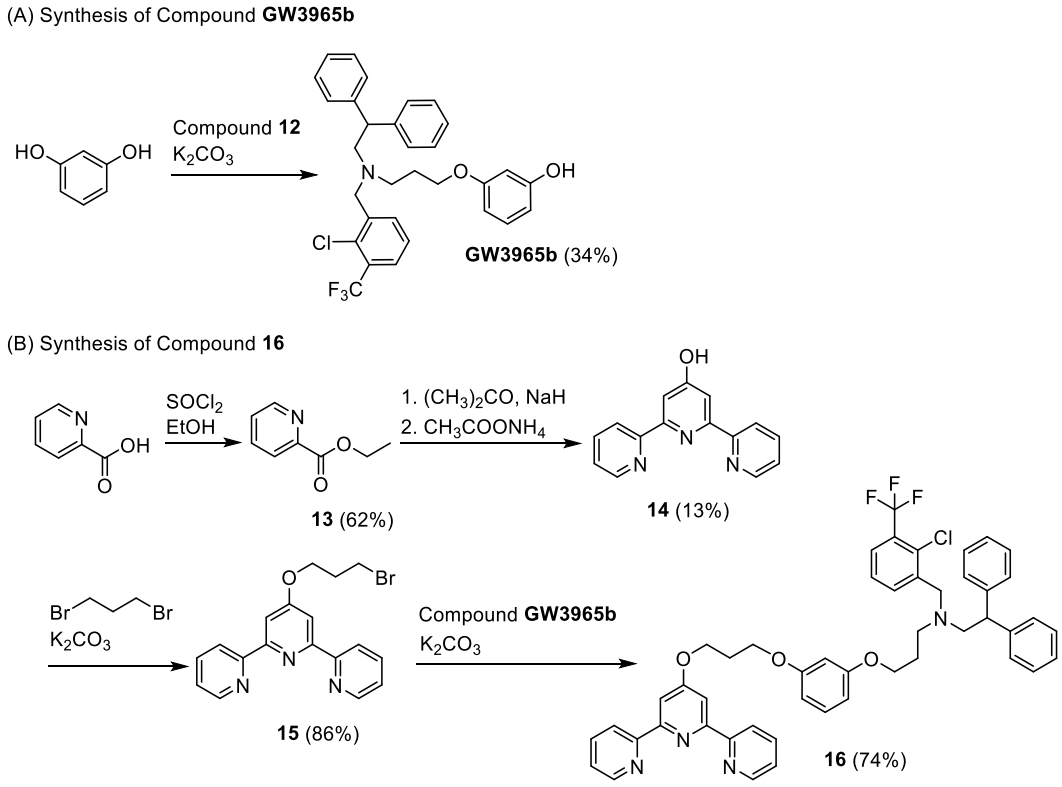

Scheme 3.2 Synthesis of compound **GW3965b** and ligand **16.**

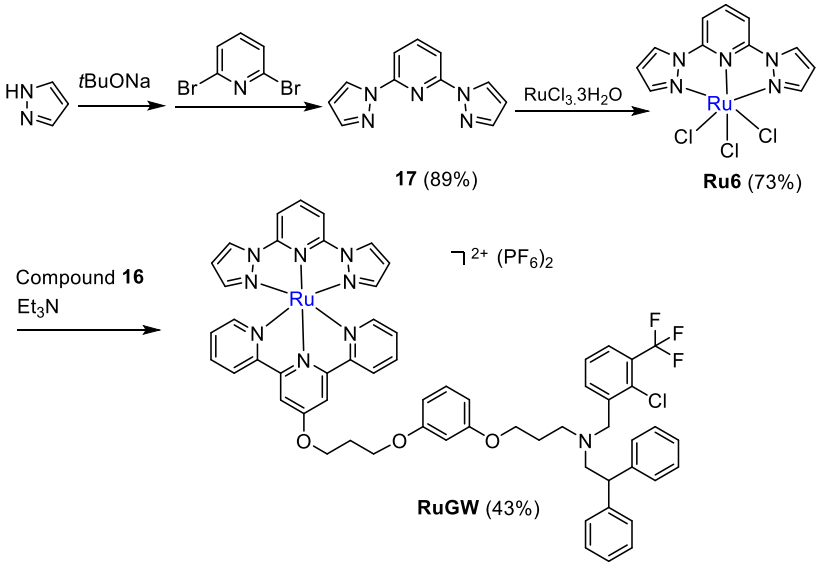

Scheme 3.3 Synthesis of complex **RuGW.**

In the first step, picolinic ethyl ester was reacted with dry acetone to form a triketone**,** followed by a condensation with ammonium acetate to generate the terpyridine derivative **14.**

Compound **14** and **GW3965b** were attached by reacting stepwise 1,3-dibromopropane to prepare ligand **15**. Except the ring closing step (22% yield for **13**), other reactions resulted in moderate to high isolated yields (60-85%). The pyrazolylpyridine ligand **17** and the precursor **Ru6** were prepared following the reported procedures in 89% and 73% yield, respectively. The final metalation step provided a pure product, and the desired composition was confirmed by NMR spectroscopy and HRMS analysis. Unfortunately, we could not observe any fluorescent signal when visualizing **RuGW** in cellular media using microscopy. We hypothesized that our ligand modification may affect the electronic properties of the metal complex and inhibit its fluorescence emission.

3.2.4 Synthesis of Complex IrGW

The complex $[Ir(III)(phenylpyridine)_2(bipyridine)]^+$ has been widely used in cell imaging studies due to its phosphorescent properties.[132-133] To take advantage of this feature, we attached **GW3965** to a phenylpyridine ligand so that it could be metalated with iridium (Scheme 3.4). Our design is attractive because it contains two units of **GW3965,** per Ir, which has high molecular weight, and is fluorescent.

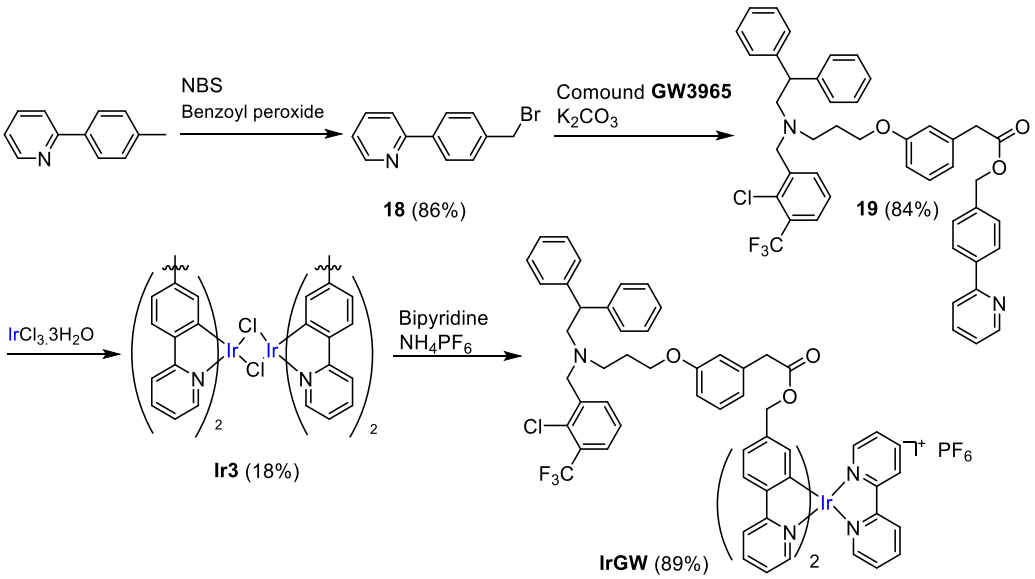

Scheme 3.4 Synthesis of complex **IrGW**

To synthesize the ligand, monobromination of methylphenyl pyridine was carried out using NBS and benzoyl peroxide. Reaction of **18** with **GW3965** to provide compound **19** in good yield. A common procedure to prepare iridium dimer complex was used to synthesize the precursor **Ir3**, which was followed by a ligation step with bipyridine to yield the final product (89%). The fluorescent **IrGW** show an emission with λ_{max} at 576 ± 5 nm upon excitation with 310 nm in DCM at room temperature (Fig. 3.3). The quantum yield of this complex was calculated to be 1.1%, relative to a standard of tetraphenylporphyrin in toluene, which has a reported fluorescence quantum field (Φ_F) of 11%.[134]

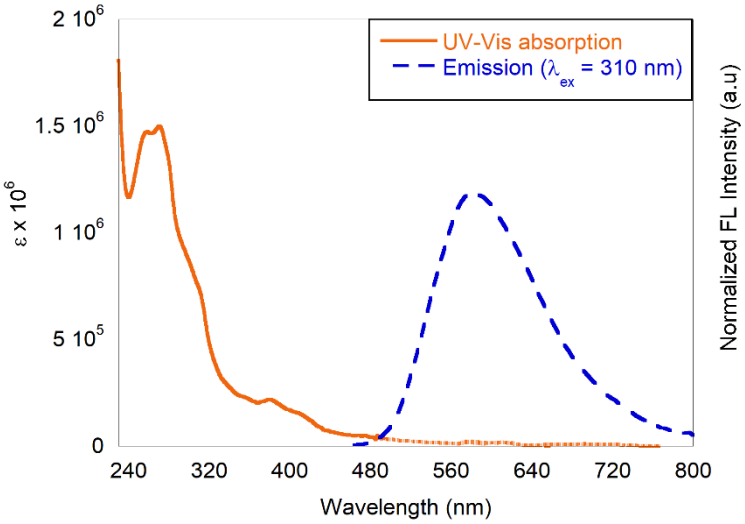

Figure 3.4 Photophysical spectra of **IrGW.**

Unfortunately, due to the low quantities of **IrGW** obtained, we are unable to measure its ^{13}C NMR spectrum at this time. synthesized molecules were characterized by ^{1}H NMR, 2D NMR and HRMS. We planned to carry out larger scale preparations for those complexes for further characterization and *in vitro* studies.

3.2.5 Spatial Distribution of Complex IrGW in Cells.

The nuclear permeability of the synthetic iridium conjugate was studied in A549 human lung cancer cells and MCF-7 human breast cancer cells. The cells were co-treated

with **IrGW** and commercially available nucleus and mitochondria dyes and imaged by fluorescent microscopy. In each experiment, the Pearson's Correlation Coefficient (PCC) was calculated based on the signal overlap between two different emission channels.

A549 cells were grown in an 8-well imaging slide and then exposed to **IrGW** (5 μM) and the nucleus stain Hoechst 33342 for 30 min. The cells were then washed with FluoroBrite DMEM before being visualized using an Olympus IX83 inverted microscope with a 100× TIRF oil immersion objective. As showed in Fig. 3.4, the iridium complex showed strong green fluorescence in the cytoplasm but not the nucleus. Cationic cyclometalated iridium complexes are known are known to localize in the nucleus, lysosome, mitochondria, and endoplasmic reticulum.[133, 135-136] In this experiment, a PCC value of 0.083 was obtained, which suggests that **IrGW** is nucleus impermeable.

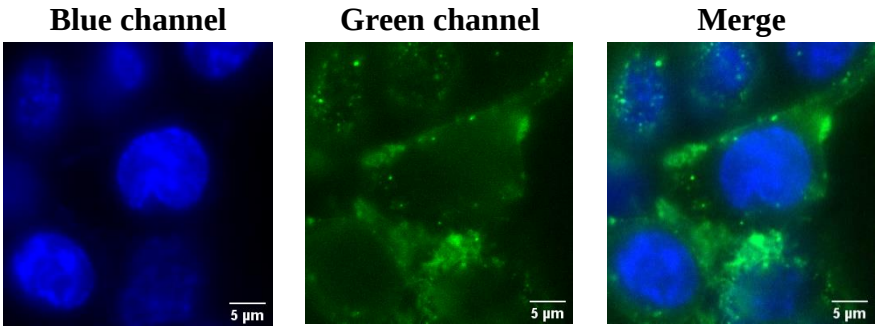

Figure 3.5 Colocalization images of **IrGW** with Hoechst 33342 in A549 human lung cancer cells. The excitation wavelength for Ir complexes is 488 nm (emission filter: 525 ± 25 nm). The excitation wavelength of Hoechst 33342 is 405 nm (emission filter: 438 ± 12 nm). Images were acquired using 100× oil objective in Olympus IX83 microscope

A similar experiment was performed using MCF-7 cells. In these experiments, cells were treated with **IrGW**, mitochondria tracker Mito-ID, and nucleus stain Hoechst 33342. The cells were washed, and the samples were visualized by confocal imaging with a 60× objective. The excitation for Mito-ID is 561 nm and the emission wavelength is 615 ±12 nm (Fig. 3.5). A PCC value of 0.087 was obtained for the colocalization of **IrGW** with the

nucleus stain, which was similar to that observed in the A549 cell studies. These results suggest that **IrGW** is not nucleus permeable in both single nuclear and multi nuclear cell lines. Interestingly, although **IrGW** was found in the cytoplasm, no signal was detected in the mitochondria (PCC value = 0.055). Different organelle stains will be used to determine the intracellular localization of **IrGW** in other organelles in future work.

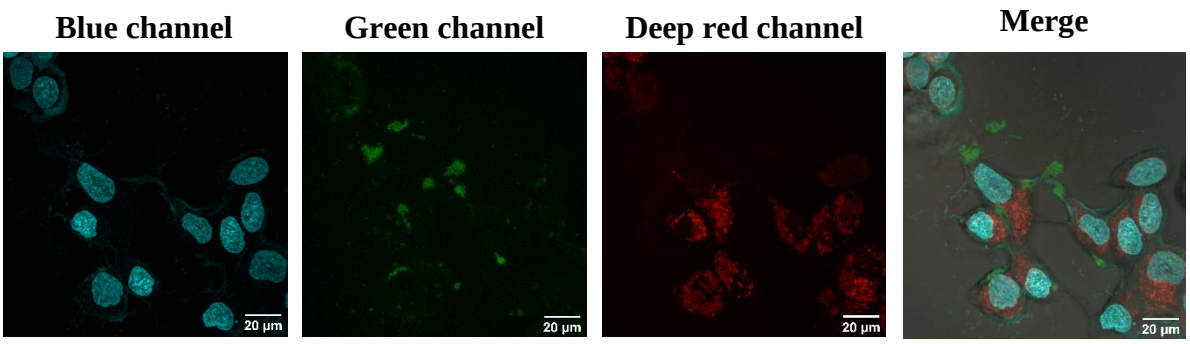

Figure 3.6 Colocalization images of **IrGW**, Hoechst 33342, and Mito-ID in MCF-7 breast cancer cells. The excitation wavelength for Ir complexes is 488 nm (emission filter: 525 ± 25 nm), for Mito-ID is 561 nm (emission filter: 615 ±12 nm), and for Hoechst 33342 is 405 nm (emission filter: 438 ± 12 nm). Images were acquired using 60× objective in Olympus IX83 microscope

When MCF-7 cells were co-treated with the β Liver X Receptor antibody labeled with Alexa 594 probe and **IrGW**, a PCC value of 0.731 was obtained. These data showed good correlation between Alexa 594 and the Ir complex, which suggest that **IrGW** is selective toward LXRβ. We are currently analyzing fractional cell lysates by ICP-MS to study the cellular distribution and accumulation of **IrGW** and **RuGW.** Both complexes are currently being tested by Dr. Umetani's group for their biological activity using proliferation assays, qPCR and SPR analysis.

3.3 Conclusion

In this project, we designed and synthesized several conjugates between a synthetic liver X receptor agonist (**GW3965**) and different metal complexes. The synthetic procedures were optimized to obtain high reactions yield with minimal purification effort. The new ruthenium/rhodium/iridium complexes are exhibit poor nuclear permeability and selectively inhibit nuclear gene expression, which may have further applications in the treatment of breast cancer. The fluorescent cyclometalated **IrGW** complex appears to target LXRβ selectivity. We are performing qPCR, cell proliferation, and cytotoxicity assays to further investigate these complexes' behaviors inside cells.

3.4 Experimental Section

3.4.1 General Procedures

Commercial reagents were used as received without further purification. All air- and water-sensitive manipulations were performed using standard Schlenk techniques or under a nitrogen atmosphere inside a glovebox. Anhydrous solvents were obtained from an Innovative Technology solvent drying system saturated with Argon. Ligand **13**, **18** and complex **Ru1, Ir3** were synthesized according to literature procedures. A549 human lung cancer cells and MCF-7 human breast cancer cells were obtained from ATCC.

Physical Methods: NMR spectra were acquired using JEOL spectrometers (ECA-400, 500, and 600) at room temperature and referenced using residual solvent peaks. All ^{13}C NMR spectra were proton-decoupled. Ultraviolet-visible (UV) absorption spectroscopic studies were performed using an Agilent Cary 60 spectrophotometer. Steady-state emission spectra were recorded using a Horiba FluoroMax-4 spectrofluorometer with appropriate long-pass filters to exclude stray excitation light from detection. Solution quantum yields were

determined relative to a standard of tetraphenylporphyrin in toluene, which has a reported fluorescence quantum yield (Φ_F) of 11%.

3.4.2 Synthesis and Characterization

Preparation of Compound 9. To a stirred mixture of 2,2-Diphenylethanamine (1.0 g, 5.0 mmol, 1.0 equiv.) and 2-chloro-3-(trifluoromethyl)benzaldehyde (1.15 g, 5.5 mmol, 1.1 equiv.) in dry DCM, 1 drop of acetic acid was added and the mixture was stirred at room temperature for 1 h. Sodium triacetoxyborohydride (2.1 g, 10.0 mmol, 2 equiv.) was then added. The reaction was stirred at room temperature overnight and was monitored by thin layer chromatography. After the reaction was complete, the reaction mixture was washed with saturated $NaHCO_3$ solution. The organic layer was collected and dried over Na_2SO_4. The product was purified by column chromatography (1 Ethyl acetate : 3 Hexane) and was isolated in 72% yield. ^{1}H NMR ($CDCl_3$, 500 MHz) δ (ppm) = 7.66 (d, J_{HH} = 8 Hz, 1H), 7.61 (d, J_{HH} = 7.2 Hz, 1H), 7.41–7.28 (m, 11H), 4.35 (t, J_{HH} = 7.6 Hz, 1H), 4.04 (s, 2H), 3.36 (d, J_{HH} = 7.6 Hz, 2H). ^{13}C NMR ($CDCl_3$, 125.7 MHz): δ (ppm) = 142.87, 140.32, 133.34, 131.75, 128.91, 128.23, 126.89, 126.66, 126.45, 126.40, 126.36, 126.32, 54.09, 51.50, 51.22. GC-MS: calc. for $C_{22}H_{19}ClF_3N$ $[M]^+$ = 389.1, found 389.0

Preparation of Compound 10. Compound **9** (1.3 g, 2.96 mmol, 1.0 equiv.) and 1,3-dibromopropane (1.7 mL, 16.6 mmol, 5.0 equiv.) were added to a round bottom flask along with K_2CO_3 (2.0 g, 9.4 mmol, 3.0 equiv.) and CH_3CN (40 mL). The reaction mixture was then refluxed overnight under a N_2 flow. The product was washed with saturated ammonium chloride solution, dried over $NaSO_4$ and concentrated. Column chromatography was performed (1

Ethyl acetate: 4 Hexane) to obtain the product as a yellow oil (79% yield). ^{1}H NMR ($CDCl_3$, 500 MHz) δ (ppm) = 7.55 (d, J_{HH} = 7.5 Hz, 1H), 7.41–7.28 (m, 11H), 4.15 (t, J_{HH} = 7.7 Hz, 1H), 3.76 (s, 2H), 3.21 (t, J_{HH} = 6.3 Hz, 2H), 3.12 (d, J_{HH} = 7.7 Hz, 2H), 2.69 (t, J_{HH} = 6.4 Hz, 2H), 1.95 – 1.89 (m, 2H). ^{13}C NMR ($CDCl_3$, 125.7 MHz): δ (ppm) = 141.87, 138.39, 132.50, 130.13, 126.99, 126.74, 125.00, 124.82, 124.65, 124.61, 124.56, 124.36, 59.09, 54.83, 51.28, 48.35, 30.54, 29.00. GC-MS: calc. for $C_{24}H_{25}BrClF_3N$ $[M]^+$ = 509.1, found 509.0

Preparation of Compound 11. Concentrated sulfuric acid (0.5 mL) was added to a solution

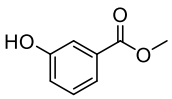

of 3-hydroxyphenylacetic acid (7.72 mmol, 1.2 g) in methanol. The reaction was refluxed for 4 h and monitored by thin layer chromatography. To work up the reaction, methanol was removed under vacuum and the crude product was dissolved in ethyl acetate. This organic layer was washed with water, saturated $NaHCO_3$ solution, and brine before being concentrated. The product was obtained as a clear oil (98% yield). ^{1}H NMR ($CDCl_3$, 500 MHz) δ (ppm) = 7.16 (t, J_{HH} = 7.8 Hz, 1H), 6.80 (d, J_{HH} = 7.5 Hz, 1H), 6.76 (s, 1H), 6.73 (d, J_{HH} = 8.1 Hz, 1H), 3.70 (s, 3H), and 3.58 (s, 2H). ^{13}C NMR ($CDCl_3$, 125.7 MHz): δ (ppm) = 173.26, 156.20, 135.23, 129.95, 121.50, 116.43, 114.54, 52.54, 41.20. GC-MS: calc. for $C_8H_8O_3$ $[M]^+$ = 152.1, found 152.2

Preparation of Compound 12. Compound **10** (450 mg, 0.88 mmol, 1.0 equiv.) and

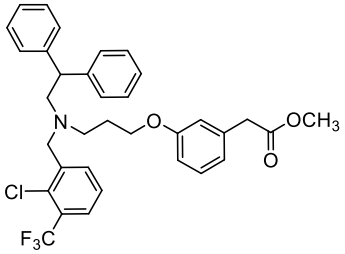

compound **11** (175 mg, 1.05 mmol, 1.2 equiv.) were dissolved in 30 mL of CH_3CN, then K_2CO_3 (182 mg, 1.3 mmol, 1.5 equiv.) was added. The reaction mixture was heated to refluxed overnight. After the reaction was complete, the white solid was removed by filtration. The organic layer was concentrated, and the crude product was

purified by column chromatography (1 Ethyl acetate: 3 Hexane) to obtain the pure product in 97% yield. ^{1}H NMR ($CDCl_3$, 400 MHz) δ (ppm) = 7.50 (d, J_{HH} = 7.6 Hz, 1H), 7.36 – 7.12 (m, 7H), 6.91 (t, J_{HH} = 6.9 Hz, 2H), 6.76 – 6.62 (m, 2H), 4.18 (t, J_{HH} = 7.5 Hz, 1H), 3.83 (s, 2H), 3.72 – 3.69 (m, 5H), 3.64 (s, 2H), 3.18 (d, J_{HH} = 7.6 Hz, 2H), 2.74 (t, J = 6.1 Hz, 3H), 1.88 (t, J_{HH} = 7.6 Hz, 2H). ^{13}C NMR ($CDCl_3$, 100.6 MHz): δ (ppm) = 170.36, 157.40, 141.85, 138.08, 133.68, 132.23, 129.65, 127.90, 126.78, 126.65, 124.76, 124.59, 124.19, 124.14, 119.82, 113.80, 111.44, 63.21, 58.66, 54.42, 50.48, 49.10, 48.12, 39.64, 25.21.

Preparation of Compound GW3965. Compound **12** (490 mg, 0.85 mmol, 1.0 equiv.) and sodium hydroxide (136 mg, 3.4 mmol, 4.0 equiv.) were dissolved in 9 mL of THF/MeOH/H_2O (3:1:5). The reaction mixture was refluxed for 4 h. After completion, the mixture was cooled to room temperature and was acidified by adding diluted HCl solution to obtain a pH 5 solution. The organic compound was extracted into ethyl acetate, and then washed with water and brine. The solvent was removed under vacuum to obtain the pure product as a pale-yellow oil (91% yield). The ammonium salt of this product was collected by the addition of HCl/Et_2O into a solution of the pure product in diethyl ether. ^{1}H NMR ($CDCl_3$, 400 MHz) δ (ppm) = 7.44 (d, J_{HH} = 7.6 Hz, 1H), 7.27 – 7.10 (m, 11H), 6.86 (t, J_{HH} = 7.2 Hz, 2H), 6.64 (d, J_{HH} = 9.8 Hz, 2H), 4.13 (t, J_{HH} = 7.3 Hz, 2H), 3.78 (s, 2H), 3.64 (t, J_{HH} = 5.7 Hz, 2H), 3.61 (s, 2H), 3.14 (d, J_{HH} = 7.6 Hz, 2H), 2.69 (t, J_{HH} = 6.2 Hz, 2H), 2.04 (s, 2H), 1.87 – 1.79 (m, 2H), 1.26 (t, J_{HH} = 7.1 Hz, 2H). ^{13}C NMR ($CDCl_3$, 100.6 MHz): δ (ppm) = 159.10, 143.51, 139.76, 135.11, 133.89, 131.35, 129.59, 128.47, 128.33, 126.45, 126.25, 125.88, 125.84, 121.58, 115.63, 113.21, 65.02, 60.35, 56.10, 50.86, 49.82, 26.89, 1.14. ESI-MS(+) calc. for $C_{33}H_{31}ClF_3NO_3$ $[M+H]^+$ = 582.1, found 582.5.

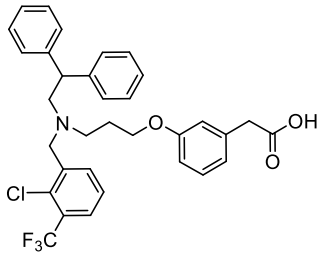

Preparation of Compound GW3965b. Compound **10** (102 mg, 0.2 mmol, 1.0 equiv.) and

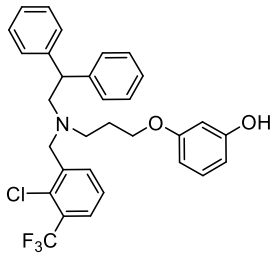

resorcinol (110 mg, 1.0 mmol, 5.0 equiv.) were dissolved in 30 mL CH_3CN, then K_2CO_3 (83 mg, 0.6 mmol, 3.0 equiv.) was added. The reaction mixture was heated to refluxed overnight. After the reaction was complete, the white solid was removed by filtration. The organic part was concentrated, and the crude product was purified by column chromatography (1 Ethyl acetate: 3 Hexane) to obtain the pure product with 34% yield. ^{1}H NMR ($CDCl_3$, 500 MHz) δ (ppm) = 7.48 (d, J_{HH} = 7.7 Hz, 1H), 7.27 – 7.08 (m, 11H), 6.93 (t, J_{HH} = 7.8 Hz, 1H), 6.43 (dd, J_{HH} = 8.0, 2.4 Hz, 1H), 6.34 (dd, J_{HH} = 8.3, 2.4 Hz, 1H), 6.28 – 6.25 (m, 1H), 4.15 (t, J_{HH} = 7.1 Hz, 1H), 3.79 (s, 2H), 3.68 (t, J_{HH} = 6.0 Hz, 2H), 3.14 (d, J_{HH} = 7.6 Hz, 2H), 2.71 (t, J_{HH} = 6.6 Hz, 2H), 1.84 (p, J_{HH} = 6.3 Hz, 2H).

Preparation of Compound 14. A mixture of anhydrous acetone (372 μL, 5 mmol, 1.0

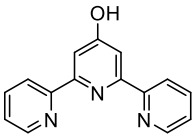

equiv.) and compound **13** (2.3 g, 15 mmol, 3.0 equiv.) in 10 mL of dry THF was added dropwise into a solution of NaH 60% (1.0 g, 25 mmol, 5.0 equiv.) in 10 mL of dry THF over 40 min. The reaction was refluxed under an inert atmosphere for 6 h. The solvent was gently removed under vacuum to collect a dark brown solid. This residue was washed with deionized water 3×. The aqueous phase was filtered through a celite pad to collect a yellow solution. The filtrate was then acidified by adding HCl until the solution became pH 6, a yellow precipitation appeared and was collected by filtration. This product was then dissolved in ethanol and combined with ammonium acetate (1.6 g, 21 mmol, 4 equiv.). The mixture was refluxed for 6 h. When the reaction was complete, the solvent was removed and then the residue was redissolved in DCM. The organic phase was washed with water and brine before being concentrated under vacuum. The pure product was collected as a pink solid (13% yield). ^{1}H NMR ($CDCl_3$, 400 MHz) δ

(ppm) = 8.77 (d, J_{HH} = 4.6 Hz, 2H), 7.93 (d, J_{HH} = 8.0 Hz, 2H), 7.87 (t, J_{HH} = 7.7 Hz, 2H), 7.42 (dd, J_{HH} = 7.5, 4.9 Hz, 2H), 7.11 (s, 2H). ^{13}C NMR ($CDCl_3$, 125.7 MHz): δ (ppm) = 149.57, 137.73, 125.20, 120.52, 113.67.

Preparation of Compound 15. A compound **14** (25 mg, 0.1 mmol, 1.0 equiv.), K_2CO_3 (28

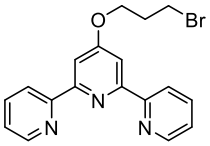

mg, 0.2 mmol, 2.0 equiv.), and 1,3-dibromopropane (32 μL, 0.3 mmol, 3.0 equiv.) were dissolved in 20 mL of sCH_3CN. The mixture was refluxed overnight. The solution turned purple after 3 h. When the reaction was complete, the white precipitate was removed by filtration and the filtrate was concentrated. The resulting oily residue was dissolved in ethyl acetate and washed with water and brine. The organic layer was separated and then evaporated to dryness. The crude product was dried under vacuum overnight at 60 ℃ to remove excess 1,3-dibromopropane. The final product was collected as a yellow solid (86% yield). ^{1}H NMR ($CDCl_3$, 500 MHz) δ (ppm) = 8.69 (s, 2H), 8.62 (d, J_{HH} = 7.4 Hz, 2H), 8.03 (s, 2H), 7.85 (t, J_{HH} = 6.8 Hz, 2H), 7.37 – 7.30 (m, 2H), 4.39 (s, 2H), 3.64 (t, J_{HH} = 5.2 Hz, 2H), 2.44 – 2.35 (m, 2H).

Preparation of Compound 16. A mixture of compound **15** (135 mg, 0.365 mmol, 1.0

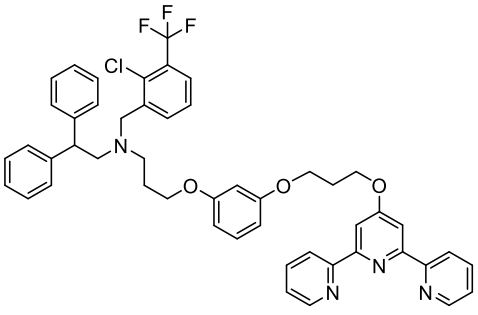

equiv.), **GW3965b** (217 mg, 0.4 mmol, 1.1 equiv.), and K_2CO_3 (151 mg, 1.1 mmol, 3.0 equiv.) were refluxed in 20 mL of CH_3CN overnight. When the reaction was complete, the white precipitate was removed by filtration and the filtrate was concentrated. The residue was dissolved in ethyl acetate and washed with water and brine. The organic layer was separated, evaporated to dryness, and purified by silica gel column chromatography using DCM/MeOH/Et_3N (100:2:0.5) eluent. The final product was collected

as a cloudy oil (74% yield). ^{1}H NMR (CD_3CN, 500 MHz) δ (ppm) = 8.64 (s, 2H), 8.60 (d, J_{HH} = 7.8 Hz, 2H), 8.03 (s, 2H), 7.89 (t, J_{HH} = 7.3 Hz, 2H), 7.48 – 7.44 (m, 1H), 7.41 – 7.35 (m, 2H), 7.23 – 7.08 (m, 11H), 6.94 (t, J_{HH} = 7.7 Hz, 1H), 6.51 (d, J_{HH} = 8.3 Hz, 1H), 6.28 (s, 2H), 4.45 – 4.38 (m, 2H), 4.22 – 4.10 (m, 3H), 3.74 (s, 2H), 3.61 (s, 2H), 3.08 (d, J_{HH} = 5.8 Hz, 2H), 2.60 (s, 2H), 2.33 – 2.26 (m, 2H), 1.82 – 1.73 (m, 2H).

Preparation of Compound RuGW. A mixture of ligand **16** (57 mg, 0.069 mmol, 1.0 equiv.) and precursor **Ru1** (29 mg, 0.069 mmol, 1.0 equiv.) were dissolved in 25 mL of anhydrous ethanol. This solution was degassed for at least 30 min before being refluxed for 18 h. When the reaction was complete, a solution of ammonium hexafluorophosphate in methanol was added into the reaction mixture to precipitate out an orange solid. This solid was collected by filtration and purified by silica gel column chromatography using $CH_3CN/KPF_6/H_2O$ (7:1:0.5) eluent. The final product was collected as a deep orange powder (74%). ^{1}H NMR (CD_3CN, 500 MHz) δ (ppm) = 9.16 (d, J_{HH} = 3.3 Hz, 2H), 8.54 (d, J_{HH} = 8.3 Hz, 2H), 8.46 (d, J_{HH} = 8.1 Hz, 2H), 8.37 (t, J_{HH} = 8.3 Hz, 1H), 8.30 (s, 2H), 7.73 (t, J_{HH} = 7.8 Hz, 2H), 7.41 (d, J_{HH} = 7.7 Hz, 1H), 7.22 (d, J_{HH} = 5.5 Hz, 1H), 7.15 (d, J_{HH} = 7.7 Hz, 1H), 7.06 – 7.00 (m, 9H), 7.00 – 6.97 (m, 4H), 6.92 (t, J_{HH} = 7.8 Hz, 1H), 6.82 (s, 2H), 6.46 (d, J_{HH} = 7.7 Hz, 1H), 6.31 (t, J_{HH} = 2.7 Hz, 2H), 6.24 (t, J_{HH} = 2.7 Hz, 1H), 6.18 (d, J_{HH} = 8.0 Hz, 1H), 4.65 (t, J_{HH} = 6.1 Hz, 2H), 4.16 (t, J_{HH} = 6.0 Hz, 2H), 4.03 (t, J_{HH} = 7.8 Hz, 1H), 3.65 (s, 2H), 3.53 (t, J_{HH} = 6.2 Hz, 2H), 3.27 (q, J_{HH} = 7.1 Hz, 1H), 2.97 (d, J_{HH} = 8.0 Hz, 2H), 2.51 (t, J_{HH} = 6.4 Hz, 2H), 2.32 (p, J_{HH} = 6.2 Hz, 2H), 1.66 (p, J_{HH} = 6.3 Hz, 2H). ^{13}C NMR ($CDCl_3$, 150.9 MHz): δ (ppm) = 166.55, 160.35, 160.16, 158.85, 157.44, 153.30, 149.31, 145.45, 144.08, 140.25, 139.59, 138.08,

134.97, 133.72, 131.79, 131.16, 130.08, 128.38, 128.12, 127.13, 126.59, 126.27, 126.13, 124.41, 110.97, 110.30, 109.38, 107.09, 106.62, 101.36, 67.23, 65.37, 64.09, 59.38, 55.85, 50.46, 49.62, 45.57, 28.83, 26.42, 7.94. ESI-MS(+) calc. for $C_{60}H_{53}ClF_3N_9O_3Ru$ $[M]^{2+}$ = 1141.2955, found 1141.2903

Preparation of Compound 18. A mixture of 4-(4-methylphenyl)pyridine (1.09 mL, 6.36 mmol, 1.0 equiv.), *N*-bromosuccinimide (1.366 g, 7.6 mmol, 1.3 equiv.), and benzoyl peroxide (31 mg, 0.13 mmol, 0.02 equiv.) were mixed in 30 mL of CCl_4. The solution was degassed for 30 min and then refluxed overnight. The yellow solid formed was removed by filtration. The organic phase was collected and concentrated under vacuum. The crude material was purified by silica gel column chromatography (1 ethyl acetate: 6 hexane) to afford the desired product as a colorless oil (86% yield). ^{1}H NMR ($CDCl_3$, 500 MHz): δ (ppm) = 8.69 (d, J = 4.6 Hz, 1H), 7.97 (d, J = 8.2 Hz, 2H), 7.78 – 7.69 (m, 2H), 7.48 (s, 2H), 7.25 – 7.22 (m, 1H), 4.54 (s, 2H). ^{13}C NMR ($CDCl_3$, 125.7 MHz): δ (ppm) = 156.73, 149.84, 139.54, 138.59, 136.99, 129.63, 127.44, 122.51, 120.72, 33.35. GC-MS calc. for $C_{19}H_{25}NO_4$ $[M]^+$ = 247.0, found 247.2.

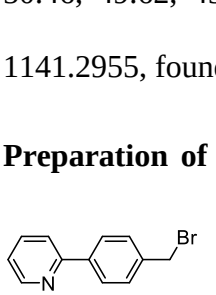

Preparation of Compound 19. Compound **GW3965** (89.6 mg, 0.154 mmol, 1.0 equiv.) and compound **18** (53 mg, 0.21 mmol, 1.4 equiv.) were added to a round bottom flask along with K_2CO_3 (74 mg, 0.3 mmol, 2.0 equiv.) and CH_3CN (10 mL). The reaction mixture was then refluxed overnight under a N_2 flow. After the reaction was complete, K_2CO_3 was removed by filtration. The filtrate was concentrated. Column chromatography was performed (1 Ethyl acetate: 6 Hexane) to obtain product as a colorless oil (84% yield). ^{1}H NMR ($CDCl_3$, 500 MHz) δ (ppm) = 8.70 (dd, J_{HH} = 4.7, 1.6 Hz, 1H), 7.99 (d, J_{HH} = 8.0 Hz, 2H), 7.76 – 7.67 (m, 2H), 7.45 (dd, J_{HH} = 12.0, 7.8

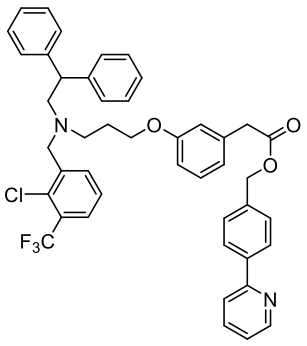

Hz, 3H), 7.28 – 7.13 (m, 13H), 6.94 – 6.85 (m, 2H), 6.71 (t, J_{HH} = 2.1 Hz, 1H), 6.68 (dd, J_{HH} = 8.2, 2.5 Hz, 1H), 5.22 (s, 2H), 4.15 (t, J_{HH} = 7.4 Hz, 1H), 3.79 (s, 2H), 3.69 (s, 2H), 3.67 (t, J_{HH} = 5.9 Hz, 2H), 3.15 (d, J_{HH} = 7.7 Hz, 2H), 2.71 (t, J_{HH} = 6.4 Hz, 2H), 1.84 (p, J_{HH} = 6.2 Hz, 2H). ^{13}C NMR ($CDCl_3$, 125.7 MHz): δ (ppm) = 171.42, 159.15, 156.94, 149.86, 143.58, 139.81, 139.42, 136.94, 136.72, 135.28, 133.94, 131.35, 129.64, 128.66, 128.51, 128.37, 127.19, 126.48, 126.32, 125.91, 125.87, 122.43, 121.62, 120.63, 115.45, 113.40, 6.40, 64.97, 60.40, 56.15, 50.85, 49.85, 41.55, 26.93, 14.35. ESI-MS(+) calc. for $C_{45}H_{40}ClF_3N_2O_3$ $[M+H]^+$ = 749.2758, found 749.2753.

Preparation of Compound IrGW. A mixture of precursor **Ir2** (63 mg, 0.018 mmol, 1.0 equiv.) and compound **19** (7 mg, 0.04 mmol, 2.2 equiv.) were dissolved in 10 mL of MeOH/DCM (2:1). This solution was degassed for at least 30 min before being refluxed for 4 h. After cooling the mixture to room temperature, ammonium hexafluorophosphate (12 mg, 0.074 mmol, 4 mmol) was added and the mixture was stirred at room temperature overnight. The solvent was removed, and the crude solid was purified by silica gel column chromatography using DCM/ MeOH (2-10%) eluent. The final product was collected as a yellow powder (89% yield). ^{1}H NMR ($CDCl_3$, 500 MHz) δ (ppm) = 8.63 (d, J_{HH} = 8.2 Hz, 2H), 8.07 (t, J_{HH} = 7.8 Hz, 2H), 7.83 (t, J_{HH} = 7.1 Hz, 4H), 7.71 (t, J_{HH} = 7.8 Hz, 2H), 7.62 (d, J_{HH} = 8.0 Hz, 2H), 7.47 (d, J_{HH} = 5.7 Hz, 2H), 7.43 (d, J_{HH} = 7.7 Hz, 2H), 7.28 (d, J_{HH} = 6.5 Hz, 2H), 7.23 – 7.09 (m, 24H), 7.00 (m, 4H), 6.86 (t, J = 7.7 Hz, 2H), 6.80 (d, J_{HH} = 7.6 Hz, 2H), 6.61 (m, 4H), 6.18 (s, 2H), 4.90 (s, 4H), 4.11 (t, J_{HH} = 7.6 Hz, 2H), 3.77 (s, 4H), 3.63 (t, J_{HH} = 5.7 Hz, 4H), 3.54 (s, 4H), 3.13 (d, J_{HH} = 7.7 Hz, 4H), 2.68 (t, J_{HH} = 6.3 Hz, 4H), 1.85 – 1.78 (m, 4H). ESI-MS(+) calc. for $C_{100}H_{86}Cl_2F_6IrN_6O_6$ $[M]^+$ = 1843.5519, found 1843.5587.

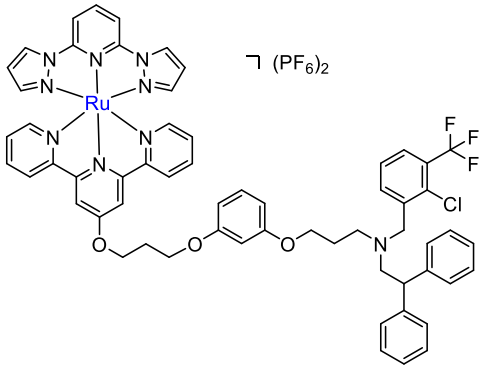

3.4.3 Fluorescence Imaging Studies

A549 and MCF-7 cells were cultured at 37°C under a 5% CO_2 humidified atmosphere in Dulbecco's Modified Eagle Medium (DMEM) supplemented with 10% fetal bovine serum (FB Essence from VWR) and 1% penicillin streptomycin solution (100×). For live cell imaging, cells were plated in μ-Slide 8-well plates (IBIDI) in 200 μL of DMEM in each well. After overnight cell growth, the medium was removed and cells were treated with a mixture of 5 μM **IrGW**, Mito-ID, and Hoechst 33342 in 300 μL of DMEM. After an incubation time of 30 mins (37 °C, 5% CO_2), the growth solutions were removed, the cells were rinsed with FluoroBrite DMEM (3×500 μL each well), and then visualized immediately using microscopy. In the experiments with A549 cells, images were taken with an Olympus CKX53 inverted microscope equipped with a scientific CMOS camera (Photometric Prime 95B) and a 100× TIRF oil immersion objective (Olympus UApoN 100× TIRF). The samples were illuminated with a 100 W mercury lamp (U-LH100HG) at ambient temperature, and the "umbra shield" was applied to block out room light, in order to enhance the contrast of fluorescence. The experiments with MCF-7 cells were performed using an Olympus IX83 with a 60× objective. The excitation wavelength was 488 nm for **IrGW** (emission filter: 525 ± 25 nm), 405 nm for Hoechst 33342 (emission filter: 438 ± 12 nm), and 561 nm for Mito-ID (emission filter: 618 ± 12 nm). The images were processed by subtracting background emission and emission from control cells using the program ImageJ and PCC values were calculated using JACoP plugin for Pearson's Correlation Coefficient.[137]

.

3.5 Spectral Characterization

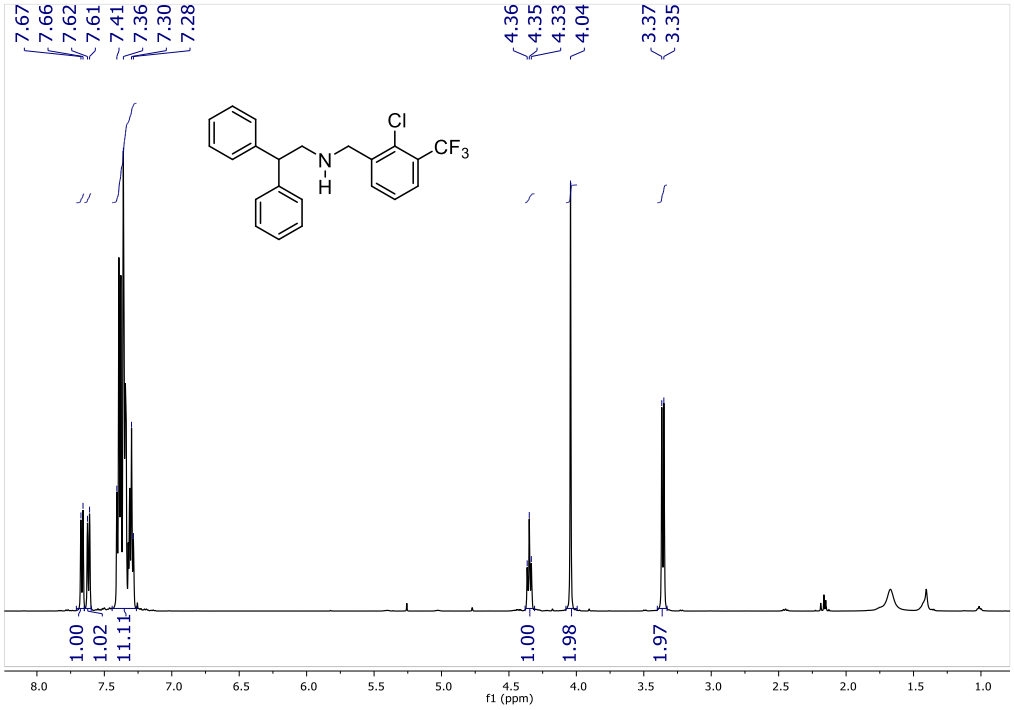

Figure 3.7 ^{1}H NMR spectrum ($CDCl_3$, 500 MHz) of compound **9**.

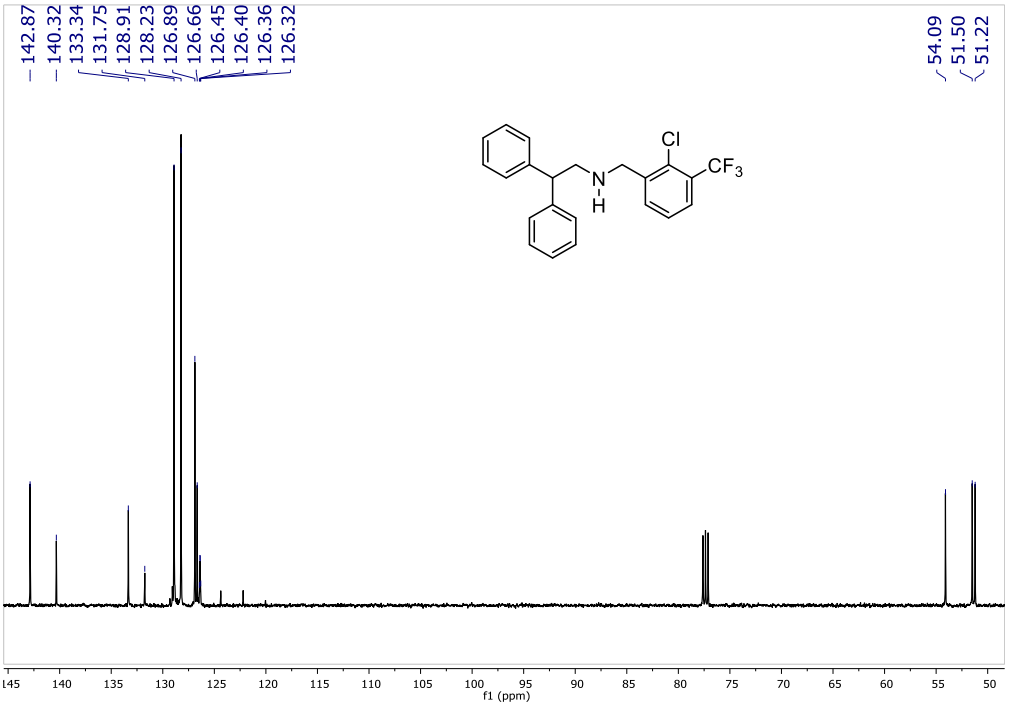

Figure 3.8 ^{13}C NMR spectrum ($CDCl_3$, 126 MHz) of compound **9**.

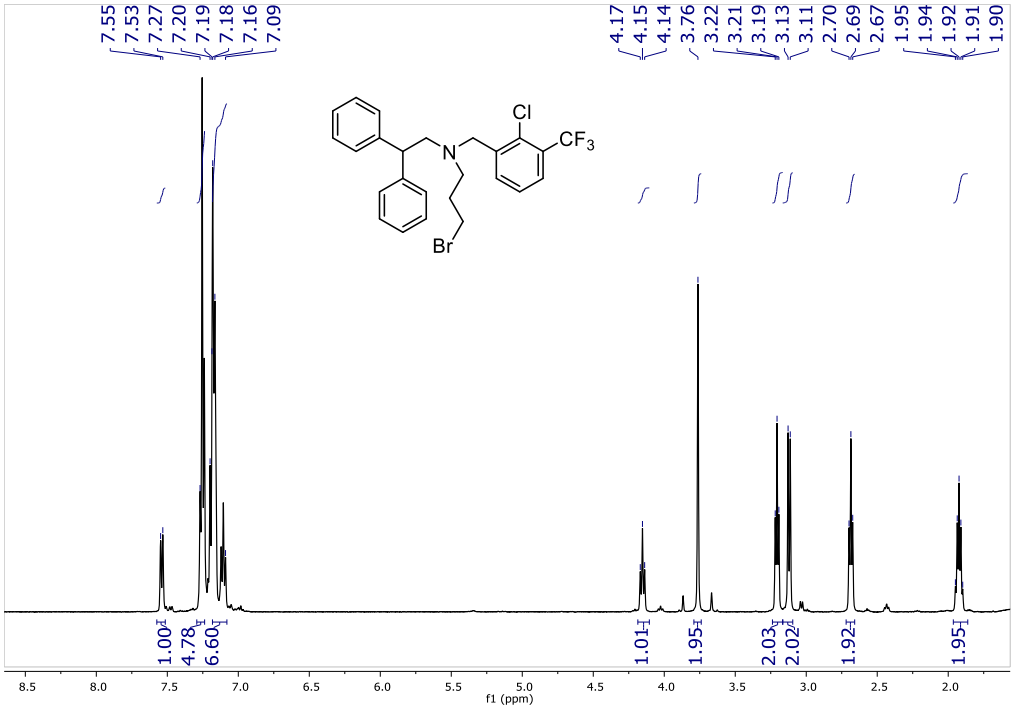

Figure 3.9 ^{1}H NMR spectrum ($CDCl_3$, 500 MHz) of compound **10**.

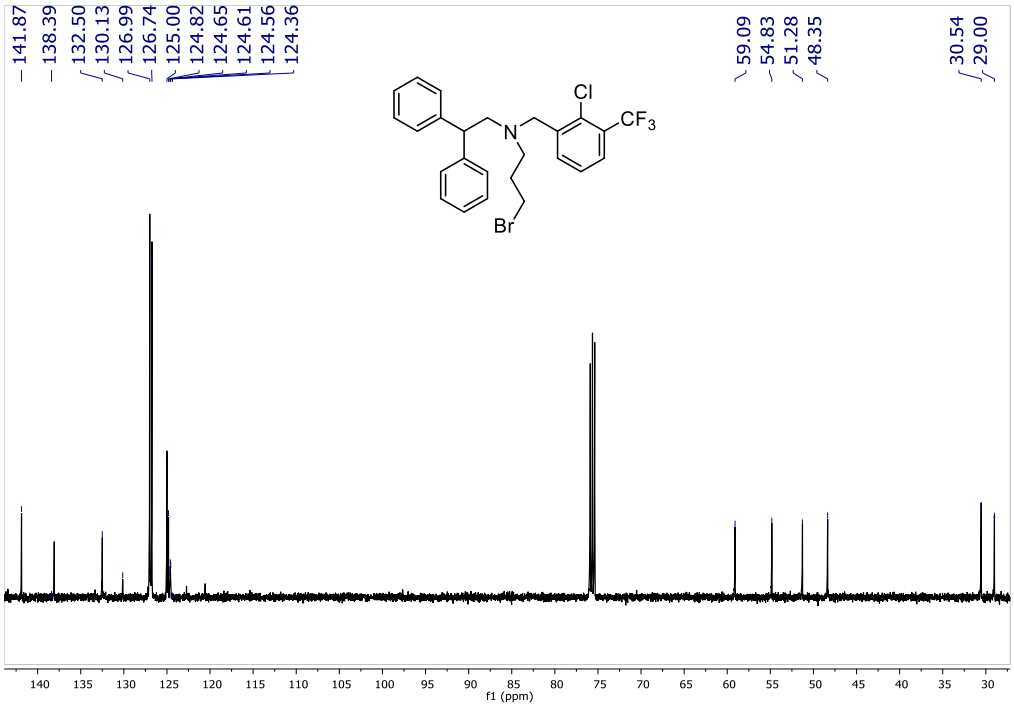

Figure 3.10 ^{13}C NMR spectrum ($CDCl_3$, 126 MHz) of compound **10**.

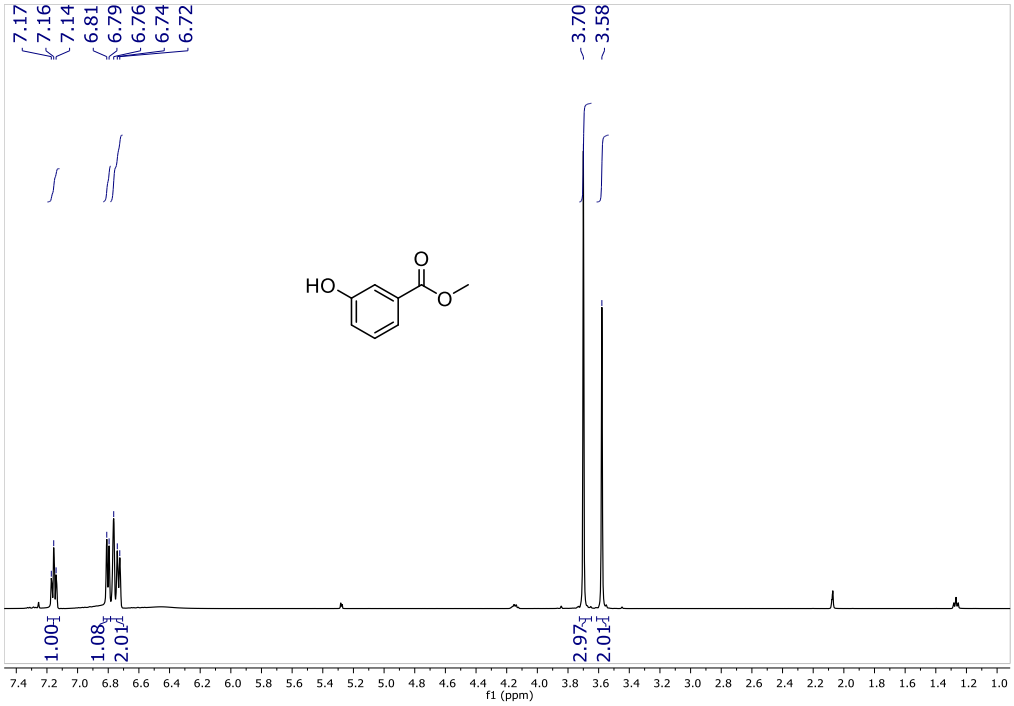

Figure 3.11 ^{1}H NMR spectrum ($CDCl_3$, 500 MHz) of compound **11.**

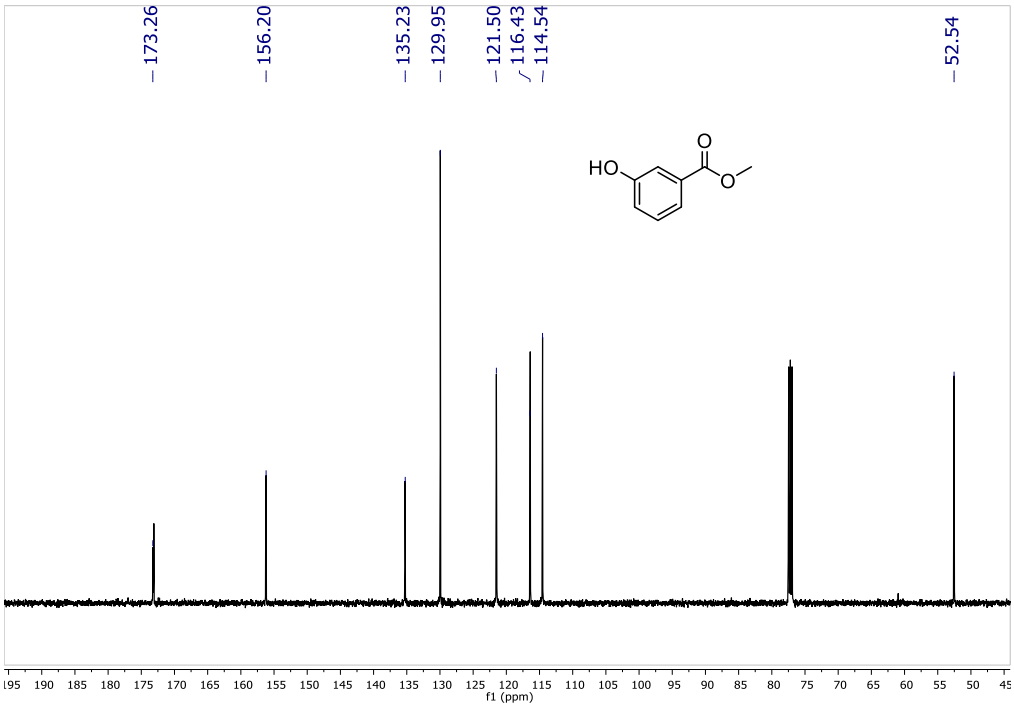

Figure 3.12 ^{13}C NMR spectrum ($CDCl_3$, 126 MHz) of compound **11.**

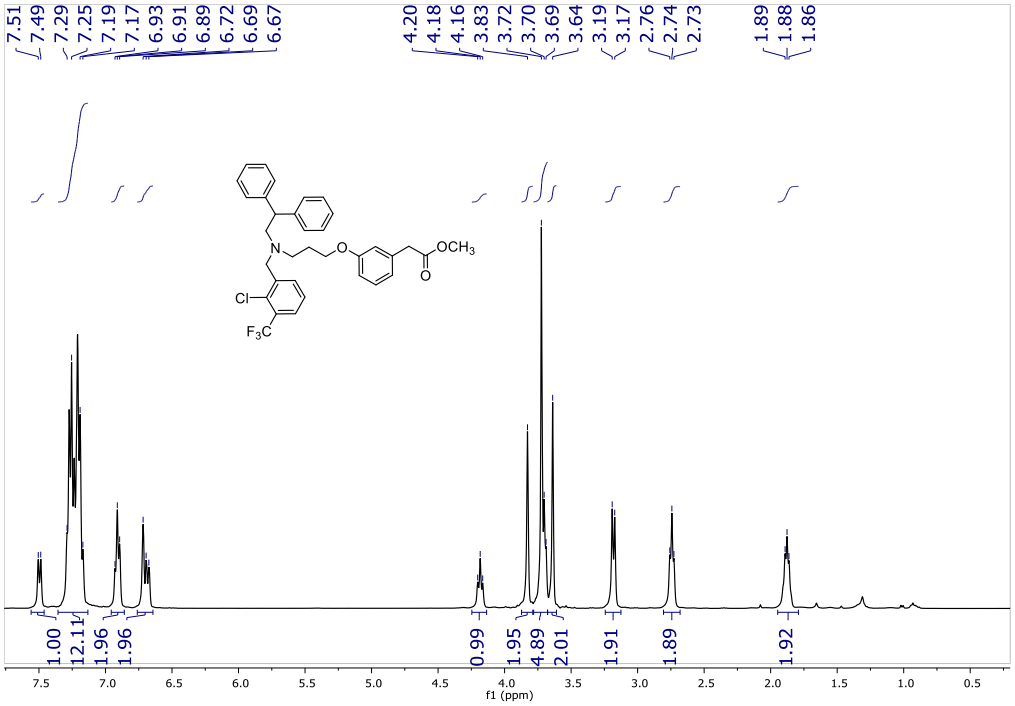

Figure 3.13 ^{1}H NMR spectrum ($CDCl_3$, 400 MHz) of compound **12.**

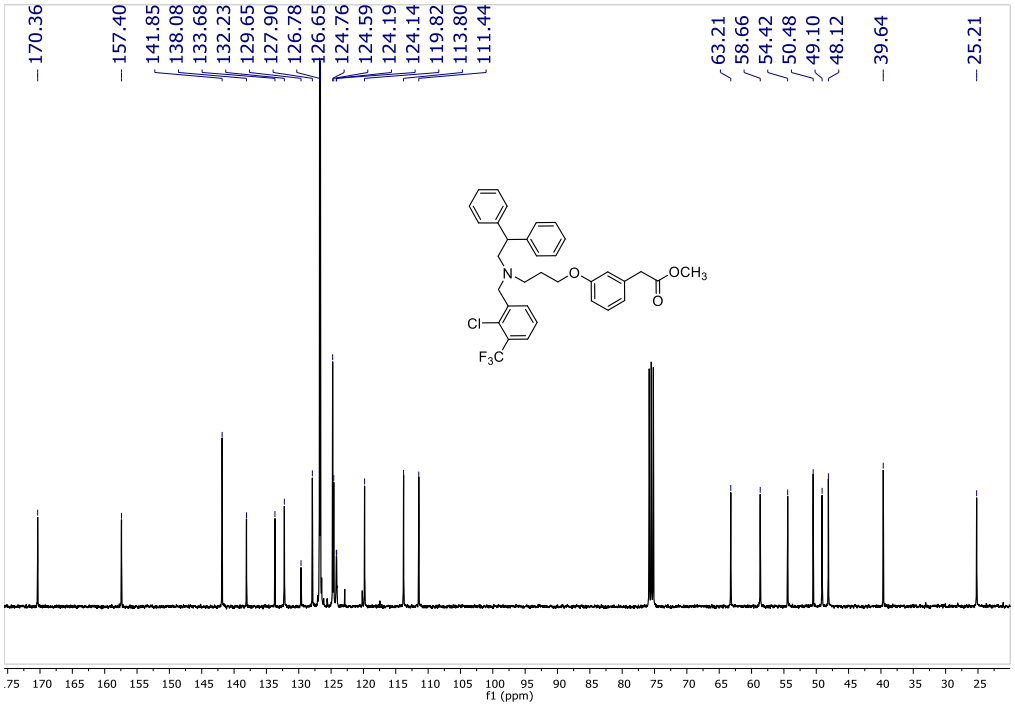

Figure 3.14 ^{13}C NMR spectrum ($CDCl_3$, 100 MHz) of compound **12.**

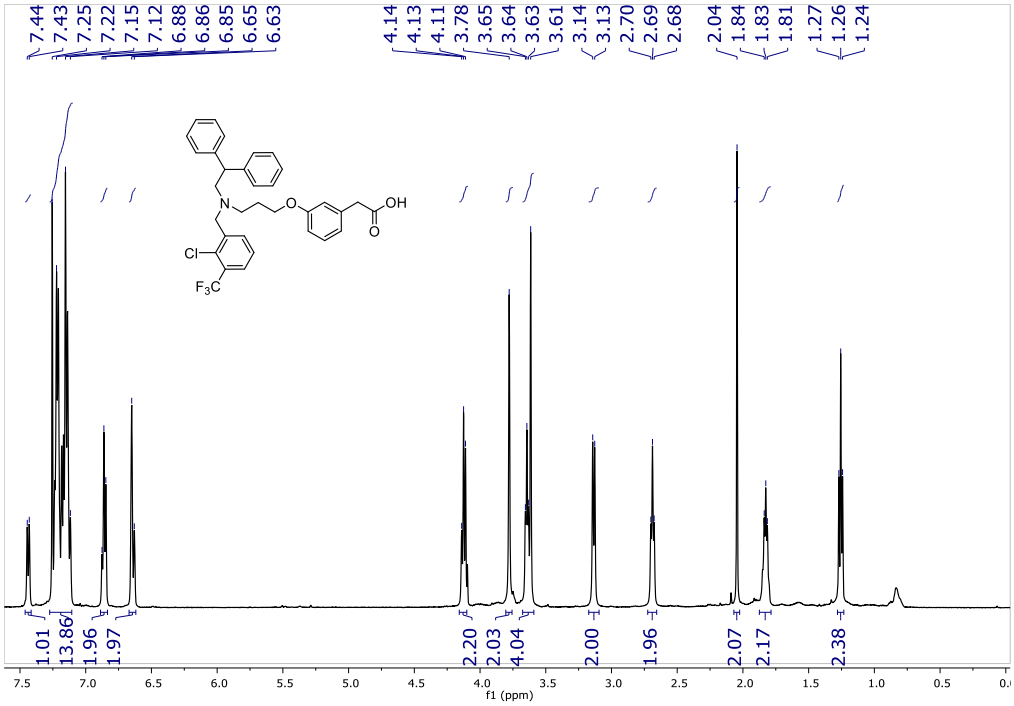

Figure 3.15 ^{1}H NMR spectrum ($CDCl_3$, 500 MHz) of compound **GW3965.**

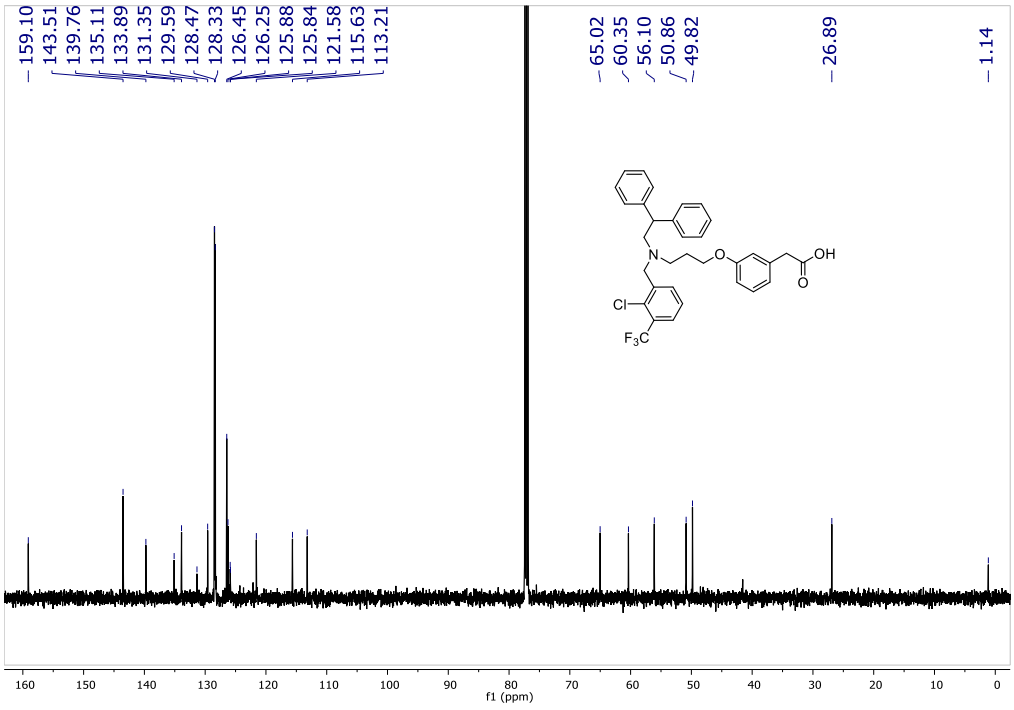

Figure 3.16 ^{13}C NMR spectrum ($CDCl_3$, 126 MHz) of compound **GW3965.**

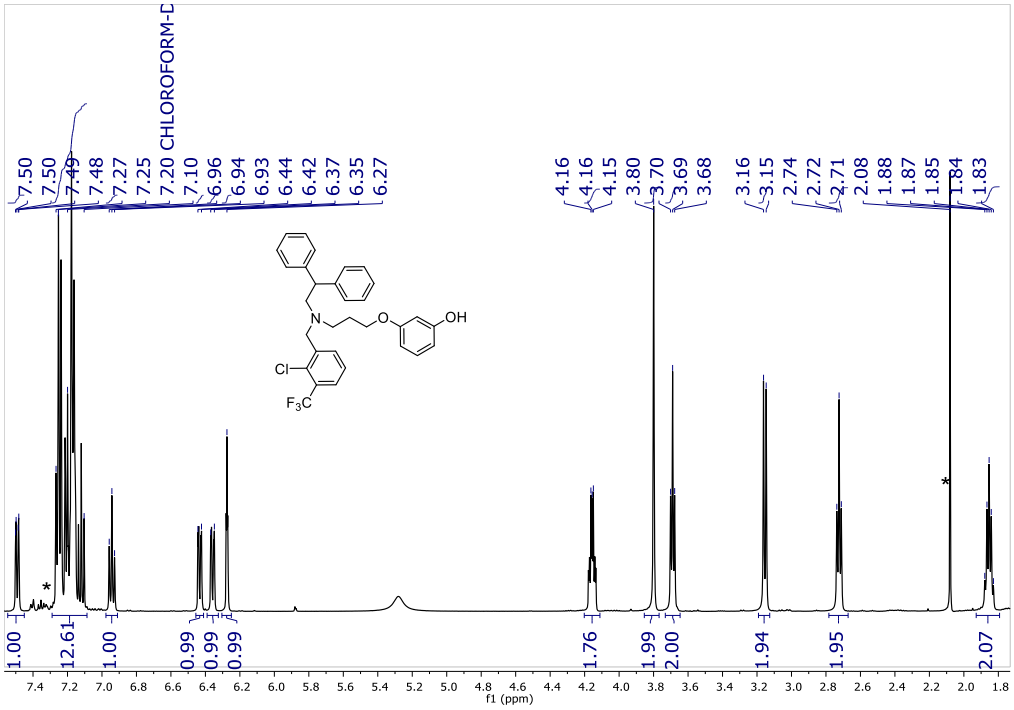

Figure 3.17 ^{1}H NMR spectrum ($CDCl_3$, 500 MHz) of compound **GW3965b.**

Peaks corresponding to trace impurities are marked with "*".

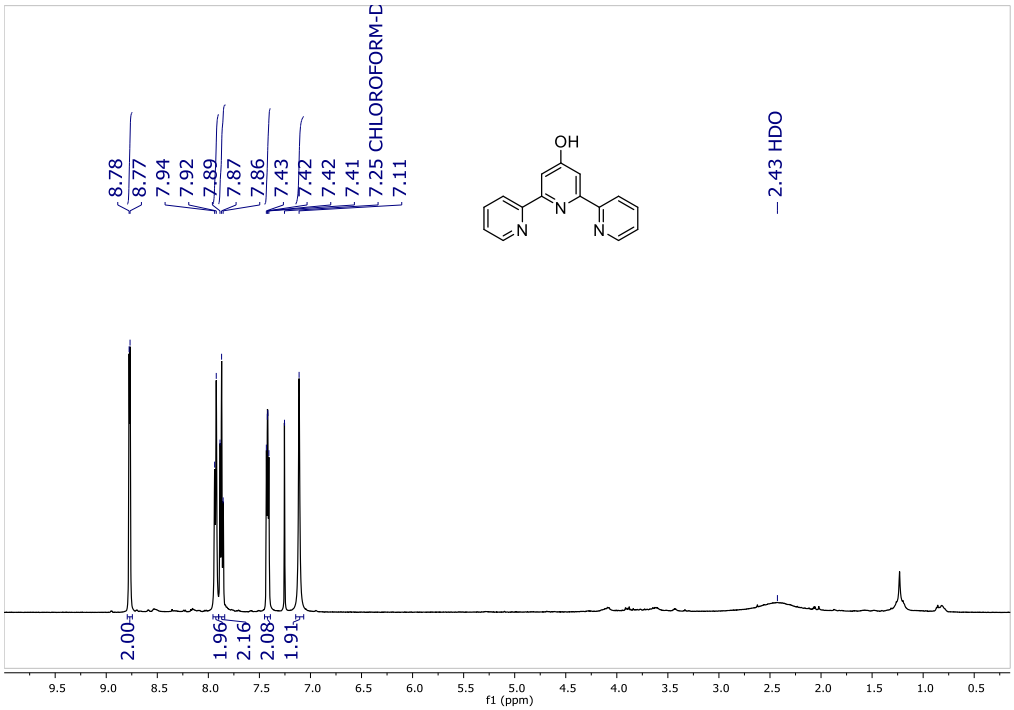

Figure 3.18 ^{1}H NMR spectrum ($CDCl_3$, 500 MHz) of compound **14.**

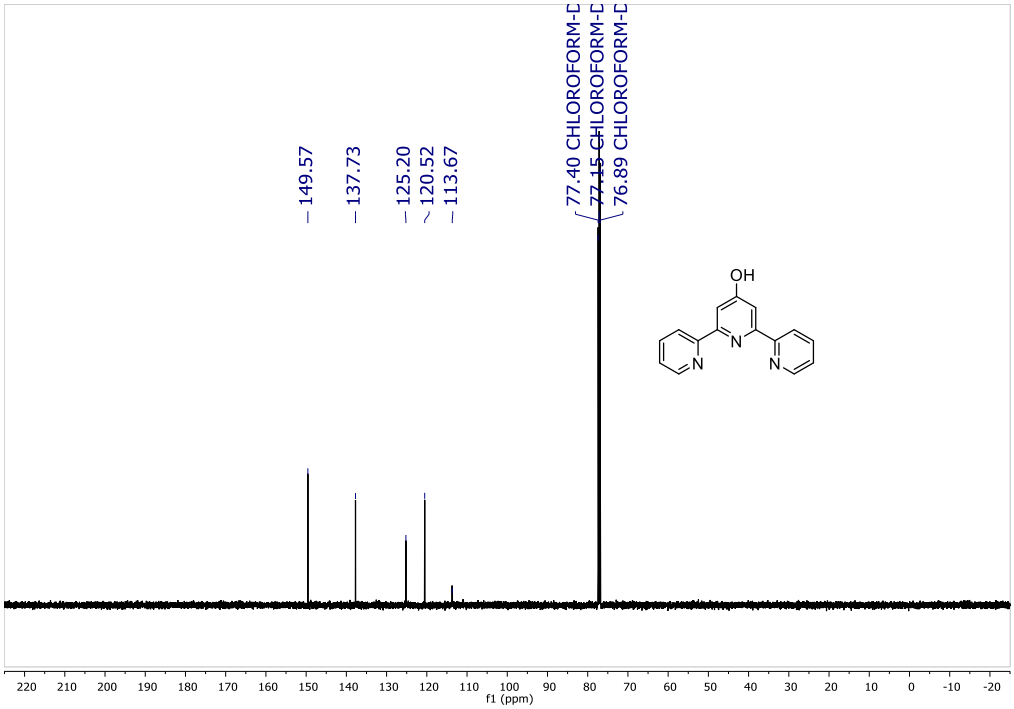

Figure 3.19 ^{13}C NMR spectrum ($CDCl_3$, 126 MHz) of compound **14.**

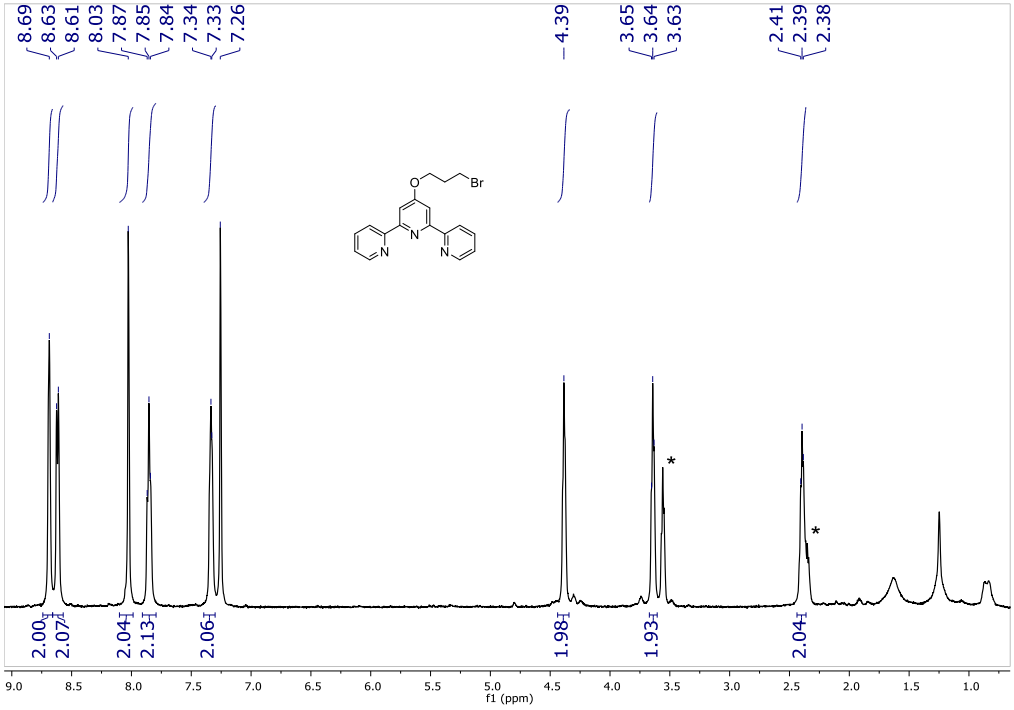

Figure 3.20 ^{1}H NMR spectrum ($CDCl_3$, 500 MHz) of compound **15.**

Peaks corresponding to excess 1,3-dibromopropane are marked with "*".

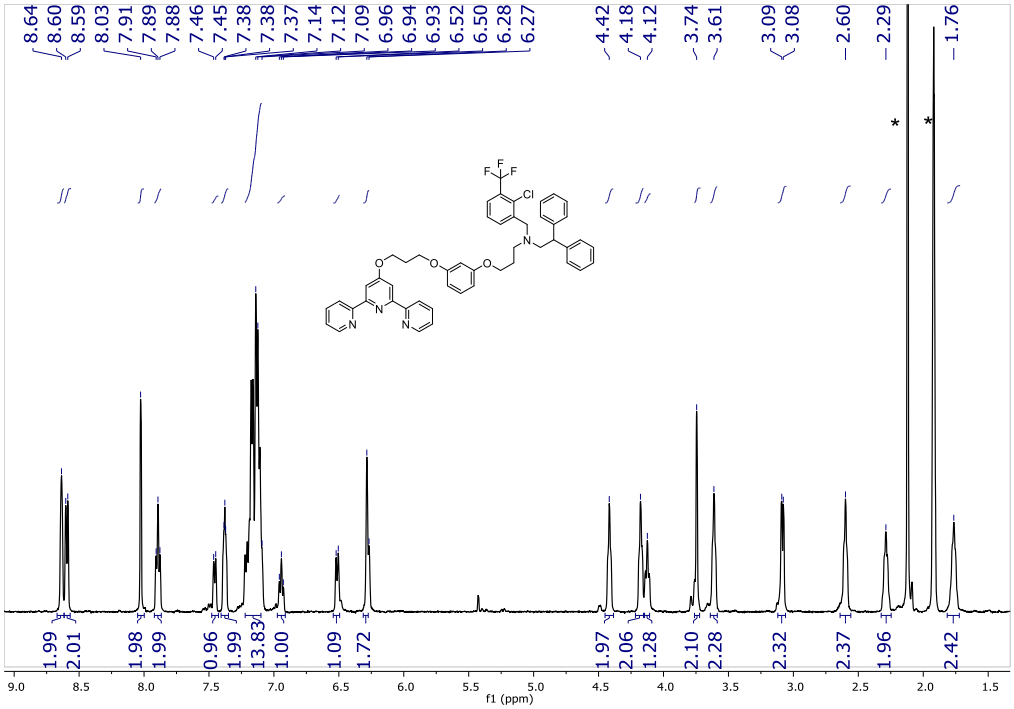

Figure 3.21 ^{1}H NMR spectrum (CD_3CN, 500 MHz) of compound **16.**

Solvent peaks are marked with "*".

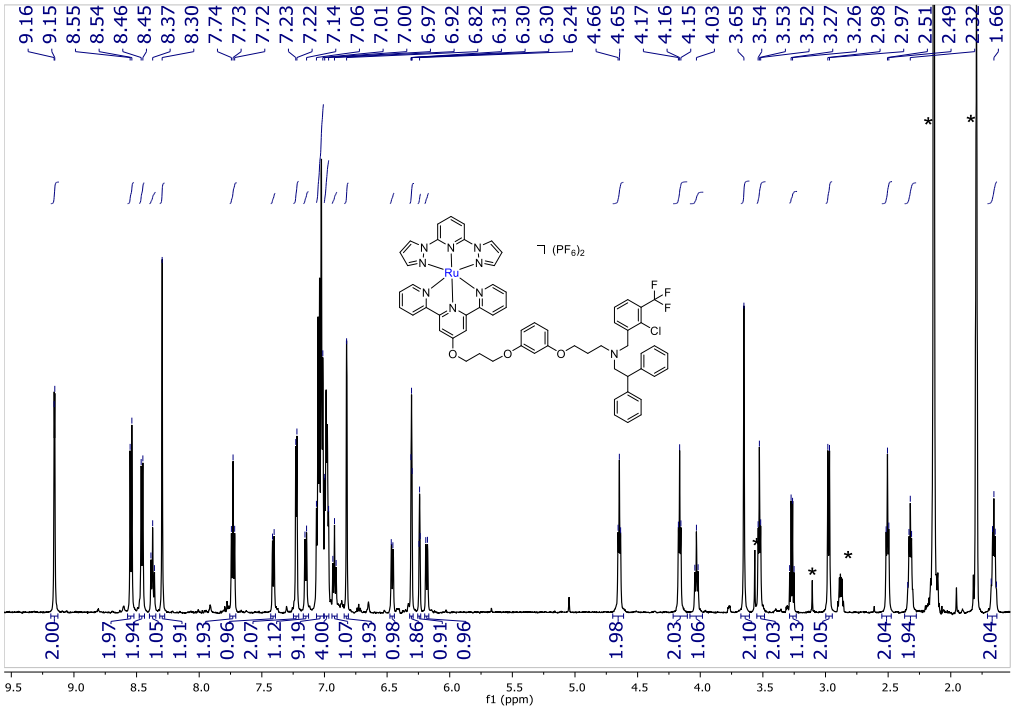

Figure 3.22 ^{1}H NMR spectrum (CD_3CN, 600 MHz) of compound **RuGW.**

Peaks corresponding to impurities present are marked with "*".

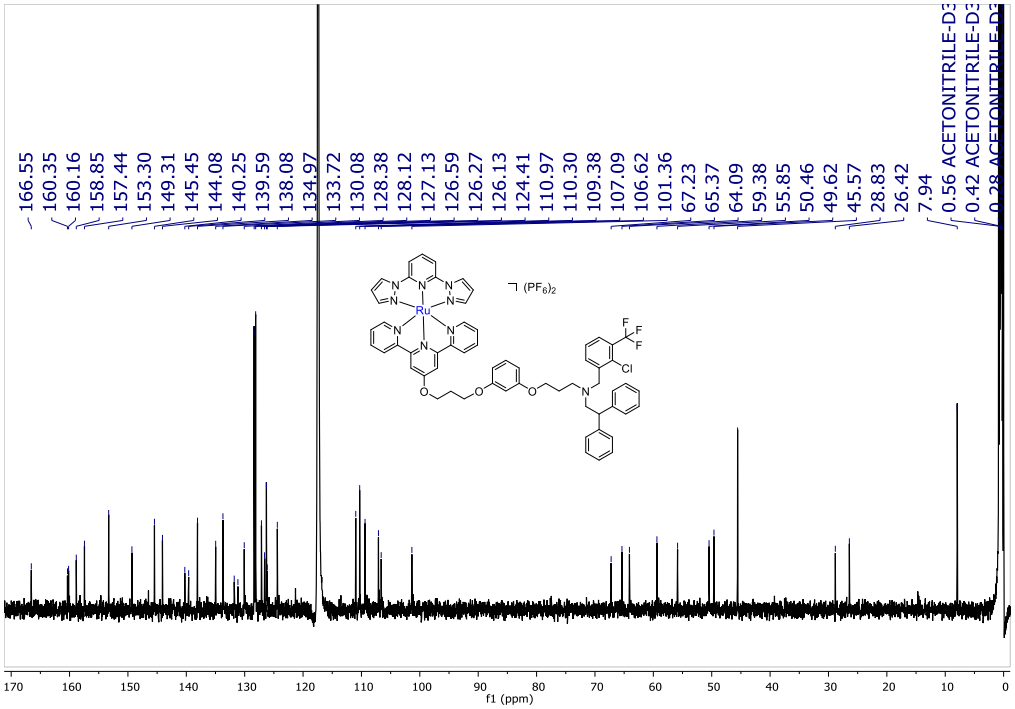

Figure 3.23 ^{13}C NMR spectrum (CD_3CN, 151 MHz) of compound **RuGW.**

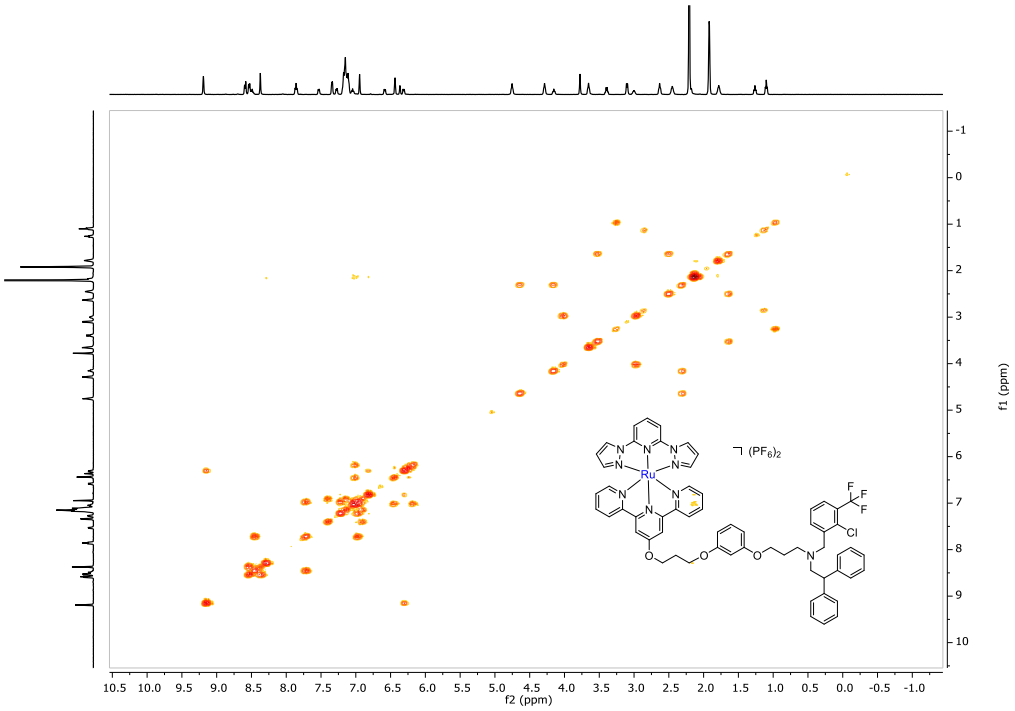

Figure 3.24 COSY NMR spectrum (CD_3CN, 600 – 600 MHz) of compound **RuGW.**

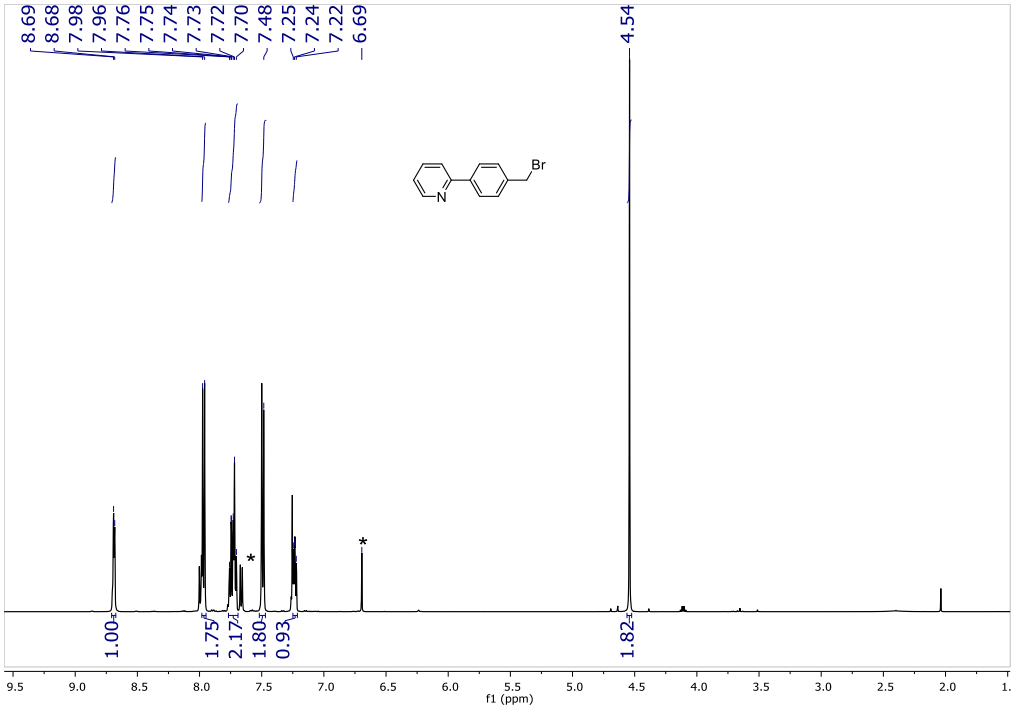

Figure 3.25 ^{1}H NMR spectrum ($CDCl_3$, 500 MHz) of compound **18.**

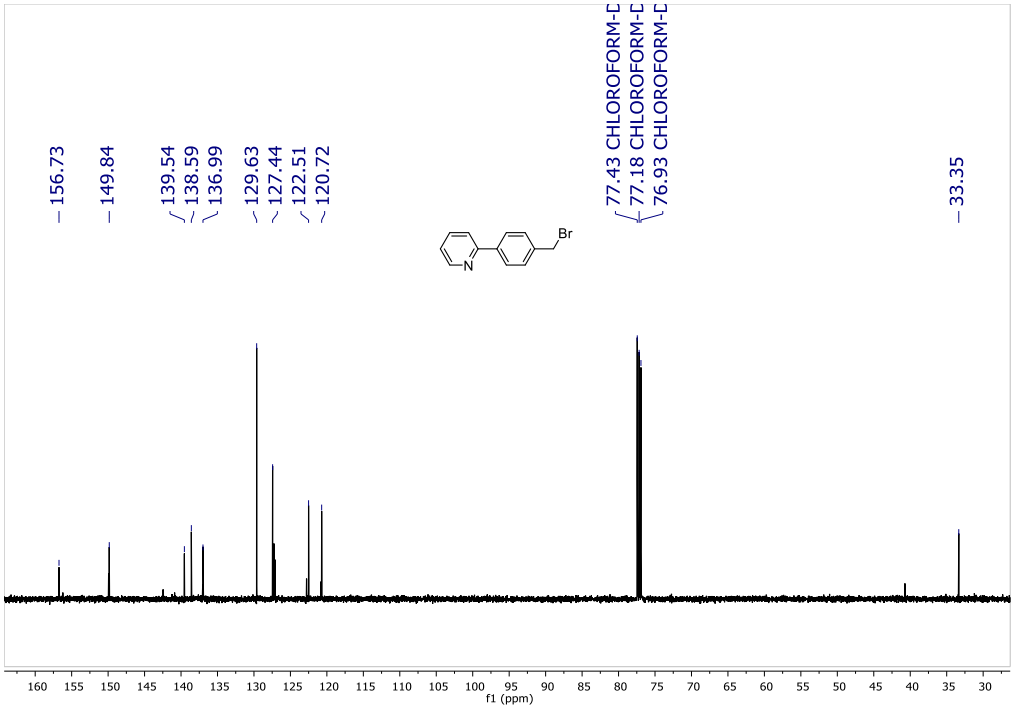

Figure 3.26 ^{13}C NMR spectrum ($CDCl_3$, 126 MHz) of compound **18.**

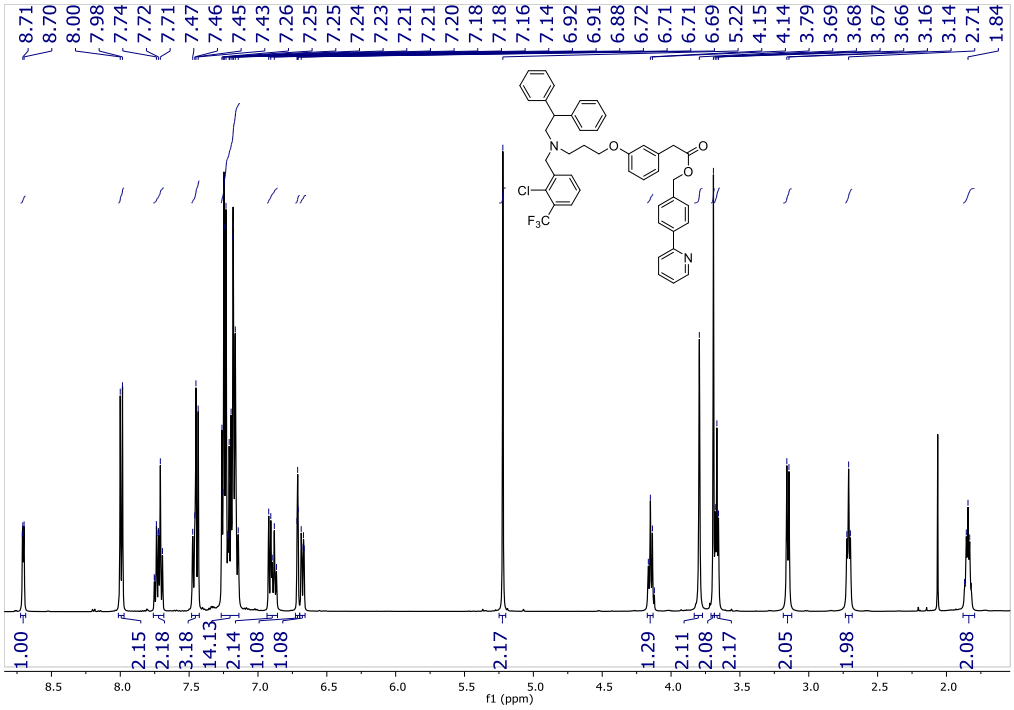

Figure 3.27 ^{1}H NMR spectrum ($CDCl_3$, 500 MHz) of compound **19.**

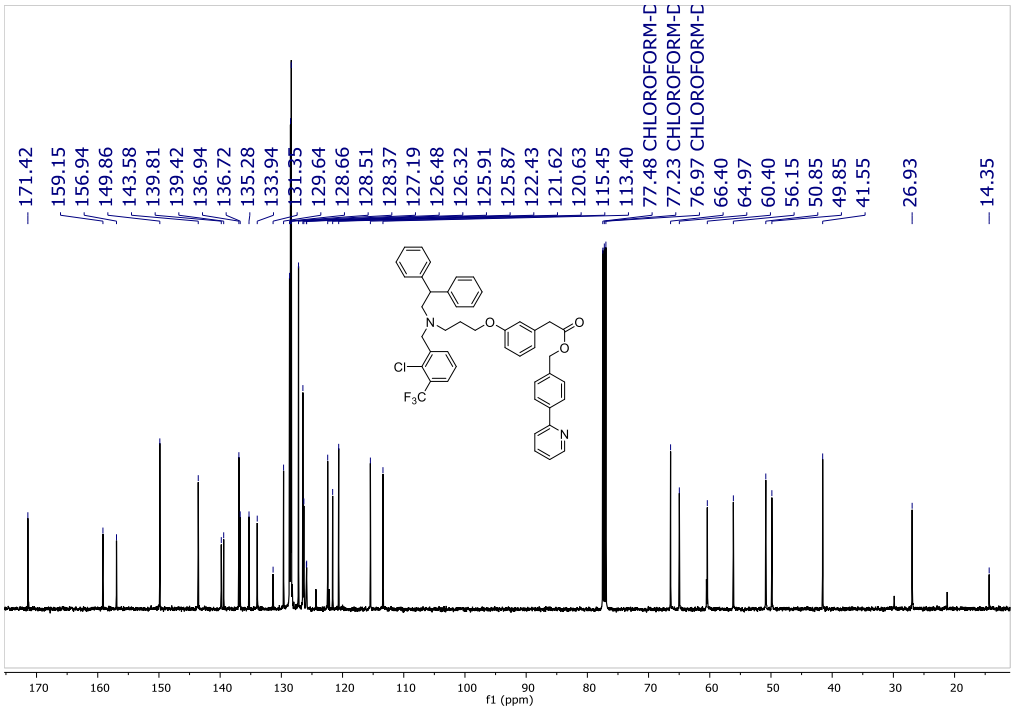

Figure 3.28 ^{13}C NMR spectrum ($CDCl_3$, 126 MHz) of compound **19.**

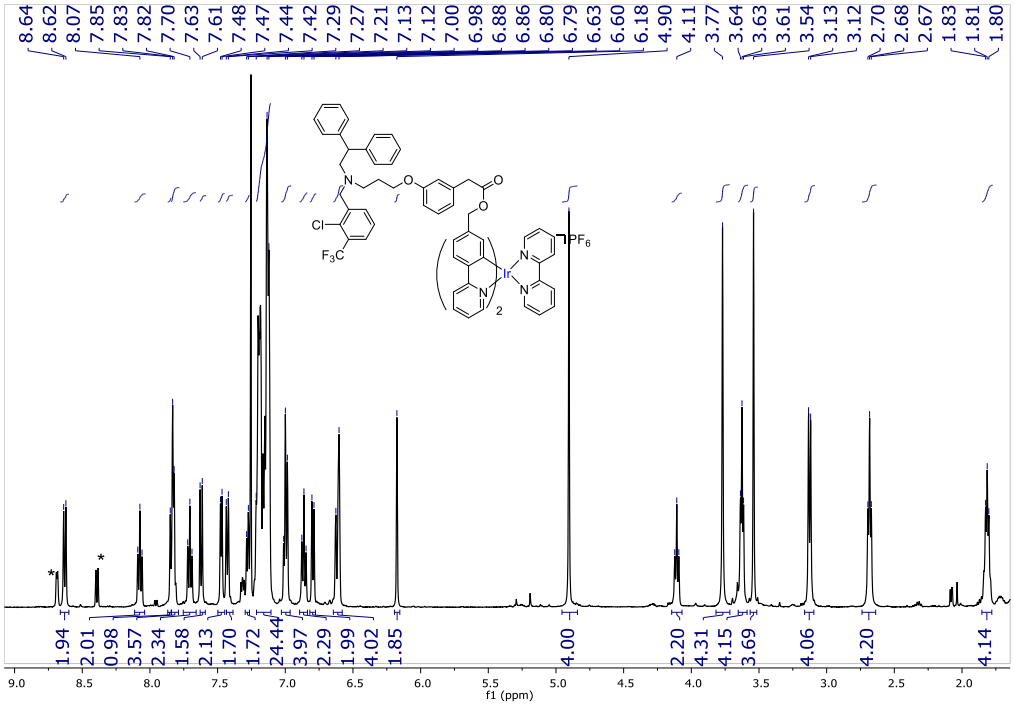

Figure 3.29 ^{1}H NMR spectrum ($CDCl_3$, 500 MHz) of compound **IrGW**.

Chapter 4. Fluorescent Probes for Quantifying Intracellular Transfer Hydrogenation

4.1 Introduction

Transfer hydrogenation catalysis has been studied for several decades. Ruthenium, rhodium, iridium, and osmium complexes have been shown to have good homogeneous catalytic activity in aqueous media.[8] These complexes are also known for the ability to transfer a hydride from the biological cofactor nicotinamide adenine dinucleotide (NADH) to organic receptors.[57] It is challenging to perform this reaction inside living cells because the presence of biological nucleophiles, electrophiles, and redox active compounds may be incompatible with the transfer hydrogenation catalyst. In 2014, Komatsu, Ariga, and coworkers used Ir(Cp*)(1,10-phenanthroline)(H_2O)$^+$ to catalyze the reduction of fluorescent ubiquinone-rhodol derivative using NADH as the hydride source.[138] This work demonstrated a new approach to study synthetic reactions in living systems. In 2017, our group reported the reduction of carbonyl compounds using unprotected organoiridium complexes inside cells. By using a fluorogenic aldehyde-containing probe, we were able to monitor the reaction using confocal fluorescence microscopy.[44]

Here in, we aim to prepare novel off – on and colorimetric aldehyde-containing probes that can be used to study intracellular transfer hydrogenation reactions. The well-known cyclometalated Ir(phenylpyridine)$_2$(bipyridine)$^+$ complex was our chosen as the fluorogenic unit because it is straightforward to synthesize, and its 6-coordinate structure precludes reactivity with external reagents.

4.2 Preliminary Results

To begin the synthesis, our first metallosubstrate design is shown in Scheme 4.1. 2,9-dimethyl phenanthroline was oxidized using selenium dioxide in dioxan to give **20**. This

compound was combined with $[Ir(ppy)_2Cl]_2$ (ppy = phenylpyridine) to afford **Ir4** in 7% yield (Scheme 4.1). We hypothesized that the steric bulk and poor solubility of the phenanthroline derivative is responsible for the low reaction yield. We proposed that when the aldehyde groups in **Ir4** are reduced, the electronic changes in the complex would lead to fluorescence turn on.

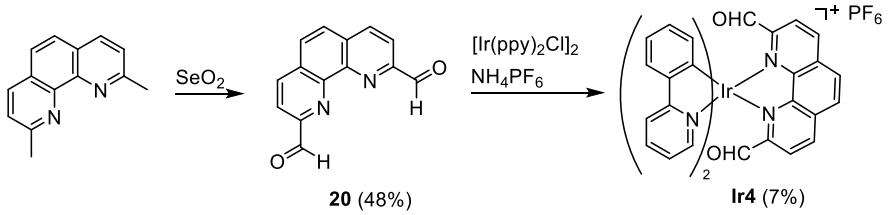

Scheme 4.1 Synthesis of complex **Ir4**

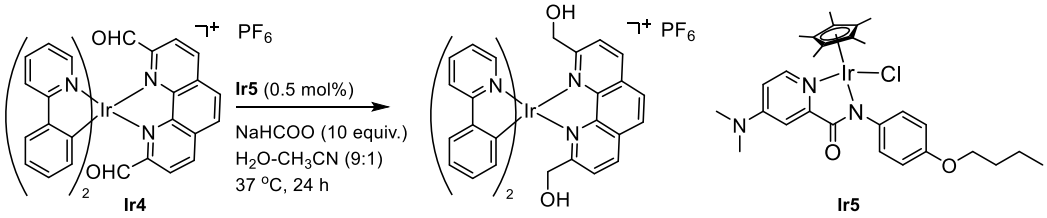

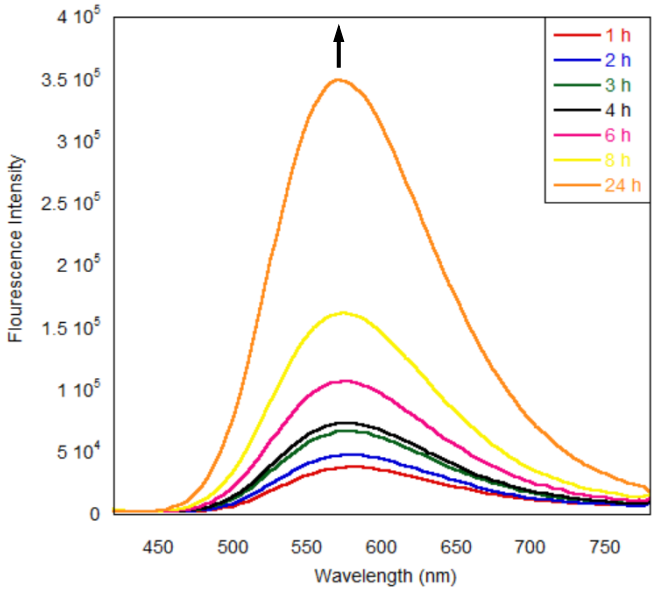

Figure 4.1 Transfer hydrogenation of complex **Ir4** in CH_3CN/H_2O (9:1)

To study the transfer hydrogenation reaction, substrate **Ir4,** catalyst **Ir5,** and sodium formate were mixed in a cuvette at room temperature. The mixture was then heat to 37 °C and was monitored for 24 h by fluorescence spectroscopy (Fig. 4.1). After the reaction was complete, the aldehyde groups were reduced to alcohols and an increase in fluorescence intensity was observed. However, the integrated fluorescence does not have a linear correlation with reaction time. One of the possibilities is that the observed fluorescence signal was from a mixture of the singly reduced and the doubly reduced products. These results suggested that having two aldehyde groups in a single substrate can complicate data analysis.

A second probe was designed containing only one aldehyde group. Using the same synthetic strategy, the first step was to oxidize of 4,4'-dimethyl-2,2'-bipyridine, followed by metalation with the precursor $[Ir(ppy)_2Cl]_2$. Unfortunately, our preliminary results showed that there is only a minor change in the fluorescence intensity of the probe $[Ir(ppy)_2bpyCHO]^+$ (**Ir6a –** red line) and its reduced product **Ir6b** (blue line) (Fig. 4.2).

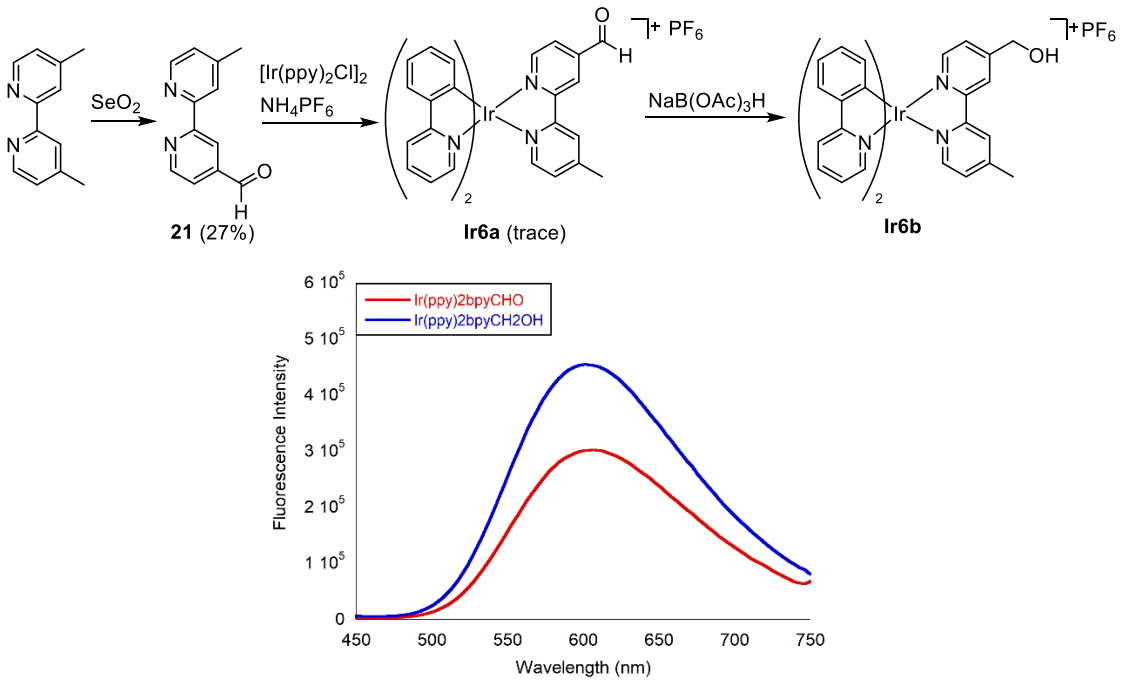

Figure 4.2 Synthesis and fluorescence spectra of complex **Ir6a** and **Ir6b**.

Next, we attempted to design a ratiometric probe based on a strategy introduced by Ward and coworkers.[46] In their work, they used sulfonamide-bearing IrCp* complex to catalyze the reduction of a self-immolative substrates in *E. coli*. Using a similar approach, we designed the quinolinium iridium complex **Ir7**. After the C=N is reduced, the iminoquinonemethide (**22**) would be cleaved, which would then release complex **Ir8** that has an emission wavelength different from that of **Ir7** (Scheme 4.2).

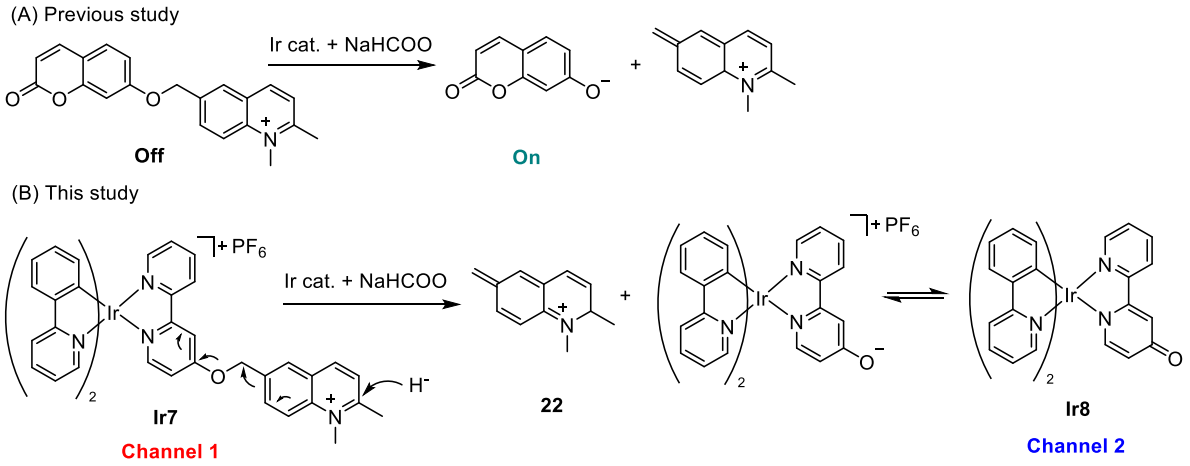

Scheme 4.2 Transfer hydrogenation in the cleavage of iminoquinonemethide.

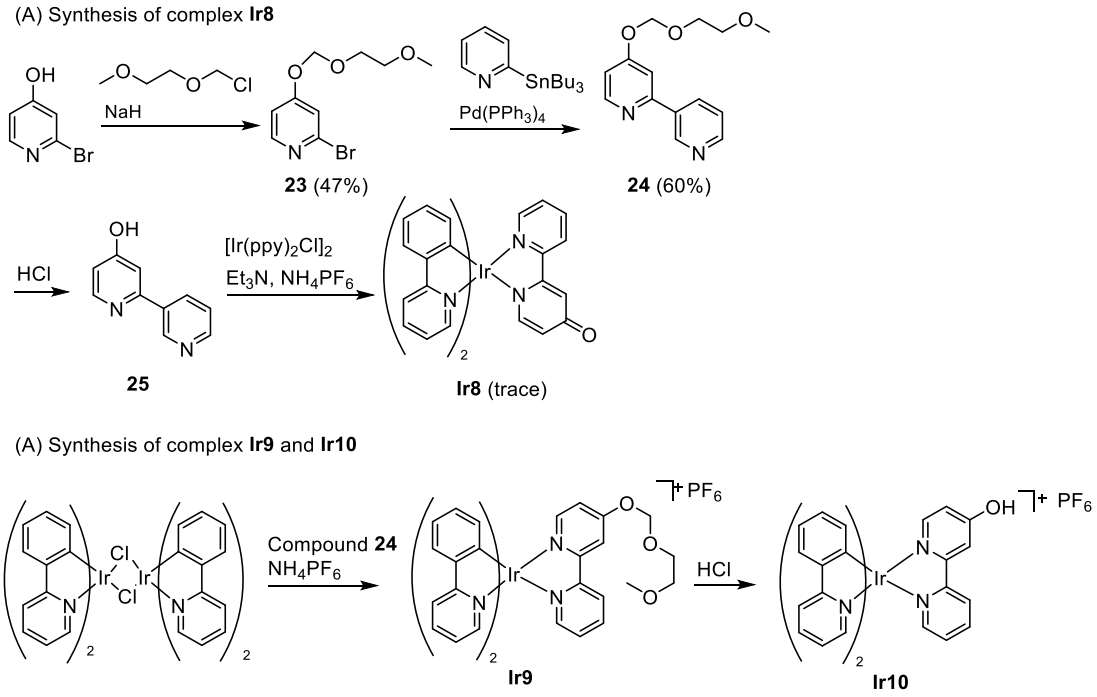

Scheme 4.3 Synthesis of complex **Ir8** and **Ir10**.

Complex **Ir8** was first prepared and tested for its fluorescence properties. Because of the difficulty in the synthesis of the quinolinium iridium complex, we first prepared a derivative with a 2-methoxyethoxymethyl ether protecting group (**Ir9**) and tested the change in its fluorescence signal after deprotection (Scheme 4.3).

In the first step, 2-bromopyridin-4-ol was protected by MEMCl, followed by a Stille coupling reaction to generate an asymmetric bipyridine **24**. The deprotection reaction of compound **24** was performed in acidic condition and compound **25** was obtained as an ammonium salt, which required the addition of triethyl amine in the next metalation step. Complex **Ir8** was collected in low yield (<5% yield) and was characterized by ^{1}H NMR spectroscopy. In an attempt to synthesize complex **Ir9**, a common procedure was followed in which ligand **24** was treated with the precursor $[Ir(ppy)_2Cl]_2$ in 1,2-ethanediol. However, no signal from the 2-methoxyethoxymethyl ether group was detected by ^{1}H NMR spectroscopy. We hypothesize that hydrochloric acid, which formed during this reaction, catalyzed the alcohol deprotection to provide complex **Ir10**.

Interestingly, complexes **Ir8** and **Ir10** are interconvertible, their stability depends on the pH of the work-up solutions. Complex **Ir8** is more stable in a basic environment, it does not precipitate upon treatment with ammonium hexafluorophosphate which suggested that it is a neutral complex. On the other hand, **Ir10** is favorable under acidic conditions. It was purified by precipitation after the addition of ammonium hexafluorophosphate, which suggested that complex **Ir10** contains a cationic center. The two complexes also have different emission wavelengths when being excited by a UV light source (Fig. 4.3).

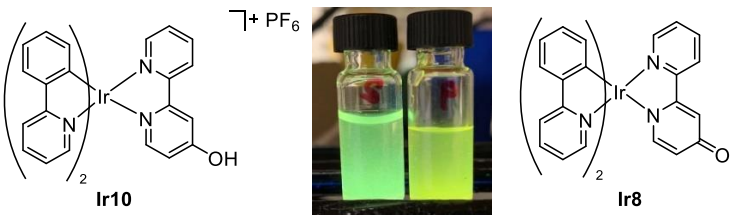

Figure 4.3 Emission images of complex **Ir8** and **Ir10** in DCM (λ_{ex} = 354 nm).

Studies are ongoing examine the emission dependence of this Ir complex as a function of pH. In addition, we are preparing our desired fluorogenic probe via the proposed synthetic route presented in scheme 4.4.

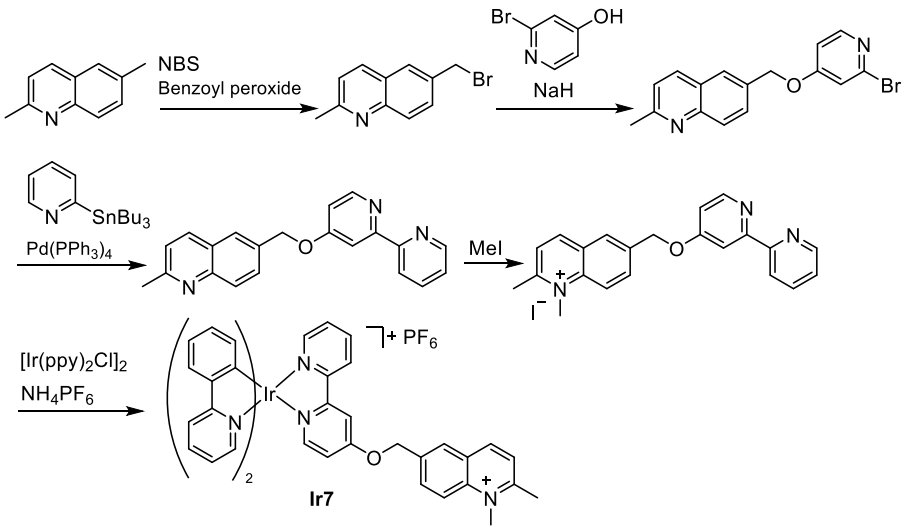

Scheme 4.4 Proposed synthetic route for complex **Ir7**.

In this project, the bipyridine aldehyde iridium probe was synthesized and showed notable increase in fluorescent intensity when subjected to transfer hydrogenation reactions. Our preliminary results suggested that our ratiometric probe design is highly promising. We are now focusing on the synthesis of the ratiometric probe, which will allow us to quantify both the starting materials and products inside live cells.

4.3 Experimental Section

4.3.1 Synthesis

Preparation of Compound 20. Compound 2,9-dimethyl phenanthroline (500 mg, 2.4 mmol, 1.0 equiv.) was dissolved in 52 mL of dioxane/water (96:4) and the mixture was degassed for 30 min. Selenium dioxide (1.1 g, 9.6 mmol, 4 equiv.) was then added and the reaction was refluxed for 6 h under an inert atmosphere. When the reaction was complete, the solution was filtered through a celite pad. A yellow precipitate appeared immediately in the filtrate and was isolated by filtration. This product

was washed with cold chloroform and dried under vacuum (48% yield). ^{1}H NMR (DMSO-d_6, 500 MHz) δ (ppm) = 10.31 (s, 2H), 8.75 (d, J_{HH} = 8.1 Hz, 2H), 8.30 – 8.23 (m, 4H).

Preparation of Complex Ir4. A mixture of precursor $[Ir(ppy)_2Cl]_2$ (42.8 mg, 0.04 mmol, 1.0

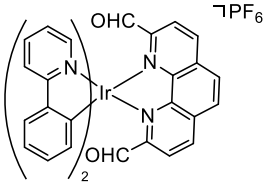

equiv.) and ligand **20** (19 mg, 0.08 mmol, 2.0 equiv.) in 15 mL of DCM/MeOH (2:1) was degassed for 30 min. The reaction was then refluxed under an inert atmosphere for 8 h. After cooling the reaction to room temperature, 10 equiv. of ammonium hexafluorophosphate was added and the suspension was stirred overnight. The solid precipitate was removed by filtration and the filtrate was concentrated under vacuum. The desired product was obtained after purification by column chromatography (15 DCM: 1 acetone) (~7% yield). The NMR spectra showed the presence of impurities.

Preparation of Compound 21. Compound 4,4'-dimethyl-2,2'-bipyridine (276 mg, 1.5

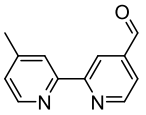

mmol, 1.0 equiv.) was dissolved in degassed dioxane (20 mL). Selenium dioxide (191 mg, 1.7 mmol, 1.1 equiv.) was then added and the reaction was refluxed for 14 h under an inert atmosphere. After completion, the solvent was removed under vacuum and the residue was redissolved in hot chloroform (100 mL). The organic mixture was washed with 1M Na_2CO_3 solution, dried over Na_2SO_4, and concentrated to a volume of 5 mL. The pure product was obtained after purification by Al_2O_3 column chromatography (1 ethyl acetate: 3 hexane) as a white solid (27% yield). ^{1}H NMR ($CDCl_3$, 500 MHz) δ (ppm) = 10.17 (s, 1H), 8.89 (s, 1H), 8.82 (s, 1H), 8.57 (s, 1H), 8.27 (s, 1H), 7.72 (s, 1H), 7.19 (s, 1H), 2.46 (s, 3H).

Preparation of Complex Ir6. A mixture of precursor $[Ir(ppy)_2Cl]_2$ (32.1 mg, 0.03 mmol, 1.0 equiv.) and ligand **21** (12.5 mg, 0.063 mmol, 2.1 equiv.) in 15 mL of DCM/MeOH (2:1) was degassed for 30 min. The reaction was then refluxed under an inert atmosphere for 12 h. After cooling the reaction to room temperature, ammonium hexafluorophosphate (130 mg, 0.3 mmol, 10 equiv.) was then added and the suspension was stirred for 1 h. The solid part material was removed by filtration and the filtrate was concentrated under vacuum. The pure product was obtained after purification by column chromatography (DCM: MeOH 0.5%) as an orange powder (8 mg). ^{1}H NMR ($CDCl_3$, 500 MHz) δ (ppm) = δ 10.28 (s, 1H), 9.10 (s, 1H), 8.66 (s, 1H), 8.12 (d, J_{HH} = 5.2 Hz, 1H), 7.94 – 7.88 (m, 2H), 7.77 (q, J_{HH} = 8.8, 6.6 Hz, 4H), 7.69 (d, J_{HH} = 7.8 Hz, 2H), 7.54 – 7.48 (m, 2H), 7.05 (q, J_{HH} = 11.5, 9.2 Hz, 4H), 6.93 (q, J_{HH} = 7.3 Hz, 2H), 6.32 – 6.24 (m, 2H), 2.65 (s, 3H).

Preparation of Compound 23. To a stirring mixture of 2-bromopyridin-4-ol (348 mg, 2.0 mmol, 1.0 equiv.) in dry THF, NaH 60% (120 mg, 3.0 mmol, 2.5 equiv.) was added and the mixture was stirred at room temperature for 30 min. 2-methoxyethoxymethyl chloride (MEMCl) (236 μL, 2.3 mmol, 1.15 equiv.) was then added and the solution was stirred overnight. The reaction was quenched by slow addition of H_2O. THF was then gently removed under vacuum. The organic compounds were extracted into DCM and then washed with water and brine. The organic layer was concentrated, and the crude product was purified by column chromatography (1 Ethyl acetate: 3 Hexane) to obtain the pure product in 47% yield. ^{1}H NMR ($CDCl_3$, 500 MHz) δ (ppm) = 8.18 (d, J_{HH} = 5.7 Hz, 1H), 7.16 (s, 1H), 6.91 (d, J_{HH} = 5.7 Hz, 1H), 5.30 (s, 2H), 3.82 – 3.78 (m, 2H), 3.55 – 3.52 (m, 2H), 3.36 (s, 3H).

Preparation of Compound 24. A pressure tube was charged with compound **23** (167 mg, 0.64 mmol, 1.0 equiv.) and $Pd(PPh_3)_4$ (74 mg, 0.063 mmol, 10 mol %) in dry toluene (12 mL). The mixture was degassed for 30 min. 3-(tributylstannyl)pyridine (120 mg, 3.0 mmol, 2.5 equiv.) was then added and the mixture was heated at 48 ℃ for 48 h. After completion, toluene was removed under vacuum and the black residue was combined with saturated KF solution (10 mL). This mixture was sonicated for 30 min and then 30 mL of DCM was added. The solution was then sonicated for another 30 min. The mixture was filtered through a celite pad. The celite cake was washed with another 15 mL of DCM. The crude solution was concentrated and purified by Al_2O_3 column chromatography (1 Ethyl acetate: 4 Hexane) to obtain the pure product in 60% yield. There was a trace amount of tin residue in the product, but it did not affect the next step. ^{1}H NMR ($CDCl_3$, 500 MHz) δ (ppm) = 8.62 (d, J_{HH} = 3.8 Hz, 1H), 8.47 (d, J_{HH} = 5.6 Hz, 1H), 8.33 (d, J_{HH} = 7.9 Hz, 1H), 8.02 (d, J_{HH} = 2.0 Hz, 1H), 7.76 (t, J_{HH} = 8.1 Hz, 1H), 7.26 (t, J_{HH} = 5.9 Hz, 1H), 6.95 (dd, J_{HH} = 5.5, 2.2 Hz, 1H), 5.38 (s, 2H), 3.82 – 3.78 (m, 2H), 3.54 – 3.48 (m, 2H), 3.32 (s, 3H).

Preparation of Compound 25. Compound **23** (30 mg, 0.12 mmol, 1.0 equiv.) was dissolved in 4 mL of methanol. 0.5 mL of hydrochloric acid solution in ether was injected and the reaction was stirred at room temperature overnight. The solvent was then removed under vacuum to collect a white solid. This crude product was washed thoroughly with hexane and diethyl ether to remove the MEMCl formed during the reaction. The pure product was a pink powder and was used directly in the next step without characterization.

Preparation of Complex Ir8. A mixture of precursor $[Ir(ppy)_2Cl]_2$ (21.4 mg, 0.02 mmol, 1.0 equiv.), ligand **25** (7.6 mg, 0.04 mmol**,** 2.0 equiv.), and triethyl amine (0.5 mL) in 1,2-

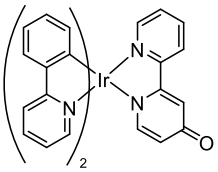

ethanediol (8 mL) was degassed for 30 min. The reaction was then refluxed under inert atmosphere for 15 h. When the reaction was complete, water was added to the solution, and the organic compounds were extracted into DCM. The solvent was then removed to obtain a yellow solid. This solid was sonicated in diethyl ether and hexane for 10 min to dissolve other impurities. A small amount of the product was collected by filtration and was dried under vacuum overnight.

Preparation of Complex Ir9. A mixture of precursor $[Ir(ppy)_2Cl]_2$ (32.3 mg, 0.03 mmol, 1.0 equiv.), and ligand **24** (17 mg, 0.065 mmol, 2.2 equiv.) in 1,2-ethanediol (10 mL) was degassed for 30 min. The reaction was then refluxed under an inert atmosphere for 15 h. After cooling the reaction to room temperature, water (15 mL) was added, and the excess ligand was removed by washing with diethyl ether. The aqueous phase was then heated to 70 ℃ and combined with ammonium hexafluorophosphate (33 mg), the salt of the desire iridium complex immediately precipitated. The mixture was stirred for extra 30 min before being cooled down to 5 ℃. The yellow product was collected by filtration and dried under vacuum overnight (29% yield). ^{1}H NMR ($CDCl_3$, 500 MHz) δ (ppm) = 8.31 (d, J_{HH} = 8.2 Hz, 1H), 8.00 (t, J_{HH} = 12.9 Hz, 3H), 7.90 (d, J_{HH} = 5.3 Hz, 1H), 7.79 (q, J_{HH} = 7.4 Hz, 2H), 7.74 (dd, J_{HH} = 7.4, 4.8 Hz, 2H), 7.68 (d, J_{HH} = 5.6 Hz, 1H), 7.65 (s, 1H), 7.59 (d, J_{HH} = 5.6 Hz, 3H), 7.42 – 7.35 (m, 2H), 6.98 (p, J_{HH} = 8.1, 7.0 Hz, 4H), 6.85 (dt, J_{HH} = 14.5, 7.3 Hz, 2H),), 6.68 – 6.67 (s, 1H), 6.26 (d, J_{HH} = 7.6 Hz, 1H), 6.20 (d, J_{HH} = 7.6 Hz, 1H).

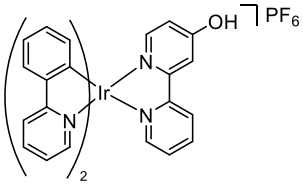

4.3.2 Procedure for Fluorescence Studies

In a quartz cuvette, **Ir4** (0.1 mL from 2.5 mM stock in CH_3CN, 0.8 μmol, 1.0 equiv.), NaHCOO (22 μL from 0.4 mM stock in H_2O, 8.0 μmol, 10.0 equiv.), and iridium catalyst **Ir5**

(13 μL from 0.33 mM stock in CH_3CN, 0.5 mol%) were combined in 3.0 mL of H_2O/CH_3CN (9:1). This solution was stirred at 37 ℃ and the fluorescence spectra were recorded every hour for the first 4 h and then every 2 h for an additional 20 h.

4.3.3 Spectral Characterization

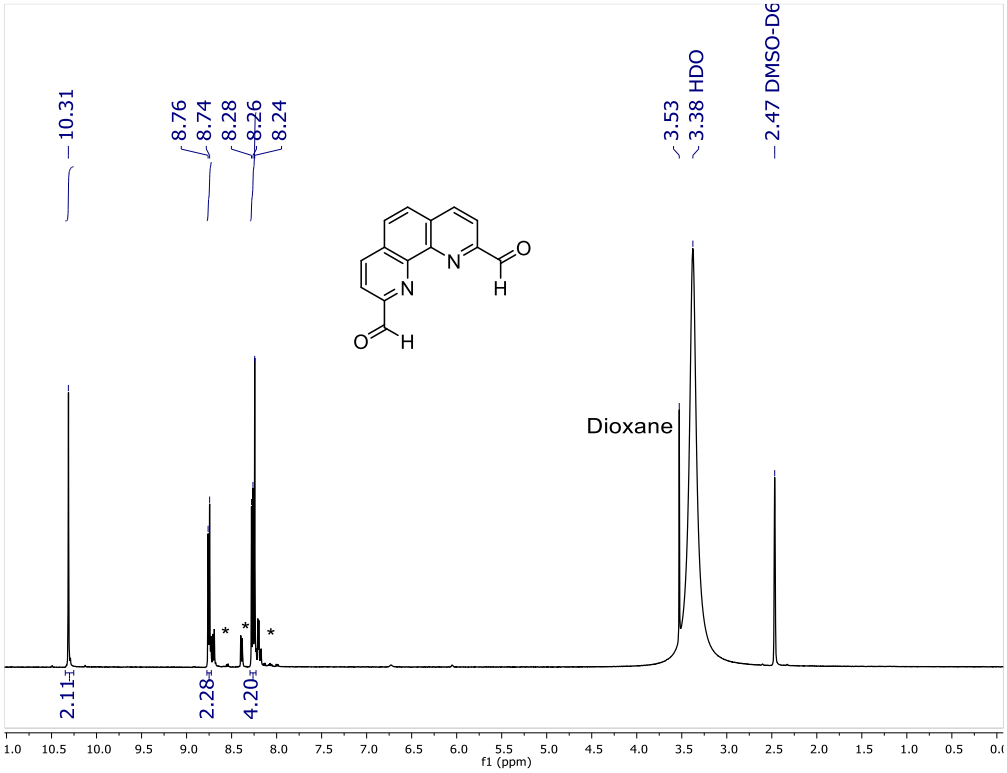

Figure 4.4 ^{1}H NMR spectrum (DMSO-d_6, 500 MHz) of compound **20.**

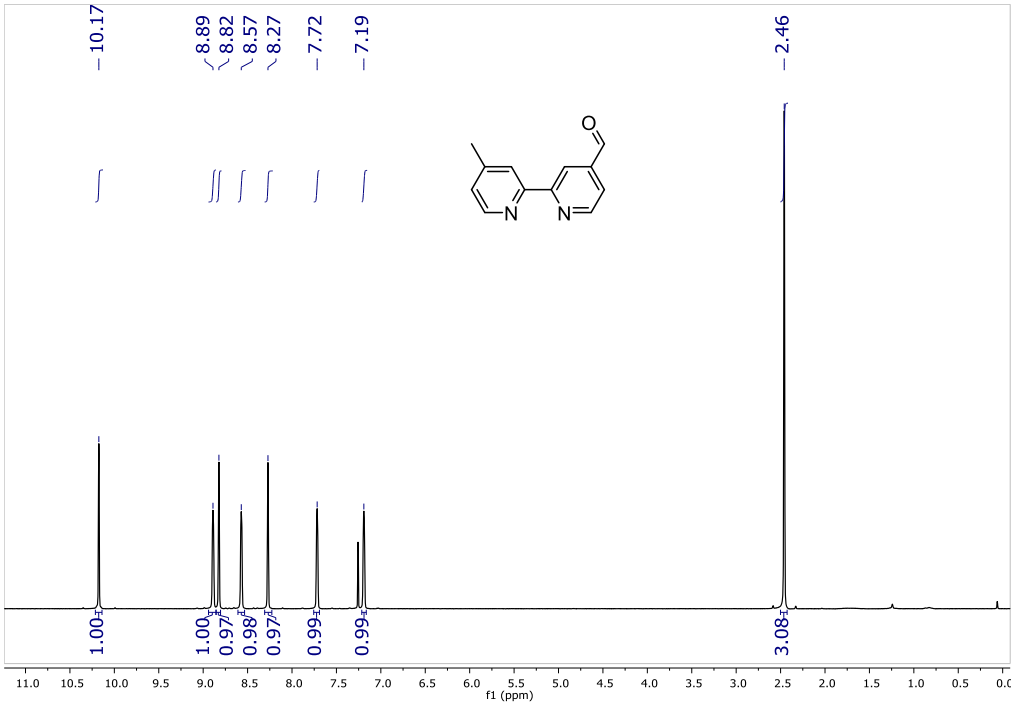

Figure 4.5 ^{1}H NMR spectrum ($CDCl_3$, 500 MHz) of compound **21.**

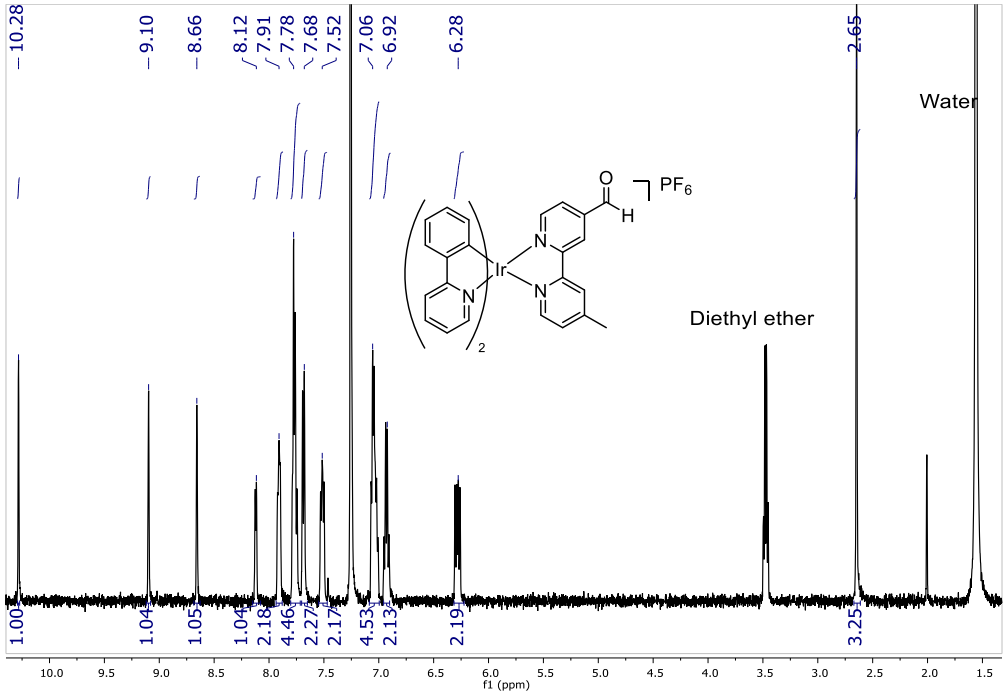

Figure 4.6 ^{1}H NMR spectrum ($CDCl_3$, 500 MHz) of complex **Ir6.**

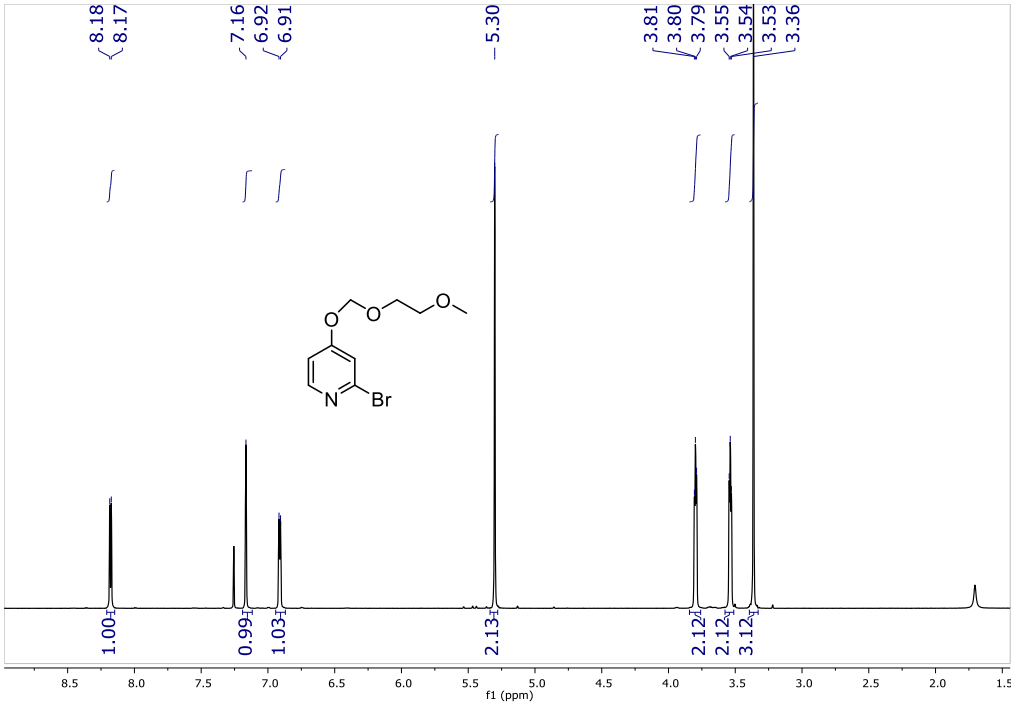

Figure 4.7 ^{1}H NMR spectrum ($CDCl_3$, 500 MHz) of compound **23.**

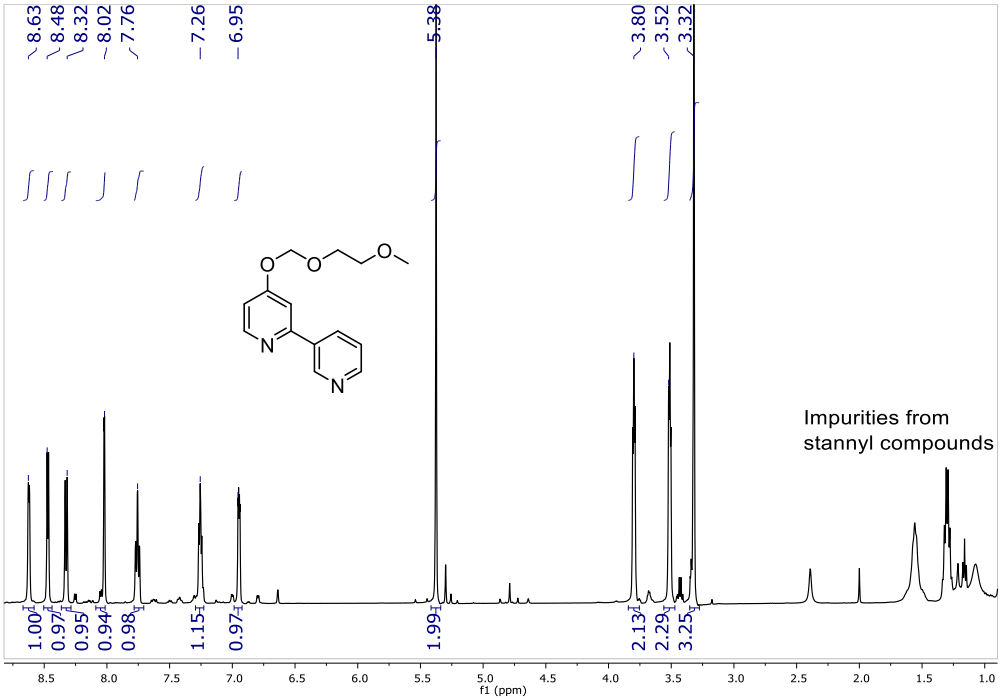

Figure 4.8 ^{1}H NMR spectrum ($CDCl_3$, 500 MHz) of compound **24.**

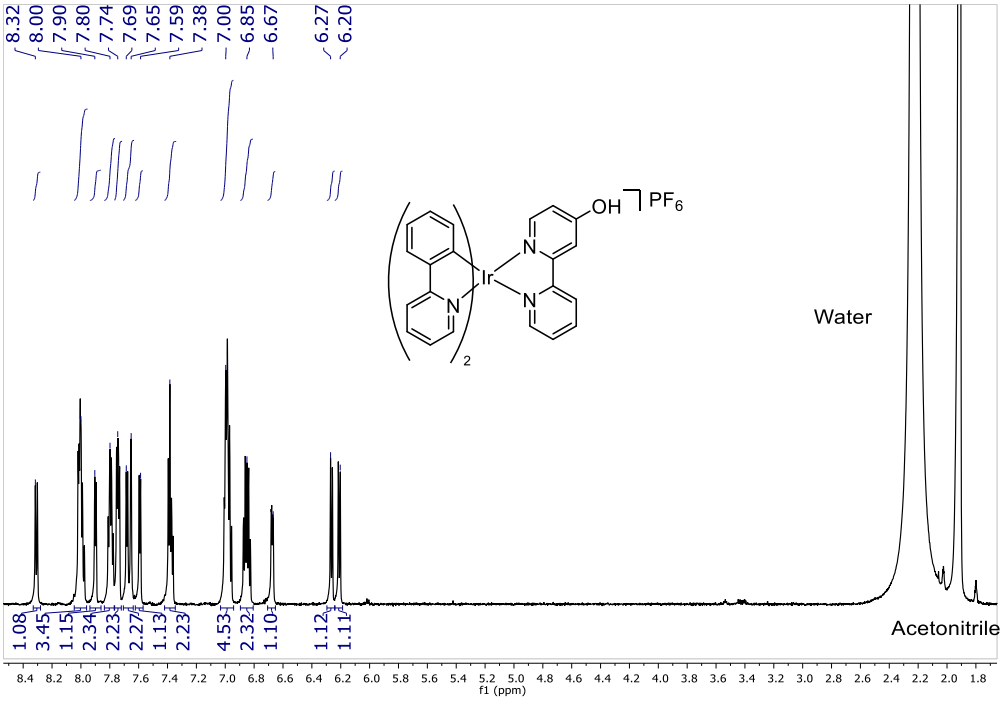

Figure 4.9 ^{1}H NMR spectrum (CD_3CN, 600 MHz) of complex **Ir9.**

Bibliography

1. Bai, Y.; Chen, J.; Zimmerman, S. C., Designed transition metal catalysts for intracellular organic synthesis. *Chem. Soc. Rev.* **2018,** *47* (5), 1811–1821.

2. Mascarenas, J. L.; Destito, P.; Vidal, C.; López, F., Transition metal-promoted reactions in aqueous media and biological settings. *Chem. Eur. J.* **2021,** *27,* 4789–4816.

3. Rebelein, J. G.; Ward, T. R., *In vivo* catalyzed new-to-nature reactions. *Curr. Opin. Chem. Biol.* **2018,** *53*, 106–114.

4. Sasmal, P. K.; Streu, C. N.; Meggers, E., Metal complex catalysis in living biological systems. *Chem. Commun.* **2013,** *49* (16), 1581–1587.

5. Hang, H. C.; Yu, C.; Kato, D. L.; Bertozzi, C. R., A metabolic labeling approach toward proteomic analysis of mucin-type *O*-linked glycosylation. *PNAS* **2003,** *100* (25), 14846–14851.

6. Bertozzi, C. R., A decade of bioorthogonal chemistry. *Acc. Chem. Res.* **2011,** *44* (9), 651–653.

7. Devaraj, N. K., The future of bioorthogonal chemistry. *ACS Cent. Sci.* **2018,** *4* (8), 952–959.

8. Soldevila-Barreda, J. J.; Romero-Canelón, I.; Habtemariam, A.; Sadler, P. J., Transfer hydrogenation catalysis in cells as a new approach to anticancer drug design. *Nat. Commun.* **2015,** *6* (1), 6582–6591.

9. Weiss, J. T.; Carragher, N. O.; Unciti-Broceta, A., Palladium-mediated dealkylation of *N*-propargyl-floxuridine as a bioorthogonal oxygen-independent prodrug strategy. *Sci. Rep.* **2015,** *5* (1), 9329–9336.

10. Kolb, H. C.; Finn, M. G.; Sharpless, K. B., Click chemistry: diverse chemical function from a few good reactions. *Angew. Chem. Int. Ed.* **2001,** *40* (11), 2004–2021.

11. Lebraud, H.; Wright, D. J.; Johnson, C. N.; Heightman, T. D., Protein degradation by in-cell self-assembly of proteolysis targeting chimeras. *ACS Cent. Sci.* **2016,** *2* (12), 927–934.

12. El-Sagheer, A. H.; Brown, T., Synthesis and polymerase chain reaction amplification of DNA strands containing an unnatural triazole linkage. *J. Am. Chem. Soc.* **2009,** *131* (11), 3958–3964.

13. Cendret, V.; François-Heude, M.; Méndez-Ardoy, A.; Moreau, V.; García Fernández, J. M.; Djedaïni-Pilard, F., Design and synthesis of a “click” high-mannose oligosaccharide mimic emulating Man8 binding affinity towards Con A. *Chem. Commun.* **2012,** *48* (31), 3733–3735.

14. Porte, K.; Riberaud, M.; Châtre, R.; Audisio, D.; Papot, S.; Taran, F., Bioorthogonal reactions in animals. *ChemBioChem* **2021,** *22* (1), 100–113.

15. Dawson, P.; Muir, T.; Clark-Lewis, I.; Kent, S., Synthesis of proteins by native chemical ligation. *Science* **1994,** *266* (5186), 776–779.

16. Nilsson, B. L.; Kiessling, L. L.; Raines, R. T., High-yielding Staudinger ligation of a phosphinothioester and azide to form a peptide. *Org. Lett.* **2001,** *3* (1), 9–12

17. Zeglis, B. M.; Sevak, K. K.; Reiner, T.; Mohindra, P.; Carlin, S. D.; Zanzonico, P.; Weissleder, R.; Lewis, J. S., A pretargeted PET imaging strategy based on bioorthogonal Diels-Alder click chemistry. *J. Nucl. Med.* **2013,** *54* (8), 1389–1396.

18. Houghton, J. L.; Membreno, R.; Abdel-Atti, D.; Cunanan, K. M.; Carlin, S.; Scholz, W. W.; Zanzonico, P. B.; Lewis, J. S.; Zeglis, B. M., Establishment of the *in vivo* efficacy of pretargeted radioimmunotherapy utilizing inverse electron demand Diels-Alder click chemistry. *Mol. Cancer Ther.* **2017,** *16* (1), 124–133.

19. Weiss, J. T.; Dawson, J. C.; Macleod, K. G.; Rybski, W.; Fraser, C.; Torres-Sánchez, C.; Patton, E. E.; Bradley, M.; Carragher, N. O.; Unciti-Broceta, A., Extracellular palladium-catalysed dealkylation of 5-fluoro-1-propargyl-uracil as a bioorthogonally activated prodrug approach. *Nat. Commun.* **2014,** *5* (1), 3277–3286.

20. Clavadetscher, J.; Indrigo, E.; Chankeshwara, S. V.; Lilienkampf, A.; Bradley, M., In-cell dual drug synthesis by cancer-targeting palladium catalysts. *Angew. Chem. Int. Ed.* **2017,** *56* (24), 6864–6868.

21. Ngo, A. H.; Bose, S.; Do, L. H., Intracellular Chemistry: Integrating molecular inorganic catalysts with living systems. *Chem. Eur. J* **2018,** *24* (42), 10584–10594.

22. van de L'Isle, M. O. N.; Ortega-Liebana, M. C.; Unciti-Broceta, A., Transition metal catalysts for the bioorthogonal synthesis of bioactive agents. *Curr. Opin. Chem. Biol.* **2020,** *61*, 32–42.

23. Martínez-Calvo, M.; Mascareñas, J. L., Organometallic catalysis in biological media and living settings. *Coordination Chemistry Reviews* **2018,** *359*, 57–79.

24. Heinisch, T.; Ward, T. R., Artificial metalloenzymes based on the biotin-streptavidin technology: challenges and opportunities. *Acc. Chem. Res.* **2016,** *49* (9), 1711–1721.

25. Schwizer, F.; Okamoto, Y.; Heinisch, T.; Gu, Y.; Pellizzoni, M. M.; Lebrun, V.; Reuter, R.; Kohler, V.; Lewis, J. C.; Ward, T. R., Artificial metalloenzymes: reaction scope and optimization strategies. *Chem. Rev.* **2018,** *118* (1), 142–231.

26. Soldevila-Barreda, J. J.; Sadler, P. J., Approaches to the design of catalytic metallodrugs. *Curr. Opin. Chem. Biol.* **2015,** *25*, 172–183.

27. Yusop, R. M.; Unciti-Broceta, A.; Johansson, E. M. V.; Sánchez-Martín, R. M.; Bradley, M., Palladium-mediated intracellular chemistry. *Nat. Chem.* **2011,** *3* (3), 239–243.

28. Li, N.; Lim, R. K. V.; Edwardraja, S.; Lin, Q., Copper-free Sonogashira cross-coupling for functionalization of alkyne-encoded proteins in aqueous medium and in bacterial cells. *J. Am. Chem. Soc.* **2011,** *133* (39), 15316–15319.

29. Toussaint, S. N. W.; Calkins, R. T.; Lee, S.; Michel, B. W., Olefin metathesis-based fluorescent probes for the selective detection of ethylene in live cells. *J. Am. Chem. Soc.* **2018,** *140* (41), 13151–13155.

30. Craig, S.; Eric, M., Ruthenium-induced allylcarbamate cleavage in living cells. *Angew. Chem. Int. Ed.* **2006,** *45* (34), 5645–5648.

31. Timo, V.; Eric, M., Chemical activation in blood serum and human cell culture: improved ruthenium complex for catalytic uncaging of alloc-protected amines. *ChemBioChem* **2017,** *18* (12), 1083–1086.

32. Learte-Aymamí, S.; Vidal, C.; Gutiérrez-González, A.; Mascareñas, J. L., Intracellular reactions promoted by bis(histidine) miniproteins stapled using palladium(II) complexes. *Angew. Chem. Int. Ed.* **2020,** *59* (23), 9149–9154.

33. Miller, M. A.; Askevold, B.; Mikula, H.; Kohler, R. H.; Pirovich, D.; Weissleder, R., Nano-palladium is a cellular catalyst for *in vivo* chemistry. *Nat. Commun.* **2017,** *8* (1), 15906–15919.

34. Tsubokura, K.; Vong, K. K. H.; Pradipta, A. R.; Ogura, A.; Urano, S.; Tahara, T.; Nozaki, S.; Onoe, H.; Nakao, Y.; Sibgatullina, R.; Kurbangalieva, A.; Watanabe, Y.; Tanaka, K., *In vivo* gold complex catalysis within live mice. *Angew. Chem. Int. Ed.* **2017,** *56* (13), 3579–3584.

35. Sasmal, P. K.; Carregal-Romero, S.; Han, A. A.; Streu, C. N.; Lin, Z.; Namikawa, K.; Elliott, S. L.; Köster, R. W.; Parak, W. J.; Meggers, E., Catalytic azide reduction in biological environments. *ChemBioChem* **2012,** *13* (8), 1116–1120.

36. Cao-Milán, R.; Gopalakrishnan, S.; He, L. D.; Huang, R.; Wang, L.-S.; Castellanos, L.; Luther, D. C.; Landis, R. F.; Makabenta, J. M. V.; Li, C.-H.; Zhang, X.; Scaletti, F.; Vachet, R. W.; Rotello, V. M., Thermally gated bio-orthogonal nanozymes with supramolecularly confined porphyrin catalysts for antimicrobial uses. *Chem* **2020**, 1–12.

37. Yang, M.; Yang, Y.; Chen, P. R., Transition-metal-catalyzed bioorthogonal cycloaddition reactions. *Topics Curr. Chem. (Z)* **2016,** *374* (2), 2.

38. Malins, L. R., Peptide modification and cyclization via transition-metal catalysis. *Curr. Opin. Chem. Biol.* **2018,** *46*, 25–32.

39. Link, A. J.; Tirrell, D. A., Cell surface labeling of Escherichia coli via copper(I)-catalyzed [3 + 2] cycloaddition. *J. Am. Chem. Soc.* **2003,** *125* (37), 11164–11165.

40. Speers, A. E.; Adam, G. C.; Cravatt, B. F., Activity-based protein profiling *in vivo* using a copper(I)-catalyzed azide-alkyne [3 + 2] cycloaddition. *J. Am. Chem. Soc.* **2003,** *125* (16), 4686–4687.

41. Bai, Y.; Feng, X.; Xing, H.; Xu, Y.; Kim, B. K.; Baig, N.; Zhou, T.; Gewirth, A. A.; Lu, Y.; Oldfield, E.; Zimmerman, S. C., A highly efficient single-chain metal–organic nanoparticle catalyst for alkyne–azide "click" reactions in water and in cells. *J. Am. Chem. Soc.* **2016,** *138* (35), 11077–11080.

42. Clavadetscher, J.; Hoffmann, S.; Lilienkampf, A.; Mackay, L.; Yusop, R. M.; Rider, S. A.; Mullins, J. J.; Bradley, M., Copper catalysis in living systems and *in situ* drug synthesis. *Angew. Chem. Int. Ed.* **2016,** *55* (50), 15662–15666.

43. Li, S.; Wang, L.; Yu, F.; Zhu, Z.; Shobaki, D.; Chen, H.; Wang, M.; Wang, J.; Qin, G.; Erasquin, U. J.; Ren, L.; Wang, Y.; Cai, C., Copper-catalyzed click reaction on/in live cells. *Chem. Sci.* **2017,** *8* (3), 2107–2114.

44. Bose, S.; Ngo, A. H.; Do, L. H., Intracellular transfer hydrogenation mediated by unprotected organoiridium catalysts. *J. Am. Chem. Soc.* **2017,** *139* (26), 8792–8795.

45. Coverdale, J. P. C.; Romero-Canelon, I.; Sanchez-Cano, C.; Clarkson, G. J.; Habtemariam, A.; Wills, M.; Sadler, P. J., Asymmetric transfer hydrogenation by synthetic catalysts in cancer cells. *Nat. Chem.* **2018,** *10* (3), 347–354.

46. Rebelein, J. G.; Cotelle, Y.; Garabedian, B.; Ward, T. R., Chemical optimization of whole-cell transfer hydrogenation using carbonic anhydrase as host protein. *ACS Catal.* **2019,** *9* (5), 4173–4178.

47. Huang, J.; Wang, L.; Zhao, P.; Xiang, F.; Liu, J.; Zhang, S., Nanocopper-doped cross-linked lipoic acid nanoparticles for morphology-dependent intracellular catalysis. *ACS Catal.* **2018,** *8* (7), 5941–5946.

48. Soldevila-Barreda, J. J.; Metzler-Nolte, N., Intracellular catalysis with selected metal complexes and metallic nanoparticles: advances toward the development of catalytic metallodrugs. *Chem. Rev.* **2019,** *119* (2), 829–869.

49. Destito, P.; Vidal, C.; Lopez, F.; Mascarenas, J. L., Transition metal-promoted reactions in aqueous media and biological settings. *Chem. Eur. J* **2020**, 4789–4816.

50. Rostovtsev, V. V.; Green, L. G.; Fokin, V. V.; Sharpless, K. B., A stepwise Huisgen cycloaddition process: copper(I)-catalyzed regioselective "ligation" of azides and terminal alkynes. *Angew. Chem. Int. Ed.* **2002,** *41* (14), 2596–2599.

51. Moses, J. E.; Moorhouse, A. D., The growing applications of click chemistry. *Chem. Soc. Rev.* **2007,** *36* (8), 1249–1262.

52. Banerjee, P. S.; Ostapchuk, P.; Hearing, P.; Carrico, I., Chemoselective attachment of small molecule effector functionality to human adenoviruses facilitates gene delivery to cancer cells. *J. Am. Chem. Soc.* **2010,** *132* (39), 13615–13617.

53. Abedin, M. J.; Liepold, L.; Suci, P.; Young, M.; Douglas, T., Synthesis of a cross-linked branched polymer network in the interior of a protein cage. *J. Am. Chem. Soc.* **2009,** *131* (12), 4346–4354.

54. Beatty, K. E.; Xie, F.; Wang, Q.; Tirrell, D. A., Selective dye-labeling of newly synthesized proteins in bacterial cells. *J. Am. Chem. Soc.* **2005,** *127* (41), 14150–14151.

55. Hong, V.; Steinmetz, N. F.; Manchester, M.; Finn, M. G., Labeling live cells by copper-catalyzed alkyne−azide click chemistry. *Bioconjugate Chem.* **2010,** *21* (10), 1912–1916.

56. Soriano del Amo, D.; Wang, W.; Jiang, H.; Besanceney, C.; Yan, A. C.; Levy, M.; Liu, Y.; Marlow, F. L.; Wu, P., Biocompatible copper(I) catalysts for *in vivo* imaging of glycans. *J. Am. Chem. Soc.* **2010,** *132* (47), 16893–16899.

57. Okamoto, Y.; Ward, T. R., Transfer hydrogenation catalyzed by organometallic complexes using NADH as a reductant in a biochemical context. *Biochemistry* **2017,** *56* (40), 5223–5224.

58. Htet, Y.; Tennyson, A. G., NAD(+) as a hydride donor and reductant. *J. Am. Chem. Soc.* **2016,** *138* (49), 15833–15836.

59. Ruppert, R.; Herrmann, S.; Steckhan, E., Very efficient reduction of NAD(P)+ with formate catalysed by cationic rhodium complexes. *J. Chem. Soc. Chem. Comm.* **1988,** (17), 1150–1151.

60. Betanzos-Lara, S.; Liu, Z.; Habtemariam, A.; Pizarro, A. M.; Qamar, B.; Sadler, P. J., Organometallic ruthenium and iridium transfer-hydrogenation catalysts using coenzyme NADH as a cofactor. *Angew. Chem. Int. Ed.* **2012,** *51* (16), 3897–3900.

61. Suenobu, T.; Shibata, S.; Fukuzumi, S., Catalytic formation of hydrogen peroxide from coenzyme NADH and dioxygen with a water-soluble iridium complex and a ubiquinone coenzyme analogue. *Inorg. Chem.* **2016,** *55* (15), 7747–7754.

62. Sasmal, P. K.; Carregal-Romero, S.; Parak, W. J.; Meggers, E., Light-triggered ruthenium-catalyzed allylcarbamate cleavage in biological environments. *Organometallics* **2012,** *31* (16), 5968–5970.

63. Unciti-Broceta, A.; Johansson, E. M. V.; Yusop, R. M.; Sánchez-Martín, R. M.; Bradley, M., Synthesis of polystyrene microspheres and functionalization with Pd^0 nanoparticles to perform bioorthogonal organometallic chemistry in living cells. *Nat. Protoc.* **2012,** *7* (6), 1207–1218.

64. Tracey, M. P.; Pham, D.; Koide, K., Fluorometric imaging methods for palladium and platinum and the use of palladium for imaging biomolecules. *Chem. Soc. Rev.* **2015,** *44* (14), 4769–4791.

65. Pak, Y. L.; Swamy, K.; Yoon, J., Recent progress in fluorescent imaging probes. *Sensors* **2015,** *15* (9), 24374–24396.

66. Aron, A. T.; Ramos-Torres, K. M.; Cotruvo, J. A.; Chang, C. J., Recognition- and reactivity-based fluorescent probes for studying transition metal signaling in living systems. *Acc. Chem. Res.* **2015,** *48* (8), 2434–2442.

67. Santra, M.; Ko, S.-K.; Shin, I.; Ahn, K. H., Fluorescent detection of palladium species with an *O*-propargylated fluorescein. *Chem. Commun.* **2010,** *46* (22), 3964–3966.

68. Zhu, B.; Gao, C.; Zhao, Y.; Liu, C.; Li, Y.; Wei, Q.; Ma, Z.; Du, B.; Zhang, X., A 4-hydroxynaphthalimide-derived ratiometric fluorescent chemodosimeter for imaging palladium in living cells. *Chem. Commun.* **2011,** *47* (30), 8656–8658.

69. Liu, W.; Jiang, J.; Chen, C.; Tang, X.; Shi, J.; Zhang, P.; Zhang, K.; Li, Z.; Dou, W.; Yang, L.; Liu, W., Water-soluble colorimetric and ratiometric fluorescent probe for selective imaging of palladium species in living cells. *Inorg. Chem.* **2014,** *53* (23), 12590–12594.

70. Goswami, S.; Manna, A.; Maity, A. K.; Paul, S.; Das, A. K.; Das, M. K.; Saha, P.; Quah, C. K.; Fun, H.-K., Selective detection and bio-imaging of Pd^{2+} with novel 'C–CN' bond cleavage of cyano-rhodamine, cyanation with diaminomaleonitrile. *Dalton Trans.* **2013,** *42* (36), 12844–12848.

71. Chen, H.; Lin, W.; Yuan, L., Construction of a near-infrared fluorescence turn-on and ratiometric probe for imaging palladium in living cells. *Org. Biomol. Chem.* **2013,** *11* (12), 1938–1941.

72. Wang, X.; Guo, Z.; Zhu, S.; Tian, H.; Zhu, W., A naked-eye and ratiometric near-infrared probe for palladium via modulation of a π-conjugated system of cyanines. *Chem. Commun.* **2014,** *50* (88), 13525–13528.

73. Sánchez, M. I.; Penas, C.; Vázquez, M. E.; Mascareñas, J. L., Metal-catalyzed uncaging of DNA-binding agents in living cells. *Chem. Sci.* **2014,** *5* (5), 1901–1907.

74. Timo, V.; Felix, D.; L., G. P.; Eric, M., Progress towards bioorthogonal catalysis with organometallic compounds. *Angew. Chem. Int. Ed.* **2014,** *53* (39), 10536–10540.

75. Hsu, H.-T.; Trantow, B. M.; Waymouth, R. M.; Wender, P. A., Bioorthogonal catalysis: a general method to evaluate metal-catalyzed reactions in real time in living systems using a cellular luciferase reporter system. *Bioconjugate Chem.* **2016,** *27* (2), 376–382.

76. Stenton, B. J.; Oliveira, B. L.; Matos, M. J.; Sinatra, L.; Bernardes, G. J. L., A thioether-directed palladium-cleavable linker for targeted bioorthogonal drug decaging. *Chem. Sci.* **2018,** *9* (17), 4185–4189.

77. Li, J.; Yu, J.; Zhao, J.; Wang, J.; Zheng, S.; Lin, S.; Chen, L.; Yang, M.; Jia, S.; Zhang, X.; Chen, P. R., Palladium-triggered deprotection chemistry for protein activation in living cells. *Nat. Chem.* **2014,** *6* (4), 352–361.

78. Tonga, G. Y.; Jeong, Y.; Duncan, B.; Mizuhara, T.; Mout, R.; Das, R.; Kim, S. T.; Yeh, Y.-C.; Yan, B.; Hou, S.; Rotello, V. M., Supramolecular regulation of bioorthogonal catalysis in cells using nanoparticle-embedded transition metal catalysts. *Nat. Chem.* **2015,** *7* (7), 597–603.

79. Tomás-Gamasa, M.; Martínez-Calvo, M.; Couceiro, J. R.; Mascareñas, J. L., Transition metal catalysis in the mitochondria of living cells. *Nat. Commun.* **2016,** *7* (1), 12538–12548.

80. Jung Jou, M.; Chen, X.; Swamy, K. M. K.; Na Kim, H.; Kim, H.-J.; Lee, S.-g.; Yoon, J., Highly selective fluorescent probe for Au^{3+} based on cyclization of propargylamide. *Chem. Commun.* **2009,** (46), 7218–7220.

81. Yang, Y.-K.; Lee, S.; Tae, J., A Gold(III) ion-selective fluorescent probe and its application to bioimagings. *Org. Lett.* **2009,** *11* (24), 5610–5613.

82. Do, J. H.; Kim, H. N.; Yoon, J.; Kim, J. S.; Kim, H.-J., A rationally designed fluorescence turn-on probe for the gold(III) ion. *Org. Lett.* **2010,** *12* (5), 932–934.

83. Wang, J.-B.; Wu, Q.-Q.; Min, Y.-Z.; Liu, Y.-Z.; Song, Q.-H., A novel fluorescent probe for Au(III)/Au(I) ions based on an intramolecular hydroamination of a bodipy derivative and its application to bioimaging. *Chem. Commun.* **2012,** *48* (5), 744–746.

84. Tang, W.; Becker, M. L., "Click" reactions: a versatile toolbox for the synthesis of peptide-conjugates. *Chem. Soc. Rev.* **2014,** *43* (20), 7013–7039.

85. Beatty, K. E.; Liu, J. C.; Xie, F.; Dieterich, D. C.; Schuman, E. M.; Wang, Q.; Tirrell, D. A., Fluorescence visualization of newly synthesized proteins in mammalian cells. *Angew. Chem. Int. Ed.* **2006,** *45* (44), 7364–7367.

86. Kennedy, D. C.; McKay, C. S.; Legault, M. C. B.; Danielson, D. C.; Blake, J. A.; Pegoraro, A. F.; Stolow, A.; Mester, Z.; Pezacki, J. P., Cellular consequences of copper complexes used to catalyze bioorthogonal click reactions. *J. Am. Chem. Soc.* **2011,** *133* (44), 17993–18001.

87. Bevilacqua, V.; King, M.; Chaumontet, M.; Nothisen, M.; Gabillet, S.; Buisson, D.; Puente, C.; Wagner, A.; Taran, F., Copper-chelating azides for efficient click conjugation reactions in complex media. *Angew. Chem. Int. Ed.* **2014,** *53* (23), 5872–5876.

88. Uttamapinant, C.; Tangpeerachaikul, A.; Grecian, S.; Clarke, S.; Singh, U.; Slade, P.; Gee, K. R.; Ting, A. Y., Fast, cell-compatible click chemistry with copper-chelating azides for biomolecular labeling. *Angew. Chem. Int. Ed.* **2012,** *51* (24), 5852–5856.

89. von Maltzahn, G.; Ren, Y.; Park, J.-H.; Min, D.-H.; Kotamraju, V. R.; Jayakumar, J.; Fogal, V.; Sailor, M. J.; Ruoslahti, E.; Bhatia, S. N., *In vivo* tumor cell targeting with "click" nanoparticles. *Bioconjugate Chem.* **2008,** *19* (8), 1570–1578.

90. Spicer, C. D.; Triemer, T.; Davis, B. G., Palladium-mediated cell-surface labeling. *J. Am. Chem. Soc.* **2012,** *134* (2), 800–803.

91. Yang, M.; Jalloh, A. S.; Wei, W.; Zhao, J.; Wu, P.; Chen, P. R., Biocompatible click chemistry enabled compartment-specific pH measurement inside E. coli. *Nat. Commun.* **2014,** *5* (1), 4981–4991.

92. Fricker, S. P., Metal based drugs: from serendipity to design. *Dalton Trans.* **2007,** (43), 4903–4917.

93. Bugarcic, T.; Habtemariam, A.; Deeth, R. J.; Fabbiani, F. P. A.; Parsons, S.; Sadler, P. J., Ruthenium(II) arene anticancer complexes with redox-active diamine ligands. *Inorg. Chem.* **2009,** *48* (19), 9444–9453.

94. Liu, Z.; Habtemariam, A.; Pizarro, A. M.; Fletcher, S. A.; Kisova, A.; Vrana, O.; Salassa, L.; Bruijnincx, P. C.; Clarkson, G. J.; Brabec, V.; Sadler, P. J., Organometallic half-sandwich iridium anticancer complexes. *J. Med. Chem.* **2011,** *54* (8), 3011–3026.

95. Liu, Z.; Romero-Canelon, I.; Qamar, B.; Hearn, J. M.; Habtemariam, A.; Barry, N. P.; Pizarro, A. M.; Clarkson, G. J.; Sadler, P. J., The potent oxidant anticancer activity of organoiridium catalysts. *Angew. Chem. Int. Ed.* **2014,** *53* (15), 3941–3946.

96. Zhang, P.; Sadler, P. J., Advances in the design of organometallic anticancer complexes. *J. Organomet. Chem.* **2017,** *839*, 5–14.

97. Yang, L.; Bose, S.; Ngo, A. H.; Do, L. H., Innocent but deadly: nontoxic organoiridium catalysts promote selective cancer cell death. *ChemMedChem* **2017,** *12* (4), 292–299.

98. Trachootham, D.; Alexandre, J.; Huang, P., Targeting cancer cells by ROS-mediated mechanisms: a radical therapeutic approach? *Nat. Rev. Drug. Discov.* **2009,** *8* (7), 579–591.

99. Liu, Z.; Romero-Canelón, I.; Qamar, B.; Hearn, J. M.; Habtemariam, A.; Barry, N. P.; Pizarro, A. M.; Clarkson, G. J.; Sadler, P. J., The potent oxidant anticancer activity of organoiridium catalysts. *Angew. Chem. Int. Ed.* **2014,** *53* (15), 3941–3946.

100. Kajetanowicz, A.; Milewski, M.; Rogińska, J.; Gajda, R.; Woźniak, K., Hoveyda-type quinone-containing complexes – catalysts to prevent migration of the double bond under metathesis conditions. *Eur. J. Org. Chem.* **2017,** (3), 626–638.

101. Kubanik, M.; Lam, N. Y. S.; Holtkamp, H. U.; Söhnel, T.; Anderson, R. F.; Jamieson, S. M. F.; Hartinger, C. G., Quinoline-para-quinones and metals: coordination-assisted formation of quinoline-ortho-quinones. *Chem. Commun.* **2018,** *54* (8), 992–995.

102. Matsubara, C.; Kawamoto, N.; Takamura, K., Oxo[5, 10, 15, 20-tetra(4-pyridyl)porphyrinato]titanium(IV): an ultra-high sensitivity spectrophotometric reagent for hydrogen peroxide. *Analyst* **1992,** *117* (11), 1781–1784.

103. Dickinson, B. C.; Huynh, C.; Chang, C. J., A palette of fluorescent probes with varying emission colors for imaging hydrogen peroxide signaling in living cells. *J. Am. Chem. Soc.* **2010,** *132*, 5906–5915.

104. Chang, M. C. Y.; Pralle, A.; Isacoff, E. Y.; Chang, C. J., A selective, cell-permeable optical probe for hydrogen peroxide in living cells. *J. Am. Chem. Soc.* **2004,** *126*, 15392–15393.

105. Gay, C.; Collins, J.; Gebicki, J. M., Hydroperoxide assay with the ferric–xylenol orange complex. *Anal. Biochem.* **1999,** *273* (2), 149–155.

106. Baga, A. N.; Johnson, G. R. A.; Nazhat, N. B.; Saadalla-Nazhat, R. A., A simple spectrophotometric determination of hydrogen peroxide at low concentrations in aqueous solution. *Anal. Chim. Acta* **1988,** *204*, 349–353.

107. Onoda, M.; Uchiyama, T.; Mawatari, K.-i.; Kaneko, K.; Nakagomi, K., Simple and rapid determination of hydrogen peroxide using phosphine-based fluorescent reagents with sodium tungstate dihydrate. *Anal. Sci.* **2006,** *22* (6), 815–817.

108. Takenaka, N.; Furuya, S.; Sato, K.; Bandow, H.; Maeda, Y.; Furukawa, Y., Rapid reaction of sulfide with hydrogen peroxide and formation of different final products by freezing compared to those in solution. *Int. J. Chem. KInet.* **2003,** *35* (5), 198–205.

109. Ngo, A. H.; Do, L. H., Structure–activity relationship study of half-sandwich metal complexes in aqueous transfer hydrogenation catalysis. *Inorg. Chem. Front* **2020,** *7* (3), 583–591.

110. Mandal, K.; Bansal, D.; Kumar, Y.; Rustam; Shukla, J.; Mukhopadhyay, P., Halogen-bonded assemblies of arylene imides and diimides: insight from electronic, structural, and computational studies. *Chem. Eur. J.* **2020,** *26* (46), 10607–10619.

111. Ngo, A. H.; Ibañez, M.; Do, L. H., Catalytic hydrogenation of cytotoxic aldehydes using nicotinamide adenine dinucleotide (NADH) in cell growth media. *ACS Catal.* **2016,** *6* (4), 2637–2641.

112. Liu, Z.; Deeth, R. J.; Butler, J. S.; Habtemariam, A.; Newton, M. E.; Sadler, P. J., Reduction of quinones by NADH catalyzed by organoiridium complexes. *Angew. Chem. Int. Ed.* **2013,** *52* (15), 4194–4197.

113. Komatsu, H.; Shindo, Y.; Oka, K.; Hill, J. P.; Ariga, K., Ubiquinone-rhodol (UQ-Rh) for fluorescence imaging of NAD(P)H through intracellular activation. *Angew. Chem. Int. Ed.* **2014,** *53* (15), 3993–3995.

114. Maenaka, Y.; Suenobu, T.; Fukuzumi, S., Hydrogen evolution from aliphatic alcohols and 1,4-selective hydrogenation of NAD^+ catalyzed by a [C,N] and a [C,C] cyclometalated organoiridium complex at room temperature in water. *J. Am. Chem. Soc.* **2012,** *134* (22), 9417–9427.

115. Maenaka, Y.; Suenobu, T.; Fukuzumi, S., Efficient catalytic interconversion between NADH and NAD^+ accompanied by generation and consumption of hydrogen with a water-soluble iridium complex at ambient pressure and temperature. *J. Am. Chem. Soc.* **2012,** *134* (1), 367–374.

116. Shibata, S.; Suenobu, T.; Fukuzumi, S., Direct synthesis of hydrogen peroxide from hydrogen and oxygen by using a water-soluble iridium complex and flavin mononucleotide. *Angew. Chem. Int. Ed.* **2013,** *52* (47), 12327–12331.

117. Hong, Y.; Sengupta, S.; Hur, W.; Sim, T., Identification of novel ROS inducers: quinone derivatives tethered to long hydrocarbon chains. *J. Med. Chem.* **2015,** *58* (9), 3739–3750.

118. Zhang, X.; Li, X.; Li, Z.; Wu, X.; Wu, Y.; You, Q.; Zhang, X., An NAD(P)H:Quinone oxidoreductase 1 responsive and self-immolative prodrug of 5-fluorouracil for safe and effective cancer therapy. *Org. Lett.* **2018,** *20* (12), 3635–3638.

119. Liu, Z.; Sadler, P. J., Organoiridium complexes: anticancer agents and catalysts. *Acc. Chem. Res.* **2014,** *47* (4), 1174–1185.

120. Ju, X.; Huang, P.; Chen, M.; Wang, Q., Liver X receptors as potential targets for cancer therapeutics. *Oncol. Lett.* **2017,** *14* (6), 7676–7680.

121. Jakobsson, T.; Treuter, E.; Gustafsson, J.-Å.; Steffensen, K. R., Liver X receptor biology and pharmacology: new pathways, challenges and opportunities. *Trends Pharmacol. Sci.* **2012,** *33* (7), 394–404.

122. Schultz, J. R.; Tu, H.; Luk, A.; Repa, J. J.; Medina, J. C.; Li, L.; Schwendner, S.; Wang, S.; Thoolen, M.; Mangelsdorf, D. J.; Lustig, K. D.; Shan, B., Role of LXRs in control of lipogenesis. *Genes Dev.* **2000,** *14* (22), 2831–2838.

123. Lehmann, J. r. M.; Kliewer, S. A.; Moore, L. B.; Smith-Oliver, T. A.; Oliver, B. B.; Su, J.-L.; Sundsethi, S. S.; Winegari, D. A.; Blanchard, D. E.; Spence, T. A.; Willson, T. M., activation of the nuclear receptor LXR by oxysterols defines a new hormone response pathway. *J. Biol. Chem.* **1997,** *272*, 3137–3141.

124. Geyeregger, R.; Zeyda, M.; Stulnig, T. M., Liver X receptors in cardiovascular and metabolic disease. *Cell. Mol. Life Sci.* **2006,** *63* (5), 524–539.

125. Collins, J. L.; Fivush, A. M.; Watson, M. A.; Galardi, C. M.; Lewis, M. C.; Moore, L. B.; Parks, D. J.; Wilson, J. G.; Tippin, T. K.; Binz, J. G.; Plunket, K. D.; Morgan, D. G.; Beaudet, E. J.; Whitney, K. D.; Kliewer, S. A.; Willson, T. M., Identification of a nonsteroidal liver X receptor agonist through parallel array synthesis of tertiary amines. *J. Med. Chem.* **2002,** *45* (10), 1963–1966.

126. Bobin-Dubigeon, C.; Chauvin, A.; Brillaud-meflah, V.; Boiffard, F.; Joalland, M.-P.; Bard, J.-M., Liver X receptor (LXR)-regulated genes of cholesterol trafficking and breast cancer severity. *Anticancer Res.* **2017,** *37* (10), 5495–5498.

127. Vedin, L.-L.; Lewandowski, S. A.; Parini, P.; Gustafsson, J.-Å.; Steffensen, K. R., The oxysterol receptor LXR inhibits proliferation of human breast cancer cells. *Carcinogenesis* **2009,** *30* (4), 575–579.

128. Marino, J. P., Jr.; Kallander, L. S.; Ma, C.; Oh, H. J.; Lee, D.; Gaitanopoulos, D. E.; Krawiec, J. A.; Parks, D. J.; Webb, C. L.; Ziegler, K.; Jaye, M.; Thompson, S. K., The discovery of tertiary-amine LXR agonists with potent cholesterol efflux activity in macrophages. *Bioorg. Med. Chem. Lett.* **2009,** *19* (19), 5617–5621.

129. Collins, J. L.; Fivush, A. M.; Watson, M. A.; Galardi, C. M.; Lewis, M. C.; Moore, L. B.; Parks, D. J.; Wilson, J. G.; Tippin, T. K.; Binz, J. G.; Plunket, K. D.; Morgan, D. G.; Beaudet, E. J.; Whitney, K. D.; Kliewer, S. A.; Willson, T. M., Nonsteroidal liver X receptor agonist through parallel array. *J. Med. Chem.* **2002,** *45*, 4.

130. Washburn, D. G.; Hoang, T. H.; Campobasso, N.; Smallwood, A.; Parks, D. J.; Webb, C. L.; Frank, K. A.; Nord, M.; Duraiswami, C.; Evans, C.; Jaye, M.; Thompson, S. K., Synthesis and SAR of potent LXR agonists containing an indole pharmacophore. *Bioorg. Med. Chem. Lett.* **2009,** *19* (4), 1097–1100.

131. Doyle, M. P., Perspective on dirhodium carboxamidates as catalysts. *J. Org. Chem.* **2006,** *71* (25), 9253–9260.

132. Zamora, A.; Vigueras, G.; Rodríguez, V.; Santana, M. D.; Ruiz, J., Cyclometalated iridium(III) luminescent complexes in therapy and phototherapy. *Coord. Chem. Rev.* **2018,** *360*, 34–76.

133. Caporale, C.; Massi, M., Cyclometalated iridium(III) complexes for life science. *Coord. Chem. Rev.* **2018,** *363*, 71–91.

134. Seybold, P. G.; Gouterman, M., Porphyrins: XIII: Fluorescence spectra and quantum yields. *J. Mol. Spectrosc.* **1969,** *31* (1), 1–13.

135. Wragg, A.; Gill, M. R.; Turton, D.; Adams, H.; Roseveare, T. M.; Smythe, C.; Su, X.; Thomas, J. A., Tuning the cellular uptake properties of luminescent heterobimetallic iridium(III)–ruthenium(II) dna imaging probes. *Chem. Eur. J* **2014,** *20* (43), 14004–14011.

136. Lau, J. S.-Y.; Lee, P.-K.; Tsang, K. H.-K.; Ng, C. H.-C.; Lam, Y.-W.; Cheng, S.-H.; Lo, K. K.-W., Luminescent cyclometalated iridium(III) polypyridine indole complexes—synthesis, photophysics, electrochemistry, protein-binding properties, cytotoxicity, and cellular uptake. *Inorg. Chem.* **2009,** *48* (2), 708–718.

137. Bolte, S.; Cordelières, F. P., A guided tour into subcellular colocalization analysis in light microscopy. *J. Microsc.* **2006,** *224* (3), 213–232.

138. Komatsu, H.; Shindo, Y.; Oka, K.; Hill, J. P.; Ariga, K., Ubiquinone-rhodol (UQ-Rh) for fluorescence imaging of NAD(P)H through intracellular activation. *Angew. Chem. Int. Ed.* **2014,** *53* (15), 3993–3995.